Electronic Environments and Electrochemical Properties of Lithium Storage Materials

Thesis by

Jason Graetz

In Partial Fulfillment of the Requirements

for the Degree of

Doctor of Philosophy

California Institute of Technology

Pasadena, California

2003

(Defended May 7, 2003)

Acknowledgements

I would like to acknowledge a number of people who were instrumental in the completion of this dissertation. First and foremost, I am eternally grateful to my family for their unremitting support. It goes without saying that none of this would have been possible without them.

I am especially grateful to my advisor, Brent Fultz, for his guidance, understanding, and insight over the years. I thank Channing Ahn for a number of enlightening conversations and for the endless hours he spent teaching me the intricacies of energy-loss spectroscopy and the electron microscope. I am grateful to Rachid Yazami for his ceaseless encouragement and for sharing his vast knowledge of electrochemical systems.

I am indebted to everyone who has extended me their friendship, Beavis, Caroline, Rachel, that British guy who lives in my apartment, Adrian and Chuck who have served as both friend and mentor, Mike, and the gentlemen at the Sea View, especially the Foos without whom this may have been completed months earlier. An extra special thanks goes out to Elizabeth, a.k.a. Megan,..."this one's for you"(psyche).

I would like to thank a number of collaborators and colleagues for their contributions to this work, including Peter Rez at ASU for his work with simulating the oxygen partial density of states, and Anton Van der Ven and Gerbrand Ceder for providing the atomic positions used in the VASP code.

I would like to acknowledge a number of companies for their generosity: Enax Inc. (Japan) for providing the the $LiTMO_2$ samples, Crane & Co., Inc. for providing the fiberglass used in the electrochemical cells, and Reminex Inc. (Morocco) for the elemental analyses.

This work was supported by the Department of Energy through Basic Energy Sciences Grant No. DE-FG03-00ER15035.

Abstract

The local electronic environments and energy storage properties of lithium electrodes are investigated through inelastic electron scattering and electrochemical measurements. Experimental and computational methods are developed to characterize the electronic structure of lithiated compounds during electrochemical cycling. An electrochemical investigation of new lithium alloys has led to a better understanding of the thermodynamics, kinetics, and mechanical properties of nanostructured materials. These studies have also inspired the development of new anode materials for rechargeable lithium batteries.

One of the large controversies regarding lithium cathodes concerns the arrangement of the local electronic environments in the host material and how these environments are affected by lithium intercalation. To investigate this issue, the core edges of the $3d$ transition-metal oxides were studied using electron energy-loss spectrometry. A number of techniques were developed to better understand how characteristics of the electronic structure are reflected in the core edge and near-edge structure of metal oxides. An empirical relationship is established between the transition-metal $L_{2,3}$ white line intensity and the transition-metal $3d$ occupancy. In addition, the near-edge structure of the oxygen K-edge was used to investigate the $2p$ electron density about the oxygen ions. The results of these investigations were used to study charge compensation in lithiated transition-metal oxides (e.g., $LiCoO_2$ and $LiNi_{0.8}Co_{0.2}O_2$) during electrochemical cycling. These results show a large increase in state occupancy of the oxygen $2p$ band during lithiation, suggesting that much of the lithium $2s$ electron is accommodated by the anion. *Ab initio* calculations of the oxygen $2p$ partial density of states curves confirm the increase in unoccupied states that accompany lithium extraction. In contrast with the large changes observed in the oxygen K-edge, much smaller changes were observed in the transition-metal $L_{2,3}$ white lines. Surprisingly, for layered $LiCoO_2$ and Li(Ni, Co)O_2, the transition-metal valence changes little during the charge compensation accompanying lithiation. These results have led to a better understanding of intercalation hosts and the role of oxygen in these layered structures.

Recent demand for alternatives to graphitic carbon for lithium anodes motivated an investigation into novel binary lithium alloys. The large volume expansions associated with lithium insertion is known to generate tremendous microstructural damage, making most alloys unsuitable for rechargeable lithium batteries. Electrodes of nanostructured lithium alloys were prepared in an attempt to mitigate the particle decrepitation that occurs during cycling and to shorten diffusion times for lithium. Anodes of silicon and germanium were prepared in thin film form as nanocrystalline particles (10 nm mean diameter) and as continuous amorphous thin films (60–250 nm thick). These nanostructured materials

exhibited stable capacities up to six times larger than what is found in graphitic carbons, which are currently the industry standard. In addition, these electrodes do not suffer from particle decrepitation and therefore exhibit excellent cycle life. Nanocrystalline electrodes of silicon and germanium were found to transform into a glassy phase via an electrochemically driven solid-state amorphization during the initial alloying. The disordered structure is believed to assuage strains of intercalation by bypassing multiple crystallographic phases. However, the primary reason for the improved reversibility in these electrodes is attributed to the nanoscale dimensions, which circumvent conventional mechanisms of mechanical deterioration. Nanostructured Li-Si and Li-Ge exhibit the highest reversible electrochemical capacities yet reported for an alloy electrode.

Future investigations of the local electronic environments in cathodes could be extended to include more complicated systems such as Li(Ni, Mn)O_2 and Li(Fe, X)PO_4. Our results suggest that the electronic stability of the metal ion is necessary to maintain a prolonged cycle life. Therefore, an understanding of charge compensation in these complex oxides will be important for understanding new cathode materials. The electronic environments will also be a critical component in the development of alternative anodes, such as binary and ternary lithium alloys. Chemical and valence maps will be used to determine how the lithium is distributed and how its chemical potential varies throughout the electrode. In addition, a better understanding of the thermodynamics, kinetics, and mechanical properties of lithium hosts will be necessary for the development of lithium electrodes with high capacities and high rate capabilities.

Contents

List of Figures

List of Tables

Chapter 1 Electrochemical Cells

1.1 Introduction

A typical electrochemical, or galvanic cell, converts chemical energy into electrical energy through a controlled exothermic chemical reaction. In its simplest form, a galvanic cell consists of two electrodes (cathode and anode) and an electrolyte. By definition, reduction always occurs at the cathode while oxidation always occurs at the anode. A schematic of a galvanic cell is shown in Figure 1.1. The reaction is controlled by electrically isolating

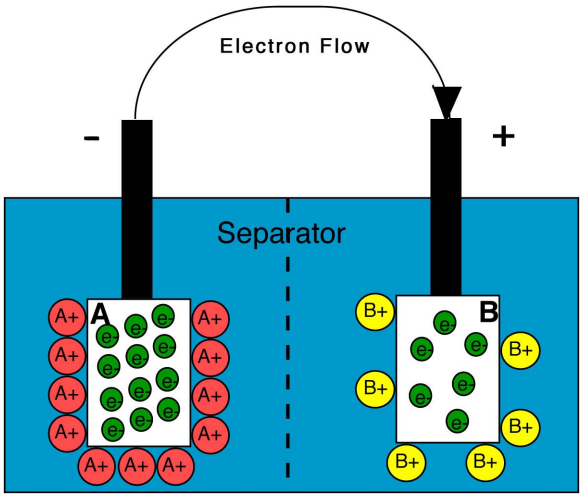

Figure 1.1: Typical electrochemical cell where the anode is oxidized ($A \rightarrow A^+ + e^-$) and the cathode is reduced ($B^+ + e^- \rightarrow B$).

the cathode from the anode. The two compartments are connected through an ionically conducting, electrically insulating medium, typically a liquid or solid electrolyte. During discharge, an external electrical connection is made between the two electrodes. The oxidation of the anode releases electrons, which travel through the electronic circuit to reduce the cathode. To ensure charge neutrality in each compartment of the cell, ions are separately transported through a salt bridge. In primary cells the reactants are entirely consumed by an irreversible reaction. Secondary cells exploit a reversible electrochemical reaction and therefore, can be charged to return the cell to its original state.

1.2 Thermodynamics

The equilibrium cell voltage ($\Delta\epsilon$), or standard potential, is determined by the thermodynamic driving force of the chemical reaction. It is straightforward to calculate the cell voltage and its dependence upon the intensive thermodynamic variables. We begin with the Gibbs-Helmholtz relation, which states that the free energy in the reaction, ΔG, is the difference between the reaction enthalpy, $\Delta H = \Delta U + P\Delta V$, and the entropic term, $T\Delta S$:

$$\Delta G = \Delta H - T\Delta S. \tag{1.1}$$

When combining this with the "fundamental equation" ($\Delta U(S,V) = T\Delta S - P\Delta V - w_e$) it is apparent that the free energy is directly related to the electrochemical work done by the cell, w_e:

$$w_e = \Delta U - T\Delta S + P\Delta V = \Delta H - T\Delta S = \Delta G. \tag{1.2}$$

The work is related to the electrical potential by the the following expression:

$$w_e = -neN_{\mathrm{A}}\Delta\epsilon, \tag{1.3}$$

where n number of electrons exchanged in the reaction (e.g., $n = 1$ in lithium cells), F is the the Faraday constant, and N_{A} is Avogadro's number (6.02×10^{23} mol^{-1}). This expression can be rewritten as

$$\Delta\epsilon = \frac{-\Delta G}{nF}, \tag{1.4}$$

where $F = 96485$ C mol^{-1} $= 26.8$ Ah mol^{-1}.

The equilibrium electrical potential is a function of the chemical potentials μ of the reactants i:

$$\Delta G = \sum_i \nu_i \mu_i, \tag{1.5}$$

where ν is $+1$ for substances formed (reducing agents) and -1 for substances consumed (oxidizing agents) in the reaction. Therefore, the thermodynamic component of the cell voltage can be expressed as the sum of the chemical potentials of the substances involved in the reaction:

$$\Delta\epsilon_0 = -\frac{1}{nF}\sum_i \nu_i \mu_i, \tag{1.6}$$

where $\Delta\epsilon_0$ is known as the "standard potential." The full cell potential must also take into account the concentrations of the different reacting species c. The standard thermodynamic relation between chemical potential and concentration is given by

$$\mu_i = \mu_i^0 + RT\ln c_i. \tag{1.7}$$

Substituting Equation 1.7 into Equation 1.6 yields the Nernst equation:

$$\Delta\epsilon = \Delta\epsilon_0 - \frac{RT}{nF}\sum_i \nu_i \ln c_i. \tag{1.8}$$

The Nernst equation relates the electrical potential to differences in the chemical potential and ionic concentration.

1.3 The Lithium Cell

The invention of the lithium battery was a great advance in the field of electrochemistry and there is considerable interest in the development of lithium electrodes for their use in secondary cells. Although the alkali metals form a group of interesting electrodic materials, lithium is the most electropositive, and will therefore exhibit the highest electrical potential (ϵ_{Li} vs. ϵ_{Li^+}). In addition to their high voltage, lithium cells offer a high energy density and reversible cycling. Primary lithium cells are generally composed of a metallic lithium anode and a layered metal oxide or metal dichalcogenide cathode. Due to its low density, lithium metal has a large specific capacity, 3860 mAh/g. Despite its high theoretical energy density, metallic lithium is not a practical anode in secondary, liquid electrolyte cells. When charged, the lithium ions are forced across the electrolyte to the metal anode where the electrodeposition forms surface clusters. During charging, lithium metal is electroplated onto the anode surface, but there is no thermodynamic tendency to stop the formation of shape asperities such as dendrites that can cause short circuits across the electrolyte [6]. A framework structure (e.g., graphitic carbon) is necessary to preserve the anode shape during cycling.

The typical secondary lithium cell (Figure 1.2) is a concentration cell (also known as a rocking chair battery) where the lithium ions are transported from a lithium source (cathode) to a lithium sink (anode) during discharge. The modern secondary lithium electrode

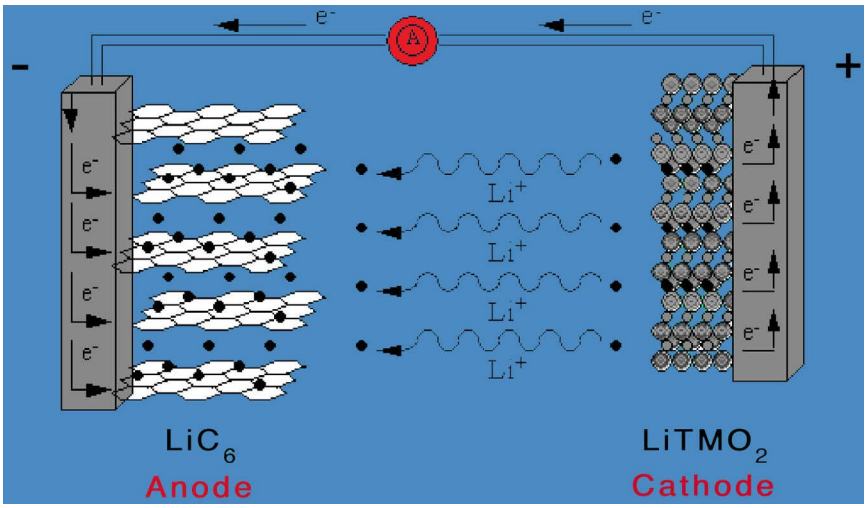

Figure 1.2: Schematic of a full electrochemical lithium cell during charge.

uses a host material to store lithium ions. These materials generally take the form of intercalation, or insertion, compounds. Typical electrodes have a layered structure with large open channels for the diffusion and storage of the lithium guests. Intercalation compounds permit a topotactic insertion of lithium where the mobile lithium guests occupy open layers of the stable host. This is equivalent to an interstitial insertion of lithium into the host. This method of lithium insertion/extraction has the potential to admit lithium with only minor modifications to bonding and the host structure. Mitigating changes of the electronic and mechanical structure throughout the cycle are critical to ensure a reversible reaction.

1.3.1 Cathodes for Lithium Batteries

The typical lithium cathode is a layered intercalation compound, generally a metal dichalcogenide or metal oxide. A list of common cathodes is presented in Table 1.1. Currently, the

Cathode	Cycling Range	Average E (V)	Capacity (mAh/g)	Energy Density (Wh/kg)
$Li_xMn_2O_4$	$1.0 \leq x \leq 2.0$ [7][2]	3.0	143	428
Li_xCoO_2	$0.5 \leq x \leq 1.0$ [8]	4.0	137	548
Li_xNiO_2	$0.5 \leq x \leq 1.0$ [9]	3.8	137	521
$Li_xNi_{1-y}Co_yO_2$	$0.4 \leq x \leq 1.0$ [10][3]	3.9	164	640
Li_xVO_2	$0.7 \leq x \leq 1.0$ [11]	3.6	89	320
Li_xFePO_4	$0.0 \leq x \leq 1.0$ [12]	3.5	170	595

Table 1.1: Some common lithium cathodes showing the cycling range, the average voltage (E), the theoretical specific capacity ($Li/LiTMO_2$), and the theoretical energy density.

preferred cathodes are the layered lithium transition-metal oxides ($LiTMO_2$ where TM = V, Mn, Co, Ni). A layered structure is well suited as an intercalation cathode owing to good mobility of lithium ions and its tolerance of internal strains of intercalation [15]. The crystal structures of the Co, Ni, and V based cathodes have a rhombohedral symmetry and belong to the $R\bar{3}m$ space group. In these materials the lithium and TM ions order along (111) planes to form alternating cation layers [16, 17]. The TM ion, located in octahedral sites, forms a strong bond with neighboring oxygen atoms to produce O-TM-O sheets. Layers of octahedrally coordinated Li^+ ions are sandwiched between the TMO_2 sheets. The layered $LiTMO_2$ structure is shown in Figure 1.3. $LiCoO_2$ is the only material of the TM group that

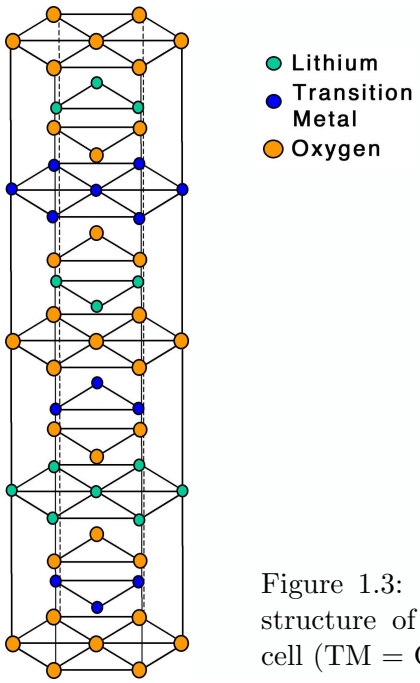

Figure 1.3: The open, layered structure of the $LiTMO_2$ unit cell (TM = Co, Ni, and V).

is easy to prepare in the ideal layered structure (c/a=4.99) and has therefore become the industry standard for secondary lithium cells. $LiNiO_2$ suffers from cationic disorder where nickel ions occupy lithium sites forming a $Li_{1-y}Ni_{1+y}O_2$ compound [18]. The formation of a mixed cation layer considerably reduces the electrochemical activity and the kinetics of lithium diffusion. Similar problems exist in $LiVO_2$ where a disordered layered structure is formed upon delithiation. The structural changes that occur in $Li_{1-x}VO_2$ ($0.0 \leq x \leq 0.3$) reduce the lithium kinetics by eliminating the diffusion channels. The layered $LiMnO_2$ is

[1] There is some debate over the maximum depth of discharge of lithiated manganese spinels: $0.4 \leq x \leq 2$ [13] or $0 \leq x \leq 2$ [14]. However, the standard 3 V cycling range is $1 \leq x \leq 2$ as given in Table 1.1.

[2] Values given for $y = 0.20$.

difficult to synthesize and suffers from cation disorder as well as a loss of symmetry due to crystallographic distortions originating with the Jahn-Teller Mn^{3+} ions. A lithium manganese oxide with a cubic spinel structure ($LiMn_2O_4$) is also of interest as a secondary cathode.[3]

The most promising alternative to $LiCoO_2$ are the olivine cathodes ($LiTMPO_4$). $LiFePO_4$ has recently attracted considerable attention due its high specific capacity and reasonably high voltage [19]. This material has the desirable characteristics of $LiCoO_2$ but with the substitution of cobalt for a less toxic, cheaper cation. However, $LiFePO_4$ is plagued by a very low conductivity (10^{-6} S cm^{-2})[20] and much work is being done to improve the conductivity via copper and silver additives, carbon coating, and doping with supervalent cations [20, 19, 21, 22, 12, 23].

1.3.2 Anodes for Lithium Batteries

In recent years, a number of negative electrodes have been developed as alternatives to lithium metal. Although these materials offer safer cycling conditions and an extended cycle life, the presence of an electrochemically inactive host reduces the specific capacity. In addition, the chemical potential of lithium in a host is more electropositive, which reduces the overall cell voltage. The desirable properties of lithium hosts are a low density (low Z), a high solubility of lithium, and a low voltage vs. lithium metal. A list of typical anodes is shown in Table 1.2.

The most widely used lithium anode is graphitic carbon which, similar to the cathodes, is a layered intercalation compound. Graphite was found to reversibly intercalate lithium with a polymeric electrolyte in 1983 [24] and is presently the industry standard. Lithiated carbons have stable phases up to the LiC_6 stoichiometry corresponding to a theoretical specific capacity of 372 mAh/g. A few of the low voltage (1–2 V vs. lithium) lithium transition-metal oxides have been considered as candidate lithium anodes due to their excellent cycling properties. However, these anodes produce a low overall cell voltage and also exhibit a low specific capacity. Other candidate anodes include the lithium binary alloys (Li-Al, Li-Si, Li-Sn), some of which posses theoretical specific capacities over an order of magnitude greater than that of graphite. However, these materials do not insert lithium topotactically and undergo a number of crystallographic phase changes before they are fully lithiated.

[3]The manganese oxides (γ-β MnO_2) were originally used in lithium batteries as primary cathodes.

As a result, these anodes are generally plagued by slow kinetics of lithium diffusion at room temperature and large volume dilations during lithium insertion/extraction. A final group of interesting lithium anodes are the intermetallic compounds (Li-Cu-Sn, Li-Al-In, Li-In-Sb). These materials have received recent attention due to their high specific and volumetric capacities, and their ability to cycle lithium with only minor volumetric and structural changes.

Anode	Average E (V)	Capacity (mAh/g)
Li Metal	0.0	3860[4]
Li_xC_6	0.0-0.5	372
Li-SnO_2	0.1-1.2	800
LiAl	0.3	800
$Li_{22}Si_5$	0.3	4212
$LiTiS_2$	1.5-2.7	226

Table 1.2: Some common lithium anodes showing the average voltage (E) and the theoretical specific capacity (Li/$LiTMO_2$).

1.4 The Cell Potential and the Gibbs Phase Rule

Crystallographic changes that occur in lithium electrodes during cycling are often reflected in the cell potential. To better understand these changes, the temperature and potential binary phase diagrams for a hypothetical alloy of Li_xM are shown in Figure 1.4. During electrochemical cycling, the lithium concentration moves horizontally (at T_0) through the temperature phase diagram (Figure 1.4a). As x is varied, the cell potential (Figure 1.4b) alternates between regions of invariance and regions of continuous change. This can be understood through Gibbs' phase rule, which states that the number of degrees of freedom, f, is given by

$$f = c - p + 2, \tag{1.9}$$

where c is the number of components and p is the number of phases present. When the electrochemical cell is cycled at a fixed temperature and pressure, two degrees of freedom are specified. Therefore, in a two component system with a single phase there is one degree of freedom ($f = 1$) and the voltage varies continuously with lithium concentration. However,

[4]The theoretical specific capacity of lithium metal is given for the discharge reaction. To conform with values common in the literature, all other specific capacities are given for the charge reaction. The specific capacity of $Li_{22}Si_5$ is not larger than that of lithium metal.

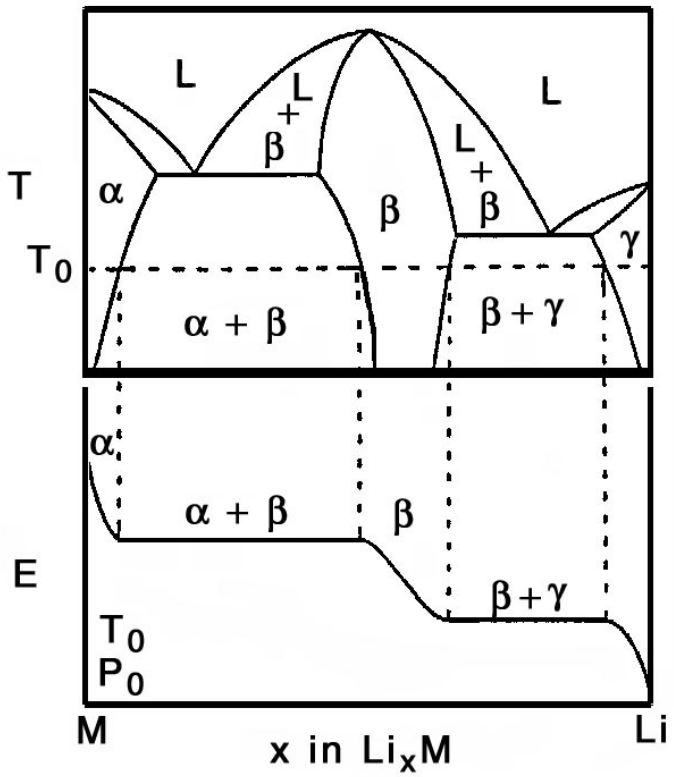

Figure 1.4: (**a**) Temperature and (**b**) potential phase diagrams of Li_xM showing multiple plateaus corresponding to coexistence regions [1].

in a two phase region $f = 0$ and the remaining intensive thermodynamic variables, such as the chemical potential, are fixed. The cell potential will remain constant for all values of x within this coexistence region. Most electrodes, such as LiC_6, exhibit a series of voltage plateaus during electrochemical cycling. Therefore, the charge/discharge profile can be used to identify various coexistence regions in the binary phase diagram at a constant temperature.

Chapter 2 Inelastic Electron Scattering and EELS

2.1 Electron Energy-Loss Spectrometry

Electron energy-loss spectrometry (EELS) measures the energy distribution of electrons scattered inelastically by a sample. When high-energy electrons pass through a sample, they can scatter via coulombic interaction with atoms in the sample. The elastically scattered electrons typically undergo changes in momentum but do not transfer energy to the material. Electrons scattered inelastically transfer momentum and energy to the material. The inelastically scattered electrons can yield information regarding the electronic structure and bonding of atoms in the material.

2.1.1 Instrumentation: Gatan 666 Parallel Detection Spectrometer

In an EELS experiment, high-energy electrons are transmitted through a sample and into a magnetic-prism spectrometer, which separates the electrons by energy. A schematic of a Gatan 666 parallel detection spectrometer is shown in Figure 2.1. In this configuration, the EELS spectrometer is mounted below a conventional transmission electron microscope (TEM), just after the projector lens. Figure 2.2 displays a diagram of electron trajectories through the prism. Electrons enter the spectrometer (on and off the optic axis) and travel in the z-direction with a velocity, $\boldsymbol{v}$, and interact with a magnetic field, $\boldsymbol{B}$, in the y-direction (out of the page). The electrons are forced into circular orbits by the Lorentz force ($\boldsymbol{F} = -e\boldsymbol{v} \times \boldsymbol{B}$), creating arcs of equal curvature for electrons of equivalent energy. The Lorentz force is also responsible for focusing the electrons that entered the prism with trajectories off the optic axis. The radius of curvature, R is given by equating the Lorentz force and the centripetal force ($F = mv^2/R$) acting on the electron,

$$R = \gamma \frac{vm}{eB}, \tag{2.1}$$

where m is the rest mass of the electron and a relativistic constant $\gamma = (1 - v^2/c^2)^{-1/2}$ has been introduced to account for the electrons traveling close to c. After being bent by

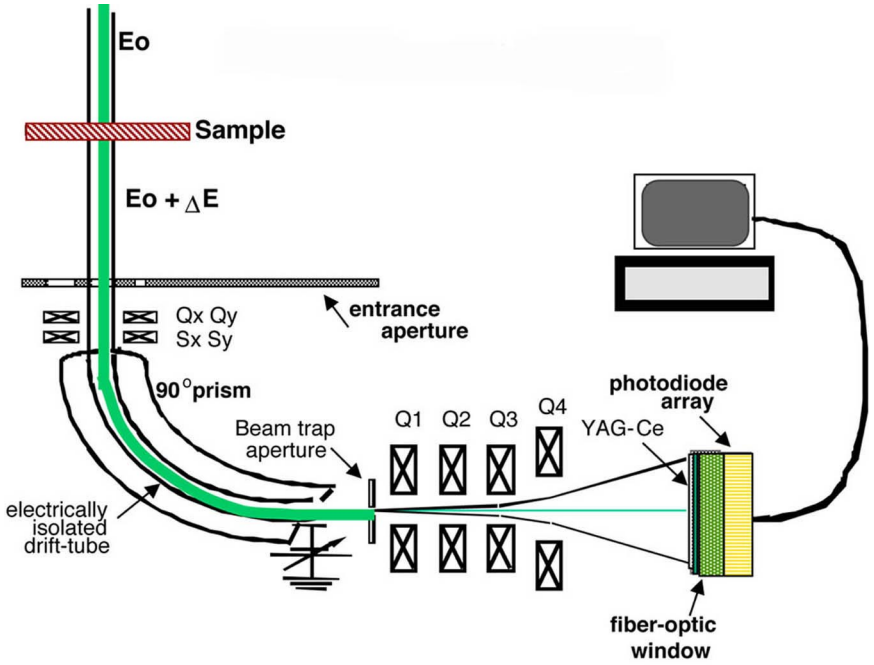

Figure 2.1: Schematic of the EELS spectrometer. Incident electrons pass through the sample and into the 90° magnetic prism where the Lorentz force separates the electrons by energy. The electrons subsequently pass through a series of quadrupole magnets (labeled Q1–Q4) and onto a linear detector array.

approximately 90°, the electrons exit the prism with a spatial dispersion related to their energy-loss. After passing through a set of quadrupole magnets (Q1–Q4), which amplify their spatial dispersion, the electrons are projected onto a parallel detector. The detector is composed of a scintillator (a YAG single crystal) and a linear photodiode array.

2.1.2 Features of Energy-Loss Spectra

The typical energy-loss spectrum can be divided into three regions: the zero-loss region from 0–5 eV, the low loss region from 5–50 eV, and the core-loss region over 50 eV. Figure 2.3 identifies the different features in a typical energy-loss spectrum. The bulk of the spectral intensity is located in the zero-loss peak (0 eV), which contains contributions from elastically scattered electrons and those that have undergone negligible energy transfer, such as phonon excitations (< 100 meV). The width of the elastic peak is a measure of the instrument resolution (typically less than 2 eV). The low-loss region is dominated by intensity contributions from plasmon excitations, which occur at ~ 25 eV. The plasmon is a quantum of charge oscillation from the electrons in a solid. Plasmons occur at a

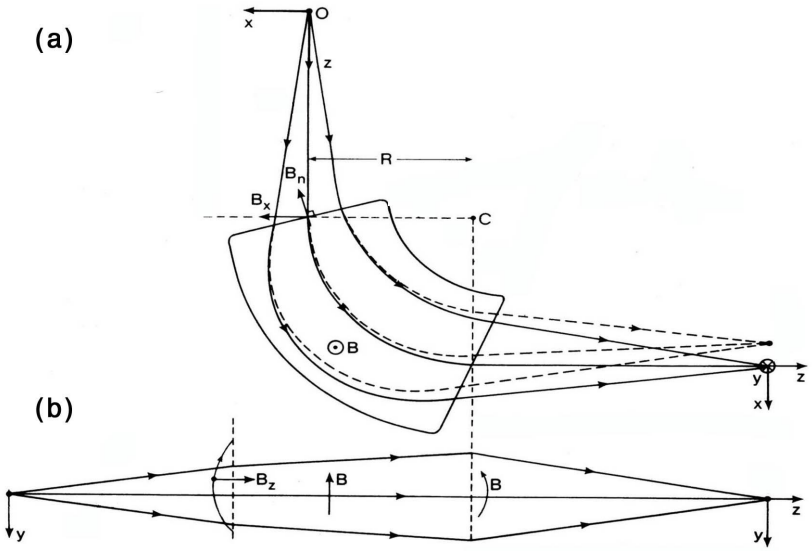

Figure 2.2: Schematic of electron trajectories through the spectrometer demonstrating (**a**) radial focusing and (**b**) axial focusing. The dashed lines indicate trajectories of electrons that have lost energy [25].

characteristic energy E_{p}, which is a function of the electron density. The number of plasmon peaks is determined by the sample thickness and the plasmon mean free path (~ 100 nm). Multiple plasmons are observed at intervals of E_{p} when the sample thickness is large ($t >$ 100 nm). Therefore, plasmons are often used to determine the specimen thickness. Free-electron-like materials with a low density of states near the Fermi energy (e.g., aluminum) typically have sharp plasmon peaks but usually lack detailed structure.

The most interesting region of the energy-loss spectrum occurs at energy losses greater than 50 eV where the core-edges are observed. These edges are produced when the incident electron excites an electronic transition from an atomic core state into an unoccupied atomic state within the atom or the external continuum (ionization). The sharp transition occurs at $E = E_n - E_{n'}$, where E_n is the binding energy of the core electron and $E_{n'}$ is the binding energy of the excited electron ($E_{n'} = 0$ for ionization). The post-edge region is characterized by a decay governed by the ionization cross section and generally is generally a power-law, of the form AE^{-r} (where A and r are positive constants). To approximate the binding energy E_n, we begin by considering a hydrogenic (spherically symmetric) atom with atomic number Z, and electron radius r. The Hamiltonian of this system is

$$H = -\frac{\hbar^2}{2m}\nabla^2 - \frac{Ze^2}{r}. \tag{2.2}$$

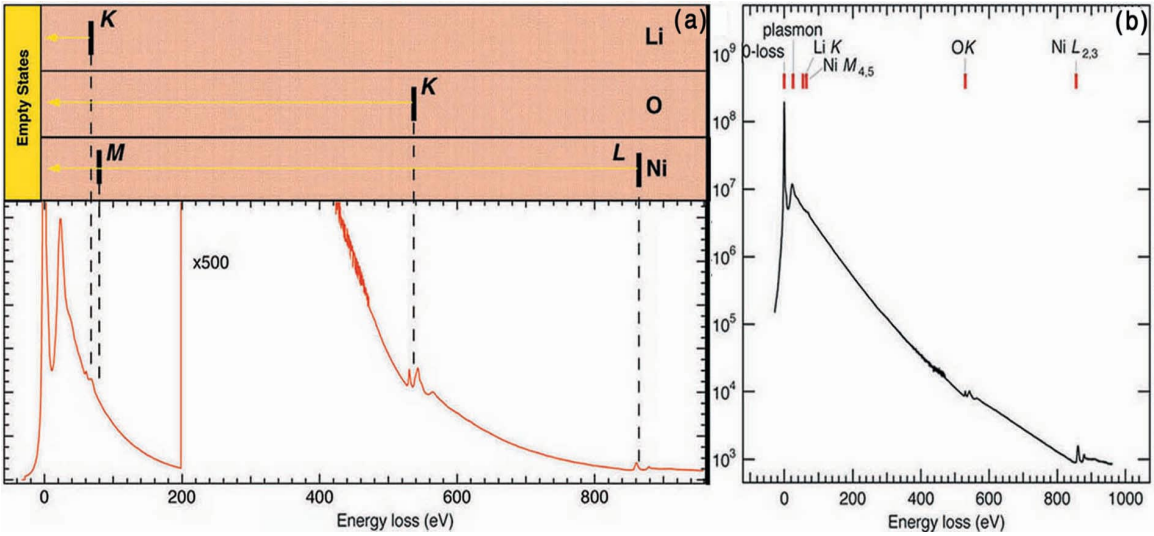

Figure 2.3: Full energy-loss spectrum from $LiNiO_2$ (**a**) with $\times 500$ gain and (**b**) displayed semi-logarithmically. The schematic (**a** top) identifies the different core edges and their associated transitions.

Solutions to the Schrodinger equation ($H\psi = E\psi$) for this Hamiltonian take the form of the product of a radial distribution function, $R_{nl}(r)$, and a spherical harmonic, $Y_l^m(\theta, \phi)$, so that $\psi_{nlm} = R_{nl}(r)Y_l^m(\theta, \phi)$. The energy eigenvalues for a one-electron hydrogenic atom are

$$E_n = -\frac{1}{n^2} Z^2 E_R, \tag{2.3}$$

where E_R is the Rydberg constant (+13.6 eV). The edge onset energy is the energy difference between the initial and final states. In an approximation for multielectron atoms, $Z - Z_S$ replaces Z in Equation 2.3 to correct for the effective screening of the nuclear potential:

$$E_n = -\left(\frac{1}{n'^2} - \frac{1}{n^2}\right)(Z - Z_S)^2 E_R \tag{2.4}$$

$$Z_S = \begin{cases} 1 \text{ for } K\text{-shell transitions} \\ 7.4 \text{ for } L\text{-shell transitions [2]}, \end{cases}$$

where the integers n and n' are the principal quantum numbers for the initial and final states, respectively. Equation 2.4 is known as Moseley's Law.

The shape of the near-edge region is dependent upon the structure of the electronic states above the Fermi energy. In its simplest form, the core edge resembles a saw tooth function. This shape is due to the excitation of bound atomic electrons into a continuum

of occupied states. Transitions into bound atomic states or molecular orbitals often create near-edge structure in the form of discrete peaks just below the ionization energy. The interpretation of near-edge structure is the subject of Chapter 3.

2.1.3 Electron Scattering Theory

The inelastic form factor for the excitation of a core electron can be derived using a bound electron and an incident free electron, whose wavefunction is modeled as a plane wave. A schematic of this scattering event is displayed in Figure 2.4. The incident electron is

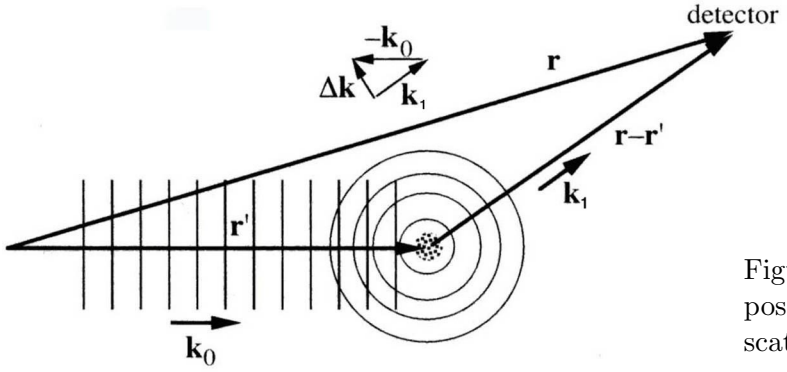

Figure 2.4: Wavevectors and position vectors for electronic scattering from an atom [2].

at a position $\boldsymbol{r}_i$ and is in an initial state $|\boldsymbol{k}_0\rangle$ and final state $|\boldsymbol{k}_1\rangle$. The atomic electron is at a position $\boldsymbol{r}_j$ and is in an initial bound-state $|\alpha\rangle$ and a final state $|\beta\rangle$, which may be another bound state corresponding to a intratomic transition or a free-electron state involving ionization of the atom. As the incident electron approaches the atom the two electron system can be described by the following Hamiltonian:

$$H = H_0 + H', \tag{2.5}$$

where the unperturbed Hamiltonian, H_0,is the sum of the Hamiltonians of the independent electrons:

$$H_0 = H_i + H_j = -\frac{\hbar^2}{2m}(\nabla_i^2 + \nabla_j^2) + V(\boldsymbol{r}_j). \tag{2.6}$$

A perturbation is added to the full Hamiltonian when the two electrons begin to feel each other's presence (through Coulombic forces). The perturbation is the sum of the Coulombic interaction and the potential of the incident electron with the atomic potential, $V(\boldsymbol{r}_i)$,

$$H' = \frac{e^2}{|\boldsymbol{r}_i - \boldsymbol{r}_j|} + V(\boldsymbol{r}_i), \tag{2.7}$$

operating on the full Hamiltonian,

$$\langle \beta \boldsymbol{k}_1 | H | \boldsymbol{k}_0 \alpha \rangle = \langle \beta \boldsymbol{k}_1 | H_0 | \boldsymbol{k}_0 \alpha \rangle + \langle \beta \boldsymbol{k}_1 | H' | \boldsymbol{k}_0 \alpha \rangle. \tag{2.8}$$

The first term in Equation 2.8 is uninteresting because the electrons are not interacting and the initial and final states are the same. However, the second term yields the probability (actually, the square root of the probability) of a transition and is known as the inelastic form factor,

$$f(\boldsymbol{k}_1, \boldsymbol{k}_0) = -\frac{m}{2\pi\hbar^2} \langle \beta \boldsymbol{k}_1 | H' | \boldsymbol{k}_0 \alpha \rangle \tag{2.9}$$

$$= -\frac{m}{2\pi\hbar^2} \langle \beta \boldsymbol{k}_1 | \frac{e^2}{|\boldsymbol{r}_1 - \boldsymbol{r}_j|} | \boldsymbol{k}_0 \alpha \rangle + -\frac{m}{2\pi\hbar^2} \langle \boldsymbol{k}_1 | V(\boldsymbol{r}_i) | \boldsymbol{k}_0 \rangle \langle \beta | \alpha \rangle, \tag{2.10}$$

for an inelastic scattering process with $|\boldsymbol{k}_1| \neq |\boldsymbol{k}_0|$ and $\alpha \neq \beta$. The second term of Equation 2.10 can be eliminated by orthogonality, $\langle \beta | \alpha \rangle = 0$. This expression can be further simplified by making the variable substitutions $\boldsymbol{q} = \boldsymbol{k}_0 - \boldsymbol{k}_1$ and $\boldsymbol{R} = \boldsymbol{r}_i - \boldsymbol{r}_j$. The inelastic form factor can be rewritten as:

$$f(\boldsymbol{q}) = -\frac{2me^2}{\hbar^2 q^2} \int \exp^{i\boldsymbol{q}\cdot\boldsymbol{r}_j} \psi^*_\beta(\boldsymbol{r}_j) \psi_\alpha(\boldsymbol{r}_j) \mathrm{d}^3\boldsymbol{r}_j. \tag{2.11}$$

The inelastic form factor is independent of the incident electron (i) and solely a property of the target atom (j) [25]. The differential cross section for inelastic scattering is

$$\frac{\mathrm{d}\sigma(\boldsymbol{q})}{\mathrm{d}\Omega} = |f(\boldsymbol{q})|^2 = \frac{4}{a_0^2 q^4} \left| \int \exp^{i\boldsymbol{q}\cdot\boldsymbol{r}_j} \psi^*_\beta(\boldsymbol{r}_j) \psi_\alpha(\boldsymbol{r}_j) \mathrm{d}^3\boldsymbol{r}_j \right|^2, \tag{2.12}$$

where a_0 is the Bohr radius, $a_0 = \hbar^2/(2m_\mathrm{e}e^2)$. Equation 2.12 [2] can be written in a more useful form using the following approximation, valid for small $\boldsymbol{q}$:

$$\mathrm{d}\Omega = 2\pi \frac{q}{q^2} \mathrm{d}q. \tag{2.13}$$

One final component to consider when analyzing transition probabilities is the occupancy of the final state. The final expression for the intensity of the core loss region must be weighted by the density of unoccupied states, $\rho(E)$. These final manipulations yield the

double-differential cross section:

$$\frac{\mathrm{d}^2\sigma(\boldsymbol{q},E)}{\mathrm{d}\boldsymbol{q}\mathrm{d}E} = \frac{8\pi}{a_0^2 k_1^2 q^3}\rho(E)\left|\int \exp^{i\boldsymbol{q}\cdot\boldsymbol{r}_j}\,\psi_\beta^*(\boldsymbol{r}_j)\psi_\alpha(\boldsymbol{r}_j)\mathrm{d}^3\boldsymbol{r}_j\right|^2. \tag{2.14}$$

This expression relates the momentum transfer and energy loss to the spectral intensity.[1]. The double-differential cross section can best be understood as the probability of a given transition or, in terms of the energy-loss spectra, as the intensity of a single scattering spectrum.

2.1.4 Dipole Selection Rule

X-rays (and other photons) can be used to excite electric dipole radiation. In the presence of a photon, the atomic electrons are driven by the photon electric field and damped by the Coulomb potential binding the electron to the atom. The harmonic motion of the electron creates an oscillating dipole moment that has resonance frequency, ω_r. X-rays are absorbed by the atom when the resonance energy ($E = \hbar\omega_r$) is sufficient to excite the electron into the next energy level. The available electronic transitions are governed by the dipole selection rule, $\Delta l = \pm 1$. This result can be derived through the angular momentum commutation relations for a spherically symmetric Hamiltonian. This selection rule is expected given that photons have a spin of 1, and conservation of angular momentum dictates that the change in momentum, Δl, must therefore be ± 1 or 0. The latter ($\Delta l = 0$) can be shown to have a transition probability of 0 [26] and therefore the electronic transitions are limited to $\Delta l = \pm 1$.

Electrons are spin 1/2 particles and therefore are not implicitly forbidden from $|\Delta l| > 1$. However, the electronic dipole radiations dominate the core transitions [2]. This can be seen by expanding the exponential part of the integrand from Equation 2.14 in a Taylor series to make the approximation $e^{i\boldsymbol{q}\cdot\boldsymbol{r}_j} \simeq 1 + i\boldsymbol{q}\cdot\boldsymbol{r}_j$ so that

$$\frac{\mathrm{d}^2\sigma(\boldsymbol{q},E)}{\mathrm{d}\boldsymbol{q}\mathrm{d}E} \propto |\langle\beta|1 + i\boldsymbol{q}\cdot\boldsymbol{r}_j|\alpha\rangle|^2 = |\langle\beta|i\boldsymbol{q}\cdot\boldsymbol{r}_j|\alpha\rangle|^2. \tag{2.15}$$

This is known as the "dipole approximation" and is only valid for small $\boldsymbol{q}$. For transitions involving small momentum transfer, the double differential cross section is identical for

[1] Much of this derivation was taken from reference Fultz et al. [2]

photons and electrons. To simplify the data analysis and eliminate non-dipole transitions, a small collection aperture (generally 3 mm) is inserted into the opening of the spectrometer to limit the contributions from electrons with large $\boldsymbol{q}$.[2] Therefore, the interpretation of energy-loss spectra in this study will be based upon electronic transition probabilities that are governed by the dipole selection rule ($\Delta l = \pm 1$).

2.1.5 Noise Reduction and Spectrum Acquisition

A number of methods were employed to reduce noise and instrumental artifacts in the experimental spectra. To minimize energy drifts due to temperature changes in the detector electronics, the microscope and detector were generally turned on two hours prior to the spectral acquisition. A current was applied to the filament 10–20 minutes before acquisition to allow time for the electron beam to stabilize. The energy calibration is extremely sensitive and without the specified warm-up a strong energy drift will lead to an inaccurate energy calibration.

Detector artifacts, such as the unique leakage currents of each diode, were characterized before acquisition by acquiring a series of dark spectra (in the absence of electrons). The calibrated dark current was subtracted from each experimental spectrum in real time. Thermal noise was minimized by cooling the detector elements using a water chiller (typically set at $+10^{\circ}$ C) and a thermoelectric cooler.

The use of a parallel detector, as opposed to a serial detector, has a considerable advantage in efficiency. However, since each channel is unique, it is necessary to account for sensitivity differences among the different channels in the array. The variation in electron response is primarily due to nonuniformities in the phosphorescent screen (the electron to photon converter). These heterogeneities lead to variations in the photon intensity across the detector. In addition, each diode has a unique photonic sensitivity. These instrument artifacts can be mitigated by dividing out a gain calibration spectrum, or instrument response, and by utilizing gain averaging [27]. An instrument response was acquired by applying parallel illumination to the entire detector array and normalizing to the integrated intensity (Figure 2.5). Each experimental spectrum has been normalized by the instrument response. Gain averaging was used to further reduce channel-to-channel heterogeneities

[2] A 3 mm aperture (21 mrad collection angle at a camera length of 70 mm) will collect electrons out to 11 Å^{-1} in k-space (in units of $2\pi/\lambda$).

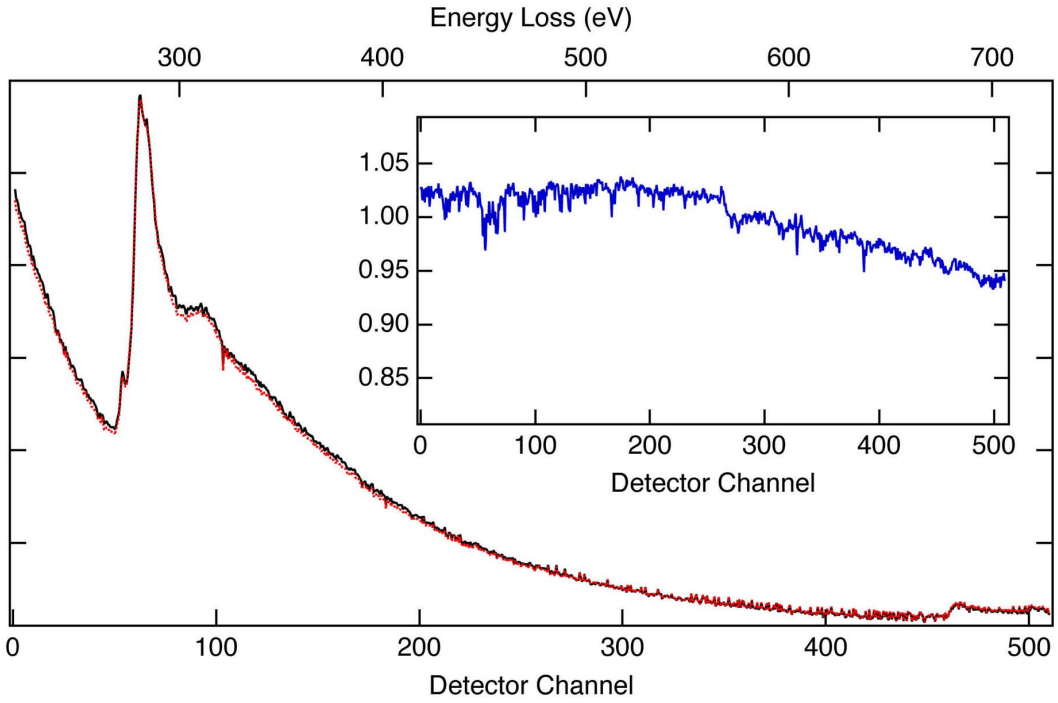

Figure 2.5: Carbon K-edge from CF_x before (solid) and after (dashed) dividing out the normalized gain calibration spectrum (inset). No gain averaging was used on these core edges. The calibration spectrum was acquired from parallel illumination of the detector array. The intensity decay towards higher energies is due to thickness variations of the phosphorescent screen.

(Fig 2.6). In this technique, spectra are acquired at a series of energy offsets. The spectra are subsequently aligned on the zero-loss peak (or a well-characterized core edge) and summed. This technique is particularly useful for eliminating single channel artifacts such as the dip in intensity at 321 eV in Figure 2.6b.

2.2 Quantitative Energy-Loss Spectra

2.2.1 Extracting a Single Scattering Spectrum

To obtain a quantifiable energy-loss spectrum, contributions from plural scattering must be removed. Plural scattering scales with the sample thickness and involves multiple excitations of a single incident electron. Although it is impossible to differentiate individual electrons that have undergone single and multiple energy-loss events, a statistical approximation can be made using a Poisson distribution. This method for removing plural scattering from the energy-loss spectrum is known as the Fourier-log deconvolution [25]. The electron intensity,

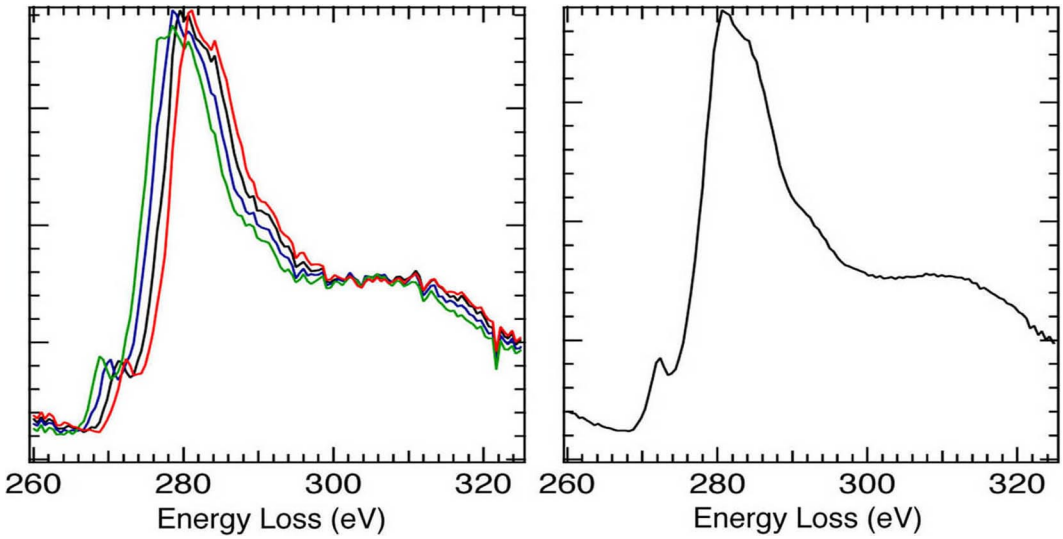

Figure 2.6: (**a**) A series of carbon K-edges from CF_x with energy offsets of 0, 1.5, 3.0, 4.5 eV. An example of a detector artifact is noticeable at 321 eV. (**b**) A smooth carbon K-edge after gain averaging.

I_n, for scattering of order n is determined by the product of the incident intensity, I, with the Poisson distribution, P_n:

$$I_n = IP_n = \int S_n(E) = \frac{I}{n!}\left(\frac{t}{\lambda}\right)^n \exp^{-t/\lambda}, \tag{2.16}$$

where $S_n(E)$ is the scattering intensity distribution, λ is the electronic mean free path and t is the sample thickness (generally t is of the same order as λ). $S_n(E)$ has the following form:

$$S_n(E) = \begin{cases} I_0\delta(E) & \text{for } n = 0 \\ S(E) & \text{for } n = 1 \\ \left[S(E) * S(E)\right]/(2!I_0) & \text{for } n = 2 \\ \left[S(E) * S(E) * S(E)\right]/(3!I_0^2) & \text{for } n = 3, \end{cases} \tag{2.17}$$

where $S(E)$ is defined as the scattering distribution for a single scattering event and $\delta(E)$ represents a delta function. The double and higher order scattering distributions can be written as multiple self-convolutions of the single scattering distribution.

The measured spectrum is slightly different than what is predicted by the sum of the contributions given above. The measured scattering distribution is effectively broadened by the spectral energy resolution, or instrument function. The energy resolution is given by the full-width at half-max (FWHM) of the normalized elastic peak (generally measured

from a spectrum acquired without a sample). The measured scattering distribution, $J_n(E)$, is therefore a convolution of $S_n(E)$ with an instrument function, $R(E)$:

$$J_n(E) = R(E) * S_n(E) = \int_{-\infty}^{\infty} R(E - E')S_n(E')dE', \tag{2.18}$$

A spectrum acquired from multiple orders of scattering $J(E)$ can be expressed as a sum of the different scattering components $J_n(E)$:

$$J(E) = \sum_{n=0}^{\infty} J_n(E) = S_0(E) * \left[\delta + \frac{S(E)}{I_0} + \frac{S(E) * S(E)}{2!I_0^2} + ...\right], \tag{2.19}$$

where $S_0(E)$ is the elastic scattering distribution ($S_0(E) = I_0R(E)$). A Fourier transformation (represented in lower-case) simplifies this expression by converting the multiple convolutions into multiple multiplications. The resulting expression is

$$j(\nu) = s_0(\nu)\left[1 + \frac{s(\nu)}{I_0} + \frac{s^2(\nu)}{2!I_0^2} + ...\right], \tag{2.20}$$

which is simply the power series for an exponential function. The Fourier transform of the full scattering distribution is given by

$$j(\nu) = s_0(\nu)\exp[s(\nu)/I_0]. \tag{2.21}$$

The energy dependence has been transformed into a frequency dependence, ν, with units of E^{-1}. Equation 2.21 can be transformed into the following expression for the Fourier transform of the single scattering distribution [28]:

$$s(\nu) = I_0\ln[j(\nu)/s_0(\nu)]. \tag{2.22}$$

This expression is used to deconvolve the full energy-loss spectrum and reduce it to a single scattering spectrum.

2.2.2 Background Subtraction

Much of the spectral background intensity is due to contributions from the high-energy tails associated with lower energy-loss processes. A quantitative analysis of the spectrum

requires the removal of this background intensity. The high-energy tail (or sum of tails) generally exhibit a power-law dependence,

$$I(E) = AE^{-r}, \tag{2.23}$$

where A and r are constants. Although A is a function of the chemistry of the sample and the beam intensity, it can take on almost any value. The exponent r is function of the specimen thickness and collection angle and is generally $2 \leq r \leq 4$.[3] The energy dependence of the pre-edge region can be approximated by fitting a background within a selected energy window (usually greater than 10 eV). The coefficients are determined from the pre-edge region and extrapolated over the entire edge as shown in Figure 2.7. A

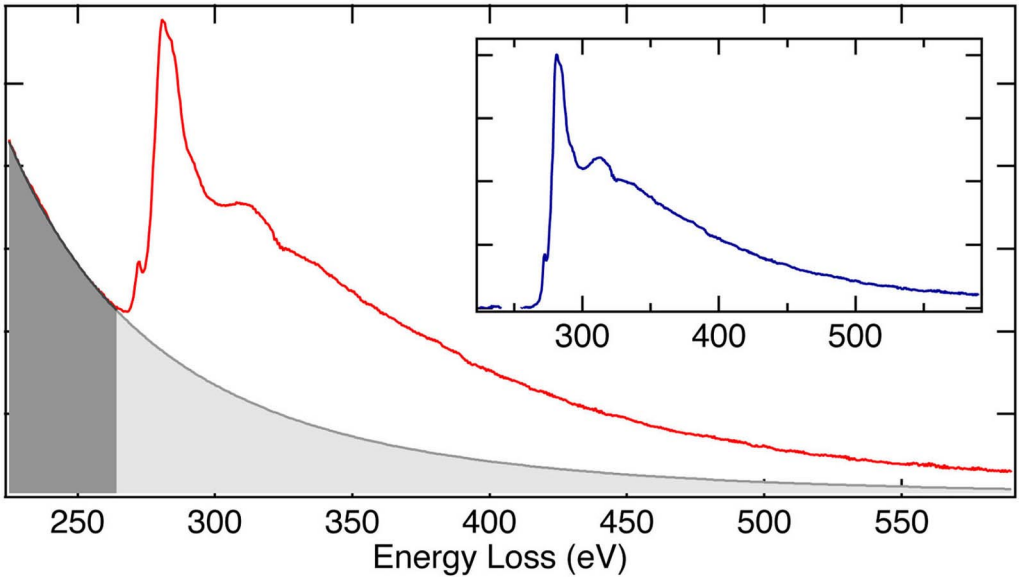

Figure 2.7: Carbon K-edge from CF_x demonstrating the background fitting window (dark grey) and the extrapolated background (light grey). The inset shows the background subtracted carbon K-edge.

reasonable background approximation will closely fit the pre-edge region and will approach zero at high energy losses.

2.2.3 Elemental Analysis

One of the most common reasons for quantifying the core edges is to perform an elemental analysis. The integrated intensity of the inner-shell edge, I_k (where $k = K,\ L,\ M,\ ...$), can

[3]Egerton gives a value of $2 \leq r \leq 6$ [25] but r is rarely, if ever, larger than 4.

be used to determine the amount of one atomic species, N_α, to another, N_β. When the sample is suitably thin (< 100 nm), and the spectrum is properly deconvolved, the following approximation is reliable:

$$I_k(\Delta) = N_k \sigma_k(\Delta) I_0 \rightarrow \frac{N_\alpha}{N_\beta} = \frac{I_{\alpha k}}{I_{\beta k'}} \frac{\sigma_{\beta k'}}{\sigma_{\alpha k}}, \tag{2.24}$$

where the integration range is from E_k to $E_k + \Delta$, $\sigma_k(\Delta)$ is the reduced cross section, and I_0 is the zero loss intensity.

2.2.4 Energy Filtered Imaging

Energy filtered imaging is a relatively recent technique used to perform chemical and valence state mapping of a solid. In this technique, an energy filter, such as an omega filter, and a 2-D detector are used to produce an image of inelastically scattered electrons. An energy window is chosen so that contributions to the image intensity are limited to electrons within a specific energy distribution. Provided the sample is thin (< 100 nm) electron spectroscopic imaging will produce elemental maps, which have been demonstrated in a variety of systems such as structural ceramics [29] and metal/metal interfaces [30]. In addition to chemical mapping, valence state mapping has recently been performed on various transition metal oxides [31, 32]. These studies have produced 2-D images that clearly reveal the distribution of valences in a multivalent manganese oxide.

2.3 Other Analytical Methods

Electron energy-loss spectrometry is a similar analytical technique to x-ray absorption spectroscopy, which measures the energy differences between incident and transmitted X rays. Generally the high fluxes needed for such an experiment require a synchrotron radiation source. The ionization edges accessible to soft X rays ($12\,\text{Å} < \lambda < 120\,\text{Å}$) are similar to those measured in EELS (100 eV$< E <$ 1000 eV). Hard X rays ($\lambda <$ 12Å) are able to access higher energy ionization edges ($E >$ 1000 eV) but are generally unable to measure the low-energy ionization edges.

Another spectroscopic technique involving the excitation of core electrons is x-ray photoelectron spectroscopy (XPS). XPS uses incident X rays to excite a photoelectron to directly

probe the filled valence states, whereas EELS probes unoccupied states. Electron energy-loss spectrometry and XPS can both provide information about bonding. However, XPS is limited to the study of surfaces owing to the short mean free path of photoelectrons ($\sim$ 1 nm). Conversely, the 100 keV electrons used in EELS have a long mean free path and are therefore sensitive to the bulk properties of a material.

Chapter 3 Electron Energy-Loss Spectrometry of Transition-Metal Oxides

3.1 Introduction

Electron energy-loss spectrometry is a useful technique for characterizing the chemical, structural, and electronic properties of a solid. The $3d$ transition-metal (TM) oxides are well suited to this technique due to their low energy core edges (< 1 keV) and their inherent stability under a high-energy electron beam. The TM oxides exhibit a variety of crystalline and electronic properties, which are often reflected in the core edges of the energy-loss spectrum [33, 34, 35]. The near-edge structure of the core edges are of specific interest because they reflect a density of unoccupied states for a given atom, which can be used to characterize valences and atomic bonding. This section is intended to illustrate some spectroscopic features and trends in the near-edge structure of the TM oxides that may offer insight into more complex systems, such as the $LiTMO_2$.

3.2 The Oxygen K-edge

To a first approximation, the oxygen K-edge represents the p-projected density of unoccupied states for the oxygen atom. Figure 3.1 shows the experimental oxygen K-edge from several TM oxides. In these materials the oxygen K-edge can be partitioned into two main regions. The region 5–10 eV above the edge onset (labeled peak a) is dominated by transitions into unoccupied states of oxygen $2p$ character. The strong hybridization of the oxygen $2p$ and the highly localized TM $3d$ states creates holes in the oxygen $2p$ band [37]. The separation of peak a in TiO_2 is attributed to a ligand-field splitting (the energy gap between t_{2g} and e_g states) and exchange splitting (the spin-up and spin-down energy difference). Intensity contributions to the region 10 eV to 30 eV above the threshold (labeled peaks b–d) are often attributed to transitions into oxygen $2p$ states hybridized with the TM $4s$ and $4p$ bands [37, 36, 38]. However, the oxygen $2p$ density of states (DOS) is minimal 20 eV above the threshold and the TM $4sp$ states are free-electron-like and do not form localized bands

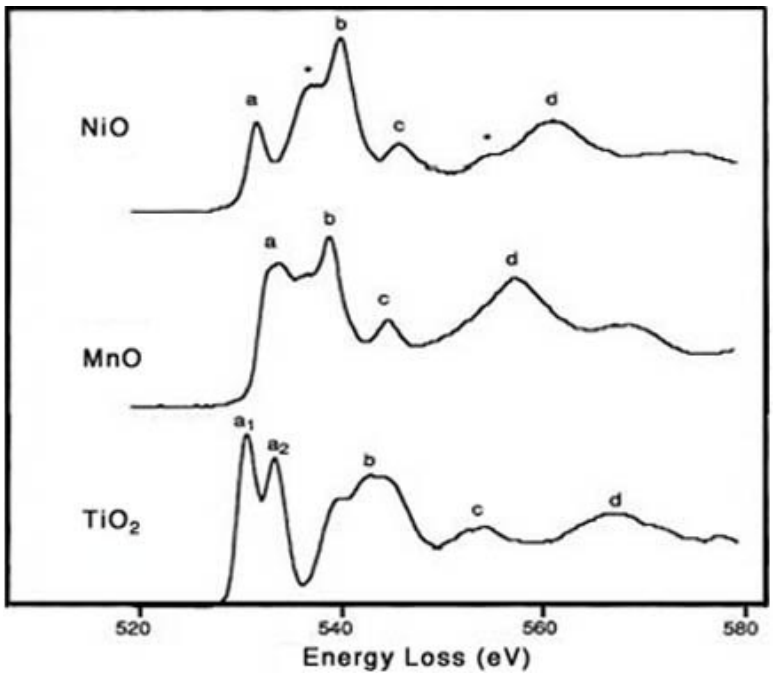

Figure 3.1: Energy-loss spectra of the oxygen K-edge from several TM oxides after deconvolution and background subtraction [36].

like the TM $3d$ states. Therefore, the oxygen $2p$ - TM $4sp$ band will contribute little to the structure at energy losses greater than ~ 15 eV above the edge onset. The peak structure is best explained by electronic scattering off of various oxygen shells. Specifically, peak b is attributed to intrashell multiple scattering within the first oxygen shell [36, 39, 40], peak c is the result of intershell multiple scattering from outer lying oxygen shells, and peak d is due to single scattering from the first oxygen coordination [36].

The sensitivity of the oxygen K-edge to the ligand-field and exchange splitting is exhibited in the near-edge structure of the manganese oxides[1] (Figure 3.2a). A series of molecular orbital diagrams (Figure 3.3) demonstrate the differences in the exchange and ligand-field splitting energies between MnO, Mn_2O_3, and MnO_2. In MnO, the oxygen K-near-edge structure manifests a single pre-peak. The 1.4 eV separation between the unoccupied t_{2g} and e_g states is sufficiently large to split this peak; however, transitions into the t_{2g} band have a much higher probability owing to the abundance of $2p$ holes when compared with the e_g band. In contrast, exchange and ligand-field interactions in Mn_2O_3 divide the near-edge structure into three peaks. Peak a_1 is the result of transitions into e_g (spin-up) states, which are separated by 1 eV from peak a_2, which is due to transitions into t_{2g} (spin-down) states. 3.4 eV separates peak a_2 from a_3, which is attributed to transitions into e_g (spin-down)

[1]Spectra from manganese oxides were acquired by Andrea Belz.

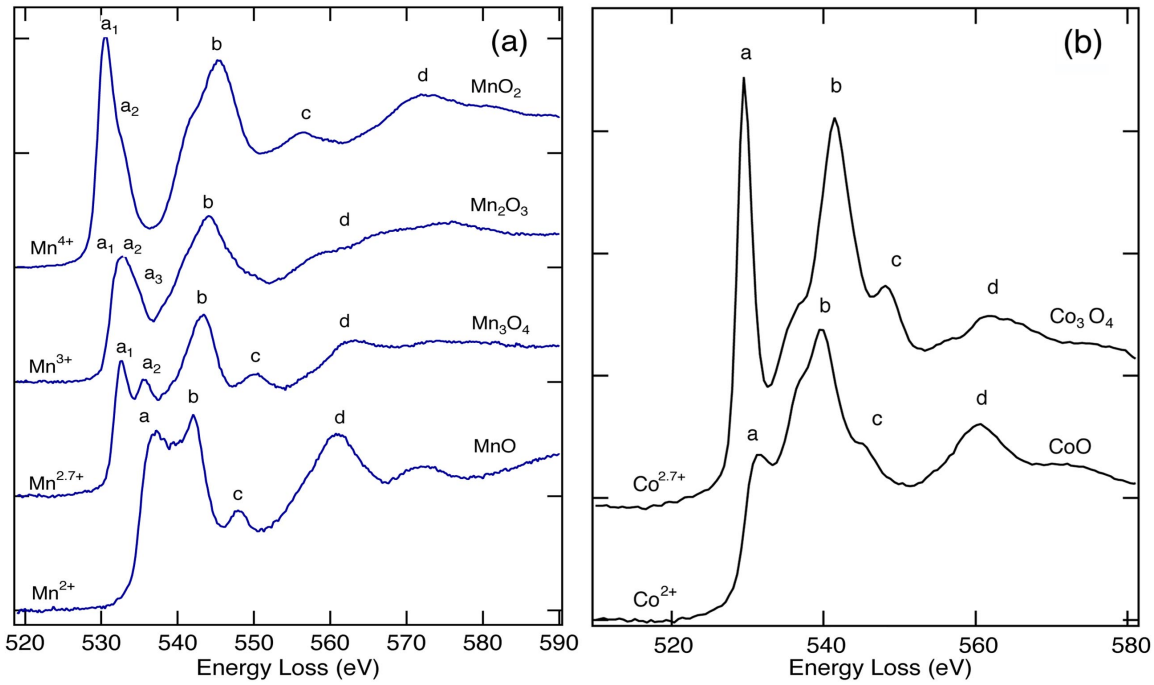

Figure 3.2: Energy-loss spectra of the oxygen K-edge from a series of (**a**) manganese and (**b**) cobalt oxides after background subtraction.

states. The near-edge structure of MnO_2 is similar to that of Mn_2O_3 however, the effect of the ligand-field and exchange interactions combine such that the t_{2g} (spin-down) and e_g (spin-up) states overlap in energy to form peak a_1, while peak a_2 is the result of transitions into higher energy e_g (spin-down) states [38].

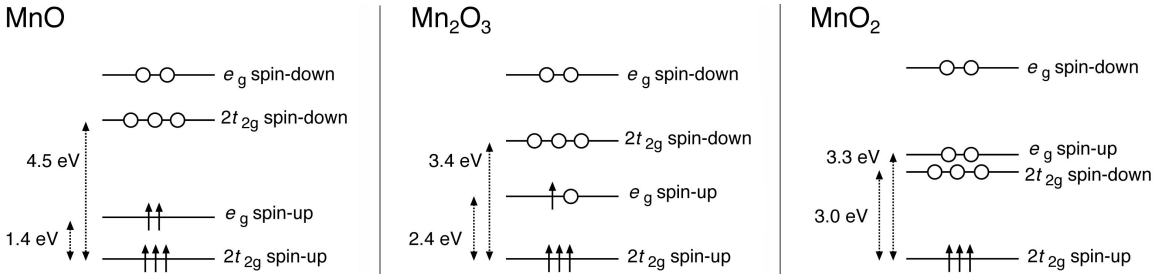

Figure 3.3: Molecular orbital diagram demonstrating the relative energies of the t_{2g} and e_g levels for MnO, Mn_2O_3, and MnO_2 [3].

In addition to the manganese oxides, the cobalt oxides are another set of compounds that are chemically similar and yet exhibit very different ionization edges. A plot of the oxygen K-edges from CoO and Co_3O_4 is shown in Figure 3.2b. In CoO, the cobalt ions have a 2+ valence and are octahedrally coordinated by oxygen atoms. Co_3O_4 has a spinel structure and

consists of mixed valent cobalt with one third of the ions occupying tetrahedral sites (Co^{2+}) and the remaining two thirds in octahedral sites (Co^{3+}). The large peak (a) observed in the near-edge structure (530 eV) of the Co_3O_4 oxygen K-edge is due to bound-state transitions from $1s$ states into $2p$ states. This structure is absent in materials containing ionically bonded oxygen such as in CoO. In ionic TM oxides there are six electrons localized in the $2p$ band and therefore, the bound transition $1s \rightarrow 2p$ is prohibited. The availability of this transition requires unoccupied $2p$ states, which are formed by a strong O $2p$ - TM $3d$ hybridization. Therefore, the intensity of this near-edge peak is indicative of the number of oxygen $2p$ holes as well as a measure of the degree of covalency of the TM - O bond [37, 41, 42].

3.3 The $L_{2,3}$-Edge and White lines

The $L_{2,3}$-edges of the $3d$ transition metals are a unique and easily identifiable feature of the energy-loss spectrum. The $L_{2,3}$-edge can best be described as independent overlapping L_2 and L_3-edges, which are the result of transitions from $2p$ states into bound $3d$ and continuum states. A spin-orbit coupling splits the degeneracy of the $2p$ states into $2p_{1/2}$ and $2p_{3/2}$ levels, and thus creating two independent L edges. The TM $L_{2,3}$-edge is characterized by two intense peaks at the onset of the edge, which are known as white lines. The $L_{2,3}$ white lines are the result of transitions from $2p$ states into the tightly bound $3d$ states near the Fermi level. The $L_{2,3}$-edge contains information regarding the valence state and bonding of the TM ion.

The manganese $L_{2,3}$-edges from various manganese oxides are displayed in Figure 3.4a. The most salient feature of this plot is the dependence of the onset energy on the oxidation state of the manganese ion. This is seen as a shift of the edge onset to higher energy from 637 eV to 639 eV with increased valence from Mn^{2+} to Mn^{4+}. The fine structure of the manganese $L_{2,3}$ white lines is due to the atomic multiplet structure, which results from $3d$–$3d$ and $2p$–$3d$ interactions as well as a cubic-crystal-field coupling [37].

The cobalt $L_{2,3}$ white lines from CoO and Co_3O_4 (Figure 3.4b) exhibit similar near-edge structure. The onset energy of the L_3 line is slightly higher in the Co_3O_4 spectrum, which conforms to the trend of the L_3 onset energy scaling directly with the TM valence.

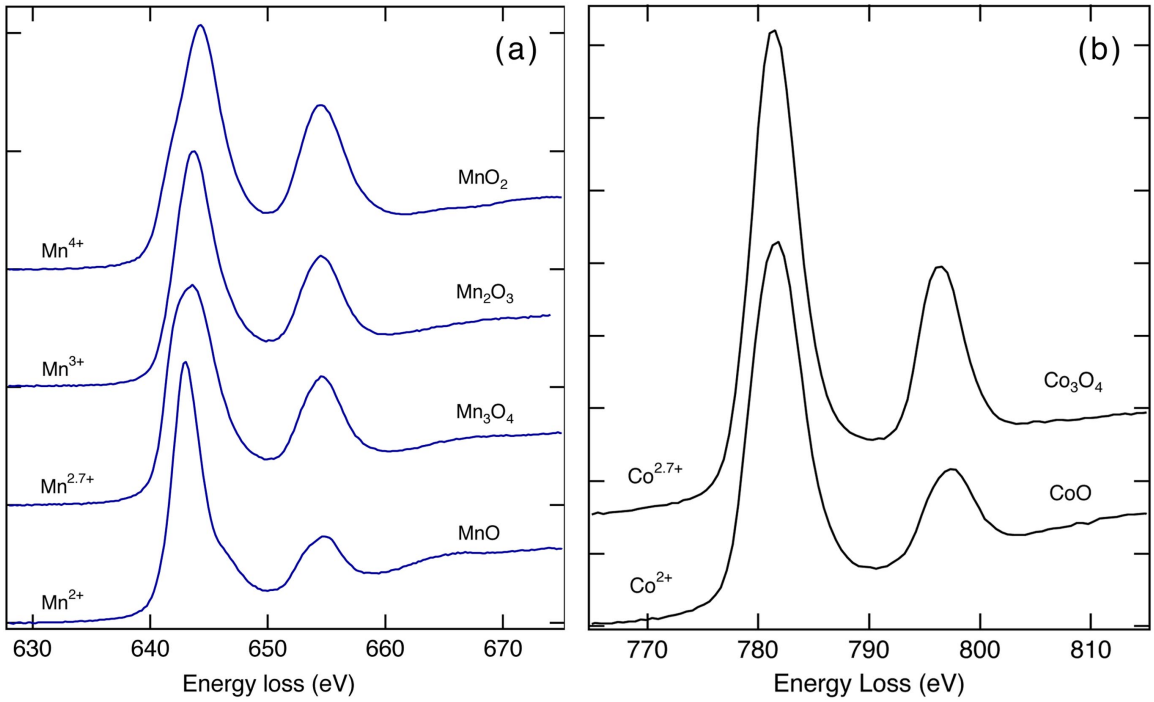

Figure 3.4: Energy-loss spectra of the (**a**) manganese and (**b**) cobalt $L_{2,3}$-edges from a series of manganese and cobalt oxides after background subtraction.

3.4 White Lines of the $3d$ Transition Metals

To understand changes in white line intensities in more complicated TM compounds, a systematic study of $L_{2,3}$-edges from $3d$ TM oxides and $LiTMO_2$ was performed. The integrated white line intensity is a measure of the number of unoccupied states, or holes, in the $3d$ electron band [43, 44, 45]. This work is an extension of an earlier study by Pearson et al [46, 47]. In this study, the normalized white line intensity is used as a measure of the d occupancy of a transition metal. An inverse linear relationship between the integrated white line intensity and the atomic number (d occupancy) is well documented for the $3d$ transition metals [46, 47]. The white line intensity is representative of the component of the $3d$ band locally projected onto the $3d$ atomic states at the TM atoms. In an equivalent description, the white lines intensity is representative of the number of $2p \rightarrow 3d$ excitations. The probability of an excitation is dependent upon the density of unoccupied $3d$ states (Equation 2.14).

3.4.1 Experimental

The TM oxide samples were prepared by thermal evaporation on single-crystal NaCl substrates in vacuum (10^{-5} torr). The samples were annealed in air at 350° C for two hours to oxidize the films and subsequently floated onto a holey carbon grid in water. The TM oxide spectra were collected using a Gatan 607 spectrometer on a Jeol-200CX TEM operating at 200 kV. The lithium TM oxide powders were crushed in Fluorinert^{TM} with a mortar and pestle and the particles were floated onto a holey carbon grid. The spectra for these samples were acquired using a Gatan 666 spectrometer on a Philips EM420 at 100 kV.

3.4.2 Spectral Analysis

Before quantifying the $L_{2,3}$ white line intensity, the contributions to the edge intensity from extraneous sources was eliminated. The dark current was subtracted from the spectrum and detector artifacts were removed by gain averaging and by dividing out an instrument response. The plural scattering was removed using a Fourier-log deconvolution and the background was approximated as a power-law and subtracted from the core edge. The spectral intensity was partitioned into contributions from bound state transitions (forming the white lines) and transitions into delocalized states. The intensity due to continuum (free-electron-like) transitions was removed to restrict the analysis to bound $3d$ transitions. The free-electron-like contributions to the core edge generally take the form of a step function [46, 47]. Figure 3.5a displays a typical TM $L_{2,3}$-edge where the free-electron-like contributions to the L_3 and L_2 edges are identified in windows A_1 and A_2, respectively. A simplified approach assumes that all of the intensity below the Lorentzian peaks originates from continuum transitions (Fig 3.5b). To quantify the white line intensity, the continuum component of the near-edge structure is removed and the total $L_{2,3}$ white line intensity is normalized to a continuum window (Figure 3.5b window B). The spectral intensity from a transition of a bound electron in a $|2p\rangle$ state to an excited $|3d\rangle$ state is the product of the inelastic form factor governing the transition and the density of unoccupied states $\rho(3d)$:

$$I = \rho(3d)|\langle 3d| \exp[i\boldsymbol{q}\cdot\boldsymbol{r}]|2p\rangle|^2. \tag{3.1}$$

Therefore, the total white line intensity is the sum of all the transitions within a given energy region. In this experiment the white line intensity ($E_0 \leq E \leq E_1$) has been normalized to

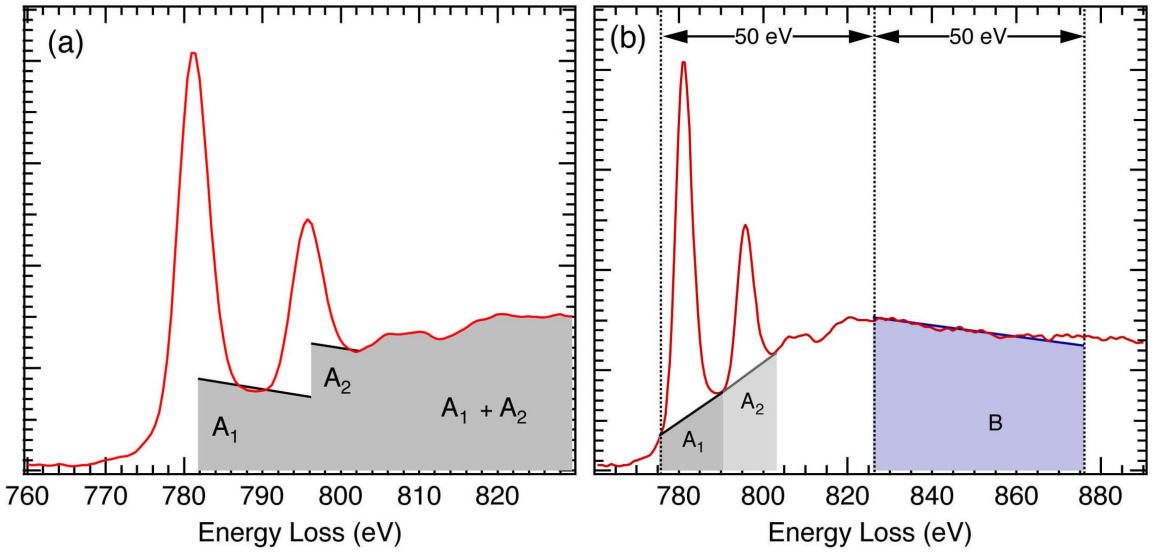

Figure 3.5: A typical TM $L_{2,3}$-edge showing (**a**) the free-electron-like contributions to the white line intensity (A_1 and A_2). In (**b**) the free-electron-like contributions are approximated as the intensity below the peaks. A 50 eV window located 50 eV above the L_3 onset, B, was used to normalize the white line intensity.

a continuum window ($E_0 + 50$ eV$\leq E \leq E_0 + 100$ eV) to give the following expression for the measured intensity:

$$I = \rho(3d)\frac{\int_{E_0}^{E_1} |\langle 3d|\exp[i\boldsymbol{q}\cdot\boldsymbol{r}]|2p\rangle|^2 \mathrm{d}\varepsilon}{\int_{E_0+50}^{E_0+100} |\langle 3d|\exp[i\boldsymbol{q}\cdot\boldsymbol{r}]|2p\rangle|^2 \mathrm{d}\varepsilon}, \tag{3.2}$$

where E_0 is the edge onset energy and E_1 is the energy at the trailing edge of the L_2 line, typically $E_1 \approx E_0 + 30$ eV.

3.5 Results and Discussion

3.5.1 White Line Intensity

The oxygen K and TM $L_{2,3}$-edges from a number of TM oxides and $LiTMO_2$ are displayed in Figure 3.6. A plot of the relationship between the integrated white line intensity and the $3d$ occupancy is shown in Figure 3.7. The composition of the TM oxides (x in TMO_x) was determined through an elemental analysis of the TM and oxygen core edges as given by Equation 2.24. The lithiated samples were analyzed as received and therefore, the stoichiometric values were used for the chemical composition. The $3d$ occupancy was determined

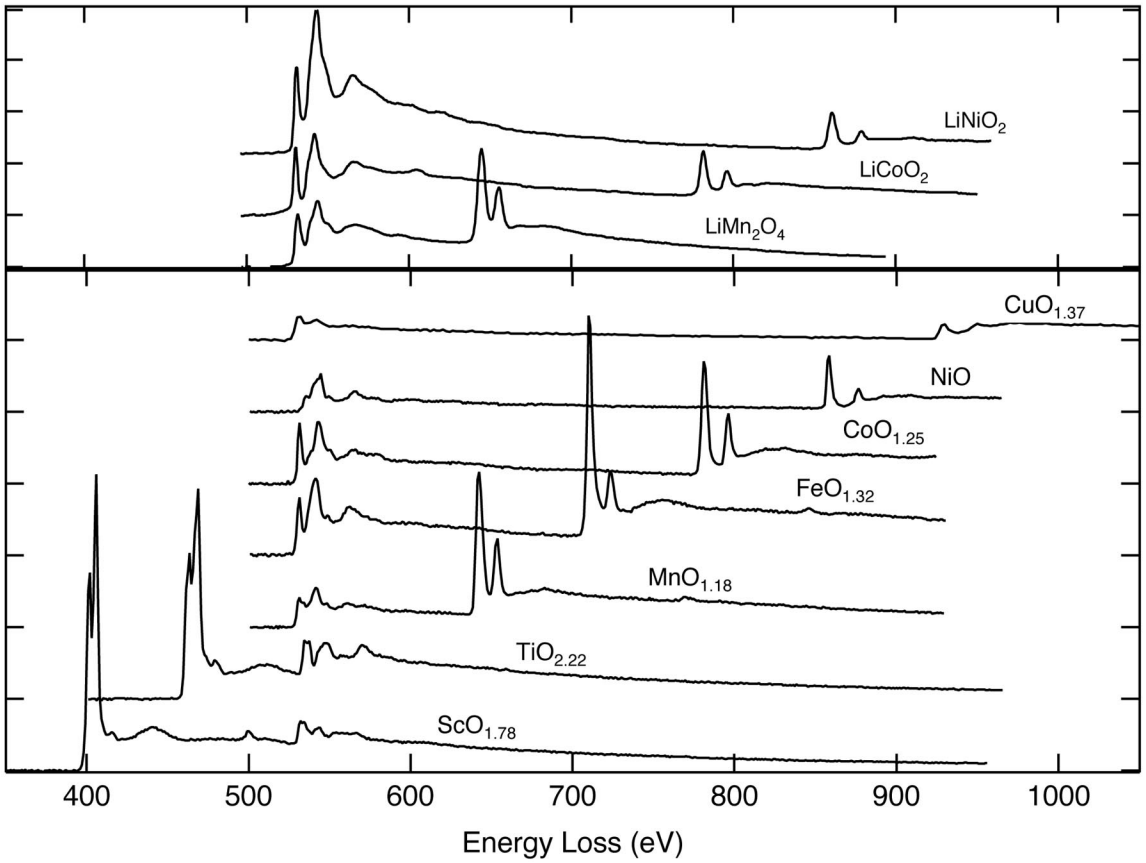

Figure 3.6: Energy-loss spectra of the oxygen K and TM $L_{2,3}$-edges from a series of $LiTMO_2$ (top) and a series of TM oxides (bottom).

by assuming that each oxygen atom removed (or oxidized) two electrons from each TM ion[3] and that the TM ions relinquished their $4s$ electrons first, followed by their $3d$ electrons. In the elemental state (prior to oxidation), each of the transition metals has two $4s$ electrons except chromium and copper, which have one. In this method, the $3d$ occupancies of scandium and titanium oxide are negative, suggesting that the oxidation extends into the $3p$ band. The $3d$ occupancy of these oxides was assumed to be zero.

Figure 3.7 clearly demonstrates a linear relationship between the d occupancy and the white line intensity in the $3d$ TM oxides. This relationship has the following form:

$$I = I_0 + \gamma n_d \quad \text{where } I_0 = 1.32 \text{ and } \gamma = -0.123, \tag{3.3}$$

where the fitting coefficients are given, I is the normalized white line intensity, and n_d is the

[3]except for nickel in $LiNiO_2$, which seems to be closer to 2+ [48]. The oxygen ion in these systems is believed to compensate for more than two electrons. This subject is covered *ad naseum* in Chapters 4–5.

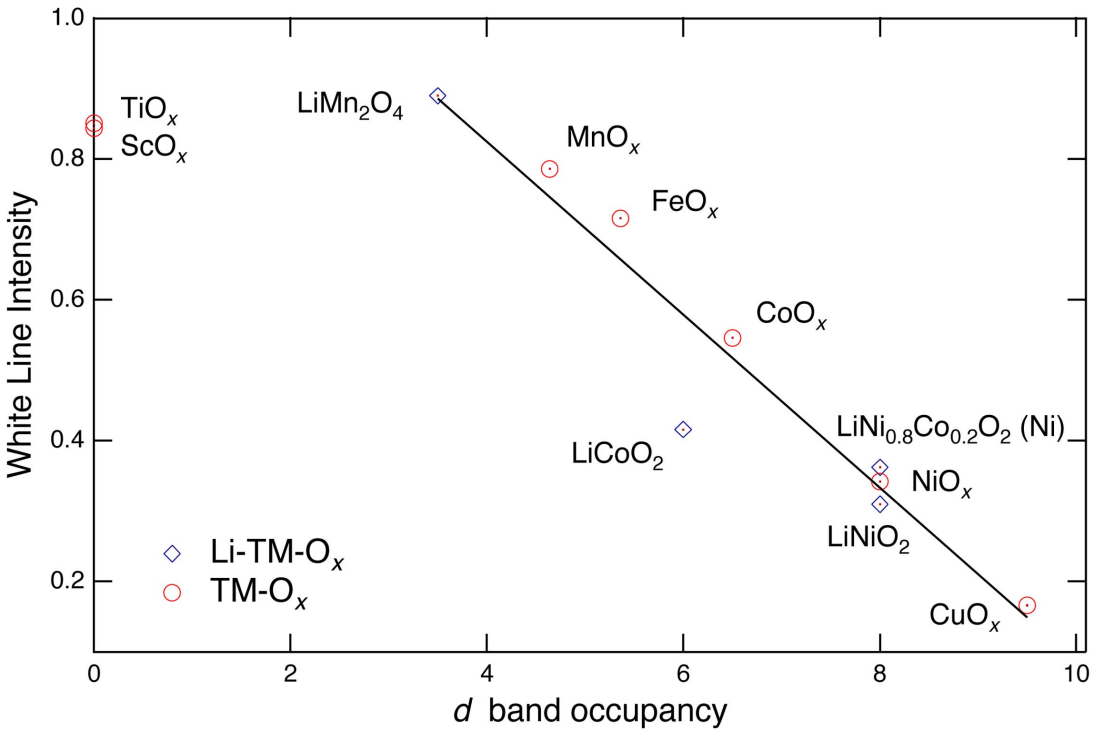

Figure 3.7: Normalized white line intensity for a series of TM oxides and lithium TM oxides. For $LiNi_{0.8}Co_{0.2}O_2$ the relevant transition metal ion is indicated in parentheses.

number of d electrons. The fit has a linear correlation coefficient -0.96. These results are in agreement with those of Pearson et al. who found values of $I_0 = 1.06$ and $\gamma = -0.1$ for the $3d$ transition metal series [47]. In this study, the white line intensity measured for the scandium and titanium oxides does not conform to this linear relationship and therefore, was not included in this linear fit. The departure from linearity is attributed to a different degree of hybridization in the Sc-O and Ti-O bonds. Despite these deviations, the empirical relationship established in Equation 3.3 is a reliable standard for measuring d occupancy in the $3d$ transition metals.

3.5.2 White Line Ratios

Another method for extracting valence information from quantified energy-loss spectra is through the white line ratio (L_3/L_2). When the initial and final states are uncoupled, the white line intensity ratio has a statistical value of 2. The p states have a degeneracy of $2j + 1$ and therefore, there are twice as many $j = 3/2$ (L_3) electrons as there are $j = 1/2$ (L_2) electrons. Deviations from this value have been reported in d transition metals and

lanthanide compounds [45, 49, 4, 50, 51, 52, 53]. These deviations are correlated with the configuration of the outer electron shell.

The nonstatistical value of the white line ratio (i.e., a departure from 2) has been shown to vary with the d occupancy across the $3d$ transition metal series [49, 4, 50, 51]. Figure 3.8 reveals an increasing L_3/L_2 ratio with the filling of the $3d$ states up to approximately FeO_x ($d^{5.3}$) where $L_3/L_2 \approx 5.0$. Subsequent filling of the d states reduces the white line ratio. This is in agreement with results of Sparrow et al. who have found that in TM oxides, the white line ratio is at a minimum in the d^0 and d^9 configurations and reaches a maximum of 4.8 when the d states are half full [4].

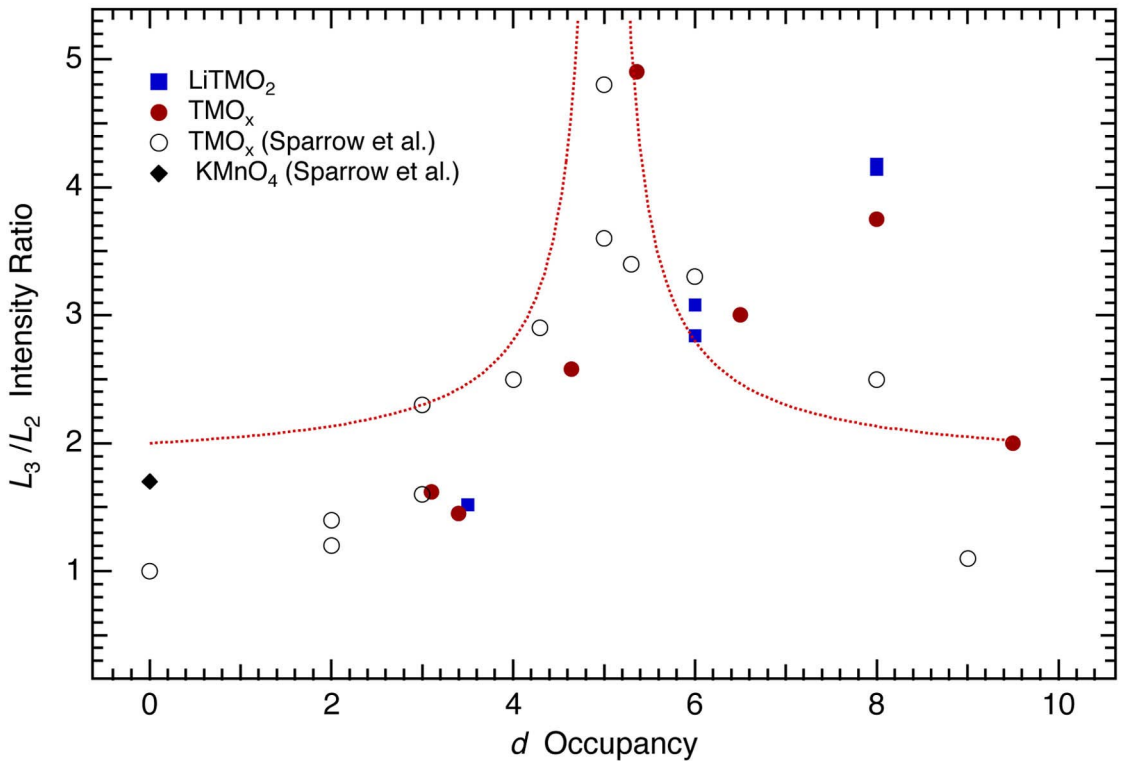

Figure 3.8: Branching ratio for a series of TM oxides and $LiTMO_2$. The data of Sparrow et al. were taken from the literature [4]. The dotted curve was fit to the data using Equation 3.4.

The ratio of the L_3 to L_2 line depends on the interaction between the core-hole and the valence electrons. The core-hole is created when the core electron undergoes a transition into an excited state. The trend in the anomalous white line ratio across the $3d$ TM oxides is due to a spin-spin interaction between the $3d$ electrons and the $2p$ hole. In addition to the j-degeneracy, the L_2 and L_3 transition probabilities will be determined by the d

occupancy, n_d. From $0 < n_d \leq 5$ the d states are filled with spin-up electrons, increasing the atomic moment (spin-spin). As the spin-up states are filled, the L_2 probability decreases to zero at $n_d = 5$. Since the number of spin-down states are unchanged when $n_d \leq 5$ the L_3 probability is constant and the net effect is an increase in the L_3/L_2 ratio. Similarly, from $5 < n_d \leq 10$ the d states are filled with spin-down electrons, reducing the spin-spin coupling and simultaneously reducing the probability of an L_3 transition. In this region the L_2 transition probability remains constant and the L_3/L_2 ratio decreases. In the absence of a spin-spin interaction ($n_d = 0$ and $n_d = 10$) the white line ratio should be exactly 2. This argument is based upon the assumption that the atomic moment is generated by a $2p$ core-hole and $3d$ valence electron that have the same z-axis. A primitive fitting function was developed based upon this concept. The L_3/L_2 ratio, I, across the TM series is given by

$$I = I_0 + c\left(1 - \left|\frac{5}{5 - n_d}\right|\right), \tag{3.4}$$

where I_0 is the statistical value for the white line ratio, 2, and c is a fitting constant. This function represents the appropriate trend expected from a spin-spin interaction and provides a reasonable fit to the data.

3.6 Conclusion

A well-documented relationship exists between the $L_{2,3}$-edge onset energy and the TM valence. Our results indicate that the valence state of the TM ion is also reflected in the white line intensity. In this study, an empirical relationship between white line intensity and d occupancy has been established for the $3d$ transition-metal oxides. The linear fit for the later transition metal white line intensities can be used to characterize the d occupancies in new systems. In addition, an obvious trend is apparent in the white line ratio across the $3d$ series, which is explained by an interaction between the core-hole and the valence electrons.

Chapter 4 Electronic Structure and Charge Compensation in $LiCoO_2$

4.1 Introduction

It has traditionally been accepted that in lithium metal oxides ($LiTMO_2$), the valence of the transition metal compensates for the charge on the intercalated lithium. In the intercalated state, there is nearly complete charge transfer from the lithium ion to the TMO_2 host. With the assumption that oxygen is fixed at O^{2-}, charge neutrality requires a trivalent TM ion for the composition $LiTMO_2$. As Li^+ is removed from the structure, local regions of composition TMO_2 must have metal atoms with valence TM^{4+}. The assumption that the oxygen valence is virtually unaffected by lithium intercalation, requires that charge compensation during lithium intercalation occurs at the TM atoms.

On the contrary, recent calculations suggest that the oxygen valence plays the dominant role in accepting the incoming charge [54, 55]. Similarly, experimental data using x-ray photoemission spectroscopy (XPS) and x-ray absorption spectroscopy (XAS) have demonstrated a decrease in oxygen $2p$ holes during lithium intercalation indicating an increase in electron density in the vicinity the oxygen ion [56, 57].

In this study, EELS was used to investigate the valence of the cobalt and oxygen ions. As mentioned in Chapter 3, the core-edges in the energy-loss spectrum provide chemical information on the bonding and the oxidation state of the ion. The near-edge structure of the oxygen K-edge and the cobalt $L_{2,3}$-edge white lines were used to probe the density of unoccupied states near the oxygen and cobalt ions, respectively. We confirm that in $LiCoO_2$ the lithium $2s$ electron is compensated by oxygen $2p$ states rather than TM $3d$ states, as is traditionally accepted.

Interpretation of the near-edge structure in the energy-loss spectrum requires an understanding of the nature of the Co-O bond, which is strongly covalent in $LiCoO_2$. The covalent bond can be viewed as combinations of oxygen $2p$ and cobalt $3d$ atomic orbitals with bonding and antibonding eigenstates. The electron donated during the intercalation of lithium will enter these molecular orbitals, but it is not obvious on which atomic site the

probability of the donated electron will be highest. From the layered structure of $LiCoO_2$, however, with the lithium layer near oxygen atoms, we might guess that the oxygen ion is most involved in the charge transfer.

4.2 Experimental

Sample preparation began with stoichiometric $LiCoO_2$ powder supplied by Enax Inc. This material was delithiated chemically using an aqueous solution of potassium persulfate ($K_2S_2O_8$). The details of the chemical delithiation process are covered in Appendix A. Elemental analysis was performed by Reminex, Inc. using an inductively-coupled plasma - mass spectrometer (ICP-MS). The samples were found to have the composition of $Li_{1-x}CoO_2$ with $x = -0.02$, 0.09, 0.12, 0.20, 0.28. X-ray diffraction (XRD) patterns were measured with an Inel CPS-120 diffractometer with cobalt $K\alpha$ radiation ($\lambda = 1.790$ Å). X-rays were detected using a wide-angle (120°) position sensitive detector with the ability to detect shifts of features on the order of 0.1°.

For TEM analysis, the samples were crushed with a mortar and pestle in Fluorinert^{TM} and the powder was dispersed onto a holey carbon grid. The EELS spectra were acquired using a Philips EM 420 transmission electron microscope and a Gatan 666 parallel-detection EELS spectrometer. The energy resolution of the spectrometer was approximately 1.5 eV with a dispersion of 0.5 eV per channel. Energy-loss spectra were acquired with diffraction coupling (image mode) using 100 keV electrons and a collection angle of approximately 100 mrad. This large collection angle includes the entire Bethe ridge from valence electron excitations as part of the background, which occurs at 72 mrad in the region of the oxygen K-edge for 100 keV electrons.

4.3 Results

In layered $LiTMO_2$ the lithium ions act as a Madelung "glue" between oxygen layers. The removal of lithium causes an increase in the interplanar distance between the basal planes and a decrease in the interatomic distance within the basal planes [58, 59]. The screening provided by the lithium ions reduces the effective Coulomb repulsion between oxygen layers, thereby decreasing the interplanar spacing [59]. This change is evident in

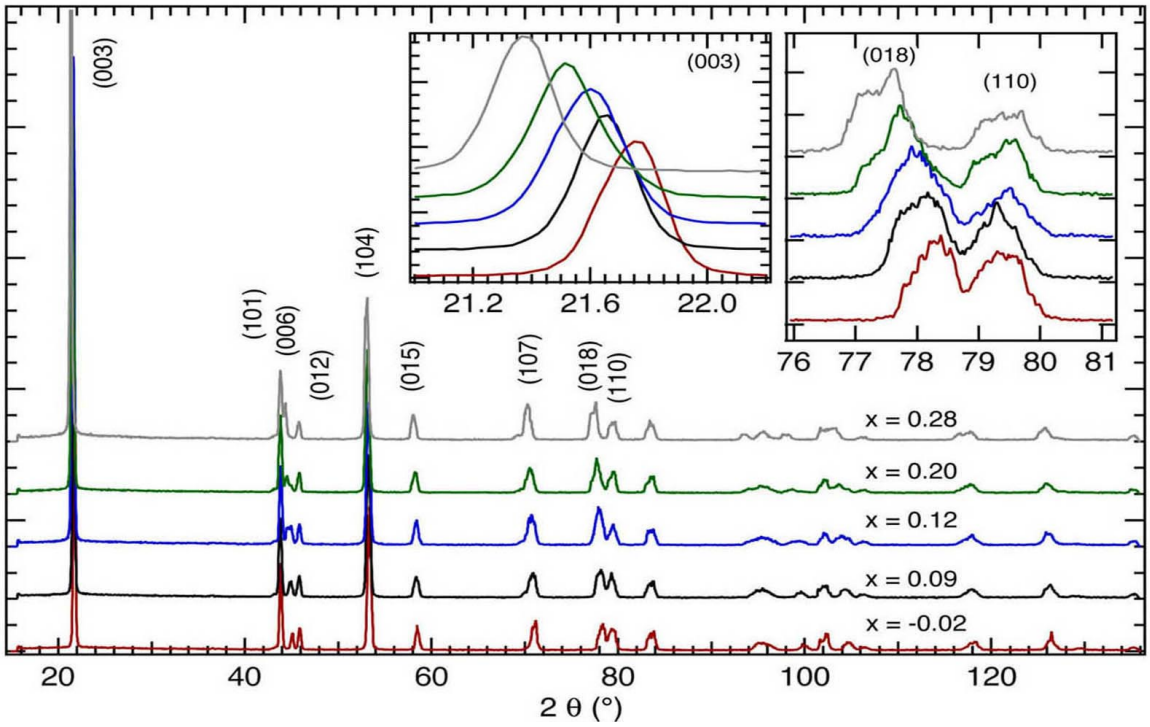

Figure 4.1: X-ray diffraction pattern from chemically delithiated $Li_{1-x}CoO_2$ with insets showing the shift of the (003) peak and the splitting of the (018) and (110) peaks.

the (003) XRD peak from the delithiated $Li_{1-x}CoO_2$ displayed in Figure 4.1. There is a consistent shift in these peaks to smaller 2θ angles, indicating an increase in the c lattice parameter attributable to the lithium depletion. This shift is well documented by Reimers and Dahn [60], who have shown that the (003) peak disappears with lithium deintercalation at $x \approx 0.07$ and that a new peak reappears at a slightly lower angle. This defines a first-order phase transition to a distorted hexagonal phase for $0.25 < x < 0.07$ [60]. The behavior of the a and c lattice parameters with changes in cell voltage (lithium concentration) was investigated using *in situ* x-ray diffraction during electrochemical cycling. The results of this study are presented in Appendix B. The diffraction patterns from the chemically delithiated samples were compared with the literature [60] to confirm the compositional analysis (ICP-MS).

The oxygen K-edge and the cobalt $L_{2,3}$-edge for the five samples are displayed in Figures. 4.3. The full spectra ($0 < E < 950$ eV) were deconvolved using the Fourier-log method (Equation 2.22). The deconvolution process removes the effects from plural scattering that distort the shape of the near-edge structure. The spectral intensities in the oxygen K-edge

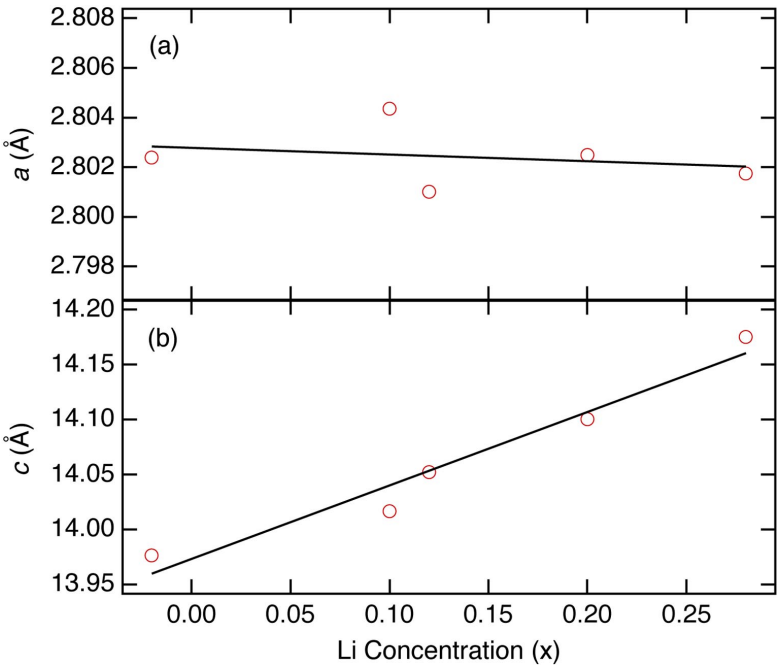

Figure 4.2: The (**a**) a and (**b**) c lattice parameters of $Li_{1-x}CoO_2$ measured using the (110) and (018) diffraction peaks.

were normalized to the main peak at 542 eV. The cobalt $L_{2,3}$-edge includes a pair of white lines from electronic transitions into unoccupied cobalt $3d$ states. The intensities of the cobalt $L_{2,3}$ white lines were normalized to a 50 eV continuum located 50 eV above the onset of the L_3 white line.

The sum of the p densities of states at oxygen atoms was calculated from the eigenvalues and the projection operators given by the *ab initio* total energy and molecular dynamics program VASP (Vienna *ab initio* simulation program) developed at the Institut fur Materialphysik of the University of Wien [61, 62, 63]. The atomic positions were taken from earlier VASP calculations of Ceder et al. and only the O3 [64] structure was considered. As the changes with stoichiometry were very small, it is expected that different structural models would not have significantly different sums over atomic site densities of states. The Gaussian smearing method [65] was used to calculate the density of states from the eigenvalues. A check was made that sufficient k points had been included to achieve convergence. A Wigner-Seitz radius of 1.39Å was chosen for projecting the oxygen states.

The atomic cross sections for the oxygen K-edge were calculated to account for the continuum contribution to the energy-loss spectrum. The full cross section is identified in Equation 2.14 and is a function of E and q. However, the energy-loss spectrum contains

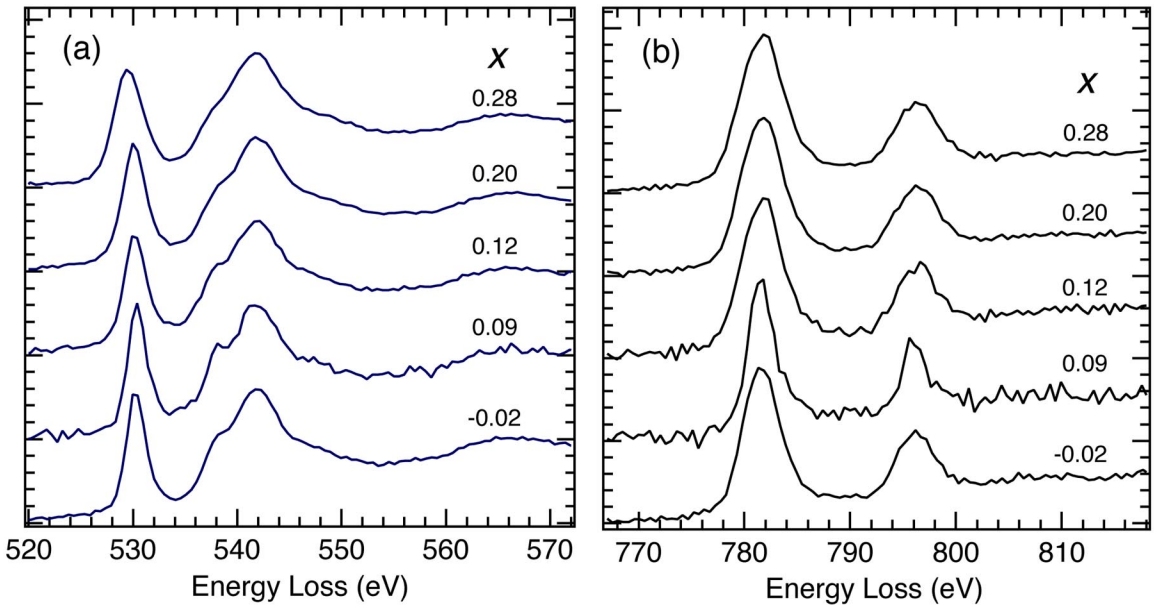

Figure 4.3: Electron energy-loss spectra of the (**a**) oxygen K-edge and (**b**) cobalt $L_{2,3}$-edge from $Li_{1-x}CoO_2$, labeled by x.

contributions from all allowed q values[1] and is only a function of E. Therefore, the differential cross section was integrated over all q, which is equivalent to accepting all allowed scattering angles, ϕ. The cross sections were calculated with hydrogenic [25] and Hartree-Slater [66, 67] wavefunctions, which gave similar results (Fig 4.4). The oxygen K-edge cross sections were calculated for transitions into a continuum of unoccupied states. When the square of the transition probability of the continuum component (as a function of E) is divided out of the energy-loss spectrum, the result is an experimental representation of the p projected density of unoccupied states.

A plot of simulated oxygen partial density of states (PDOS) for $Li_{1-x}CoO_2$ (x = 0.00, 0.20, 0.25) is shown in Figure 4.5. The oxygen PDOS were normalized to the $2p$ band ~ 15 eV above the Fermi energy (E_F) and the PDOS was plotted relative to E_F ($E - E_F$). The region $(E - E_F) \leq 0$ consists of occupied states. The peak located just above E_F at ~ 1.5 eV is the lowest unoccupied state, and corresponds to a σ^* state in the O $2p$–Co $3d$ orbital. Similar to the experimental spectra, the calculations of the oxygen PDOS demonstrate that intensity of the lowest lying unoccupied peak (just above E_F) increases with lithium extraction. The region 10–20 eV above E_F contains a continuum of unoccupied states. The structure of this region of the oxygen K-edge is dominated by intrashell multiple scattering

[1] q values up to 17 $Å^{-1}$ (in units of $2\pi/\lambda$)

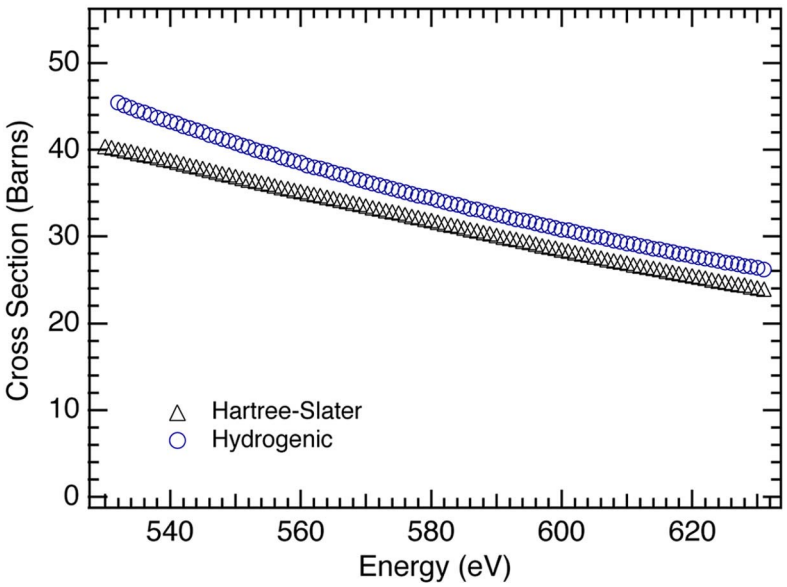

Figure 4.4: Ionization cross sections calculated with hydrogenic and Hartree-Slater wavefunctions using 100 keV electrons and a 100 mrad collection angle.

within the first oxygen neighbors [36].

4.4 Discussion

In $LiCoO_2$ the oxygen $2p$ band is hybridized with the cobalt $3d$ band, forming a strongly covalent bond. A proposed energy diagram of the TM $3d$ - O $2p$ bonding is displayed in Figure 4.6.

Bremsstrahlung isochromat spectroscopy (BIS), XPS, and XAS measurements suggest that the cobalt ion is in a low spin configuration: $S = 0$, $d^6(t_{2g})^6(e_g)^0$ [56, 68]. As lithium is doped into CoO_2, there is a reduction of states in the σ antibonding orbital. The intercalated lithium in the metal-oxide host increases the crystal field splitting between the e_g and t_{2g} orbitals such that it becomes energetically favorable to empty the e_g orbitals. In $LiCoO_2$ some of the O $2p$–Co $3d$ hybridized orbitals are empty [56, 57]. Transitions into these holes are observed in the near edge structure (530 eV) of the energy-loss spectra in Figure 4.3.

The most salient feature seen in Figure 4.3 is the increased broadening of the oxygen K-near-edge pre-peak (at 530 eV) in the delithiated material. The pre-peak growth between $Li_{1.0}CoO_2$ and $Li_{0.72}CoO_2$ is approximately 17%. This growth indicates a significant electron depletion in oxygen $2p$ states. As lithium is removed, there is a corresponding decrease in the charge density surrounding the oxygen ion, making the Co-O bond more covalent. Equivalently, as lithium is added to the material, the unoccupied Co-O antibonding states,

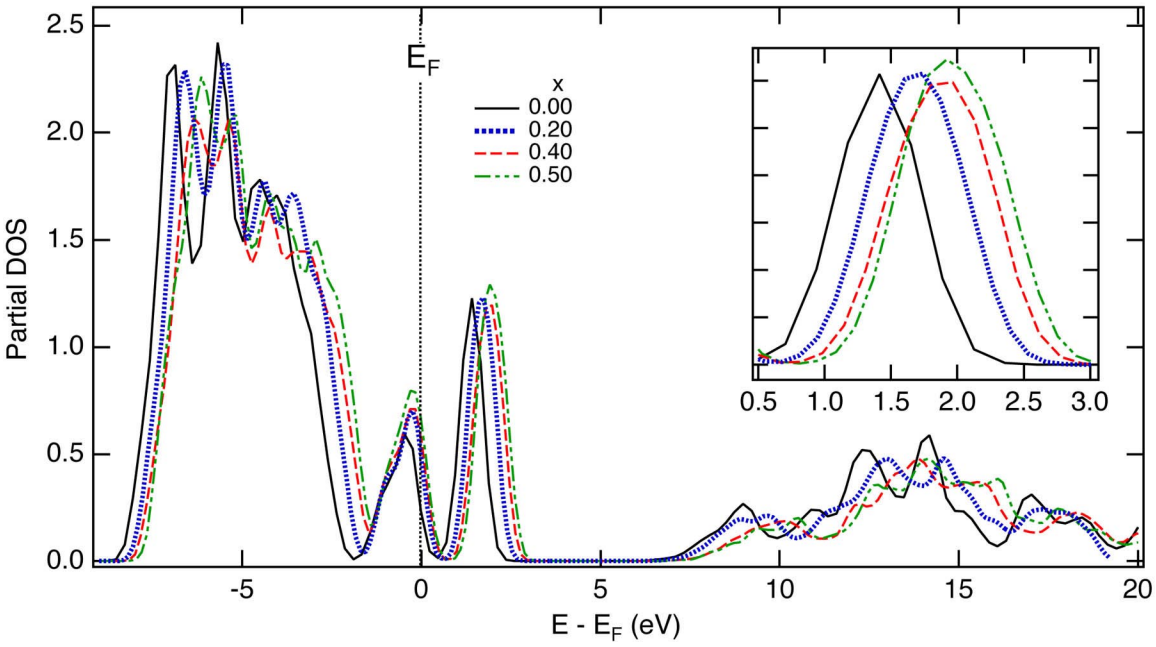

Figure 4.5: Calculated oxygen PDOS for four compositions $Li_{1-x}CoO_2$. The vertical dashed line indicates the position of the Fermi Energy (E_F).

evident in EELS as holes in the oxygen $2p$ states, are responsible for accommodating the incoming lithium $2s$ electron. This behavior is also found in the calculated oxygen PDOS shown in Figure 4.5. The increase in the first unoccupied peak ($E - E_F = 1.5$ eV) with lithium depletion is similar to that seen in the experimental spectra, and is indicative of a covalent evolution in bonding between the oxygen and cobalt ions. A plot of the oxygen PDOS with the energy loss spectrum for a sample of $Li_{1.0}CoO_2$ is displayed in Figure 4.7. In this plot the EELS spectrum was corrected for the cross-sectional intensity of Figure 4.7.

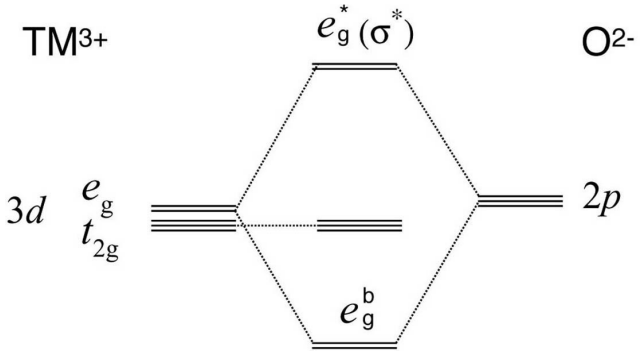

Figure 4.6: Molecular orbital diagram of the TM-O bond in $LiTMO_2$.

The core binding energy ($E_{1s} - E_{2p} \approx 529$ eV) has been subtracted off the energy scale

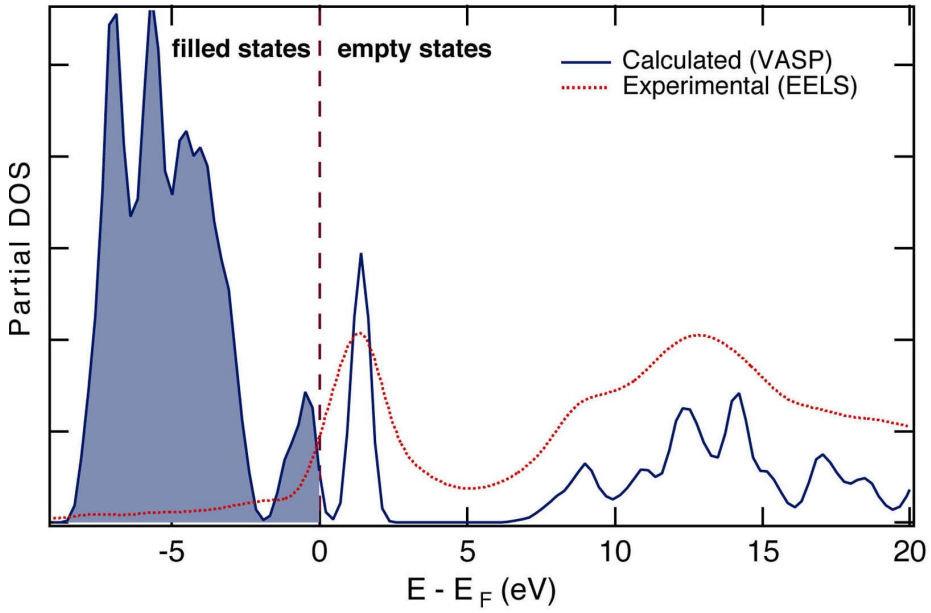

Figure 4.7: Simulated and experimental oxygen PDOS of $Li_{1-x}CoO_2$. The energy-loss spectra have been normalized by the atomic cross section and a core energy of 529 eV was removed.

in the energy-loss spectrum of Figure 4.7. The measured transition energies are dependent upon the relative energy separation between the occupied $1s$ state and the unoccupied $2p$ state. A direct comparison of peak positions in Figures. 4.3 and 4.5 would incorrectly assume that the $1s$ core energies are unaffected by changes in the oxygen $2p$ band. Since core state energies are not provided by VASP, we have chosen instead to quantify the integrated intensities of spectral features, which are unaffected by core shifts.

The experimental and computational results both demonstrate that with lithium depletion there is an increase in the density of available states in the oxygen $2p$ band. Figure 4.8 compares the integrated intensity of the oxygen K pre-peak, corrected for the inelastic form factor (Equation 2.14), and the lowest lying unoccupied state of the calculated oxygen PDOS. The plot reveals an approximately linear dependence of the occupancy of the antibonding state with lithium concentration between $0 \leq x \leq 0.5$. The behavior of the pre-peak in the experimental spectra is in excellent agreement with the calculated density of available states. No scaling of either data set was used in this comparison.

Such a model for charge compensation is also supported a number of computational studies [54, 55, 64, 69]. These investigations found a significant electron rearrangement, but little net electron transfer to the cobalt ions when lithium was inserted into the CoO_2

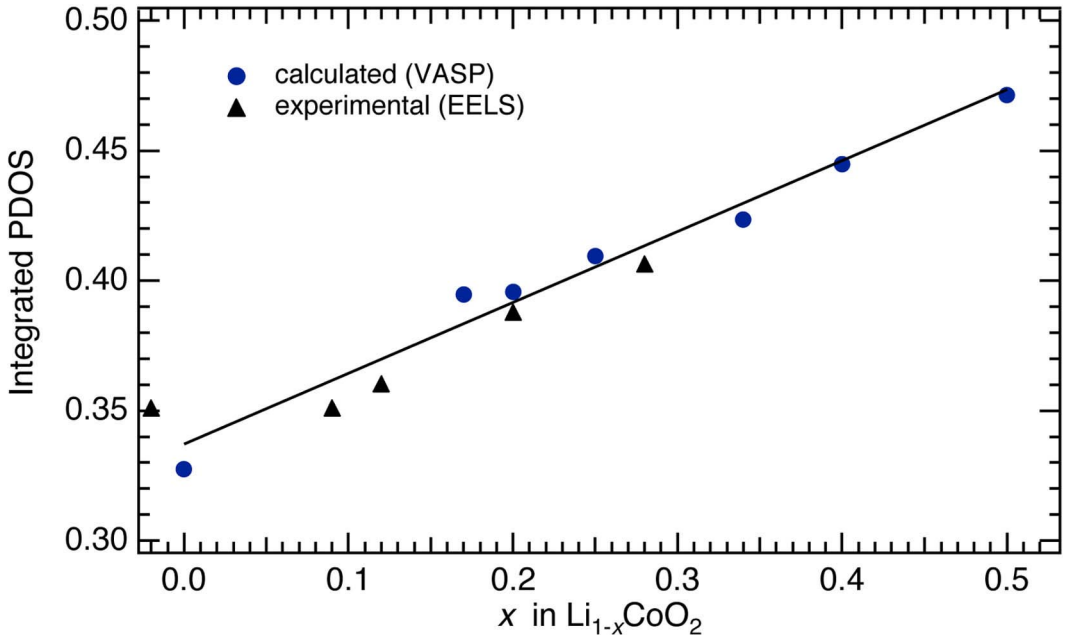

Figure 4.8: Normalized intensity of the antibonding peak in the oxygen PDOS and pre-peak in oxygen K-edge for $Li_{1-x}CoO_2$. The experimental data were normalized by the atomic cross section. The straight line is a linear fit to the calculated points (slope = 0.27).

host. Significant changes in the electronic charge density were found near the oxygen ions, suggesting that the lithium $2s$ electron is almost entirely accommodated by the O $2p$ band. As lithium is intercalated into the covalent CoO_2 host, the Co–O bond progresses towards a more ionic character.

Unlike the oxygen K-edge, the cobalt L-edge undergoes little change with lithium depletion. Figure 4.9 displays a plot of the normalized cobalt $L_{2,3}$ white line intensities for two different regions within four samples. There is no discernible trend in the total white line intensity as a function of lithium concentration. Likewise, the lithium concentration has no observable effect on the L_2/L_3 ratio. There is, however, variation in the integrated intensity of the $L_{2,3}$ white lines between different regions within a sample. Fluctuations of this nature are unexpected within a chemically and structurally homogenous material. Although this could reflect an anisotropic charge distribution near the cobalt ions, our procedures for the deconvolution of thickness effects and background correction could provide some variation in our reported white line intensity.

A recent electron energy-loss spectrometry study on the anode material of lithium-ion batteries, graphite intercalated with lithium, demonstrated that lithium atoms have neutral

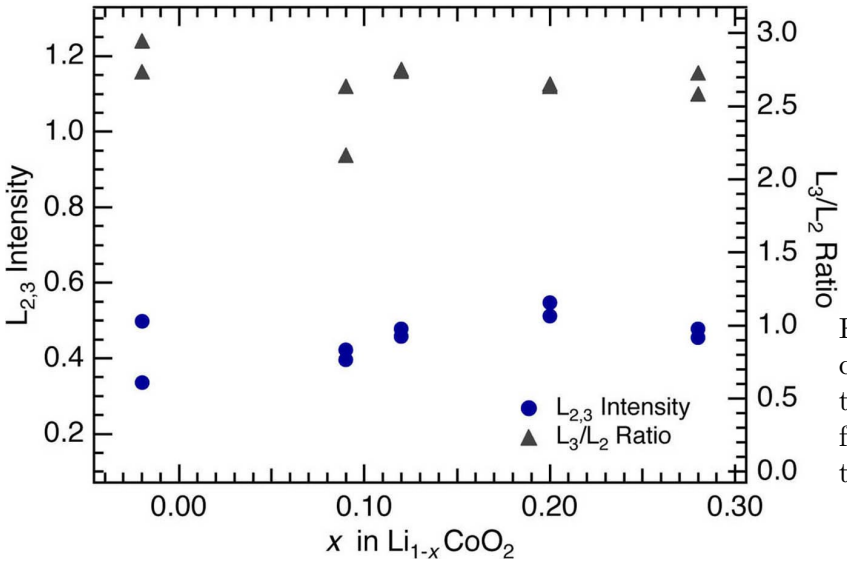

Figure 4.9: Normalized cobalt $L_{2,3}$ white line intensity and L_3/L_2 ratio from two different crystallites of $Li_{1-x}CoO_2$.

valence in the anode, and are not Li^+ ions as is implied by the name "lithium-ion battery" [37]. The present experimental work shows, as expected, that the lithium in the cathode $LiCoO_2$ is ionic Li^+. In conjunction with the previous theoretical work [54, 55], however, we see that the chemistry of the cathode material originates primarily with electron transfers from lithium to the oxygen ions. Perhaps the name "lithium-lithium oxide" battery better conveys the chemistry of the full cell.

4.5 Conclusion

The partial density of states of oxygen atoms was measured by EELS, and calculated with the VASP code for delithiated $Li_{1-x}CoO_2$. Both revealed a filling of oxygen $2p$ holes by the incoming $2s$ electron upon lithium intercalation into $Li_{1-x}CoO_2$. The large density of unoccupied states in the band of hybridized O $2p$–Co $3d$ states is indicative of the strong covalent nature of the bonding in $LiCoO_2$. Although the electron density around the cobalt ions may be strongly anisotropic, the net charge surrounding the cobalt ions is largely unaffected by lithium concentration. The oxygen ions are primarily responsible for accommodating the incoming charge during lithium intercalation.

Chapter 5 Electronic Structure and Charge Compensation in $LiNi_{0.8}Co_{0.2}O_2$

5.1 Introduction

The compound $LiNi_{0.8}Co_{0.2}O_2$ is a promising cathode for lithium batteries. It has the same layered structure as $LiCoO_2$ but with a substitution of nickel atoms at cobalt sites. In $LiNi_{0.8}Co_{0.2}O_2$ the nickel and cobalt ions are both octahedrally coordinated by oxygen ions and occupy the same crystallographic sites. This material is an improvement over $LiNiO_2$ because it combines a high cycling capacity with safe operating conditions even in the delithiated charge state. $LiNi_{0.8}Co_{0.2}O_2$ remains as a single phase during deep lithium deintercalation, allowing reversible cycling from $Li_{1.0}$ to $Li_{0.4}$ [70]. Also, the $LiNi_{0.8}Co_{0.2}O_2$ cathode is less susceptible to cationic disorder (TM ions occupying lithium sites) than the $LiNiO_2$ system. $LiNi_{0.8}Co_{0.2}O_2$ has a slightly lower voltage vs. lithium when compared to $LiCoO_2$ and consequently, electrochemical cells are less prone to electrolyte decomposition. Finally, the reduction of cobalt also allows for a cheaper, more environmentally friendly cathode.

During electrochemical discharge, lithium ions and their associated electrons are intercalated into the TMO_2 host. There have recently been a number of investigations into how the intercalated lithium affects the electronic structure of the host [10, 48, 57, 70, 71, 72, 73, 74, 75, 76, 77, 78, 79, 80, 81]. The results of these studies have led to recent debate over the amount of charge transferred to the oxygen and TM ions. Analyses of the TM core edges using x-ray absorption spectroscopy (XAS), magnetic susceptibility, electronic conductivity, and thermoelectric measurements, have found that upon lithium deintercalation the TM ion is oxidized to the tetravalent state [10, 70, 71, 77, 78]. Studies of the $LiNi_{1-y}Co_yO_2$ system suggest that during discharge, the nickel ions are immediately oxidized to the tetravalent state while the cobalt oxidation occurs only in the heavily delithiated state [10, 70, 71]. In $LiNi_{0.8}Co_{0.2}O_2$ the preferential oxidation of nickel over cobalt is attributed to the position of the Fermi level, which lies within the energy gap between the Ni^{2+}/Ni^{3+} and Ni^{3+}/Ni^{4+} redox couples. It is argued that the Fermi level drops into the Ni^{3+}/Ni^{4+} band during

the early stages of delithiation and the nickel is oxidized. The t_{2g} band of cobalt appears at a lower energy, requiring the removal of up to 80 percent of the lithium atoms before the Fermi level is lowered sufficiently for cobalt oxidation [70]. Although there is general agreement that the cobalt ion participates little in the redox processes that occur during cycling, the behavior of the nickel ion is still not well understood. The notion of a trivalent nickel ion in the fully lithiated material has been disputed by recent results of Montoro et al., which suggest that in $LiNi_{0.5}Co_{0.5}O_2$ the nickel ions are divalent and are partially oxidized to a trivalent state during delithiation [48].

Absorption studies using hard X rays have been used to investigate the electronic structure around the TM ions. However, these studies are unable to measure electronic transitions with low absorption energies like those contributing to the oxygen K-edge. Therefore, these measurements are relatively insensitive to the atomic states of oxygen. More indirect experiments, such as magnetic measurements, can be difficult to interpret, and may be misleading because changes in the spin density, or the number of unpaired electrons about an ion, are not necessarily correlated with changes in the charge density.

Soft x-ray absorption and transmission EELS are well suited for studying the electronic structure near the oxygen and TM ions at different states of lithiation. Recent studies of the oxygen K-edge and nickel and cobalt $L_{2,3}$-edges have demonstrated that the oxygen ion is responsible for accommodating much of the lithium $2s$ electron during intercalation [57, 79, 80, 81]. These studies suggest a nearly constant net charge density in the vicinity the transition metal ion, with significant changes in occupancy of the oxygen $2p$ band. The details of the redox energies of the individual transition metal ions appear to be subordinate to changes occurring in the oxygen valence.

First-principles calculations by Wolverton and Zunger have found that in $LiCoO_2$ the net charge density about the cobalt ion is unaffected by lithium concentration. This behavior is attributed to a rehybridization of the Co-O bond, which produces invariant energy levels and electronic stability over a wide range of lithium concentration [69]. Other first-principles calculations of $LiCoO_2$ have suggested that much of the lithium $2s$ electron is donated to the oxygen, allowing the cobalt valence to remain predominately in the trivalent state [54, 82, 64]. These *ab-initio* studies add insight into the experimental results for the ordered $LiCoO_2$ and $LiNiO_2$ systems. However, calculations on a disordered distribution of nickel and cobalt atoms are not practical owing to the complexity of the unit cell of $Li(Ni,Co)O_2$. Here we

report results from an experimental investigation using transmission EELS to elucidate changes in the electronic structure of $Li_{1-x}Ni_{0.8}Co_{0.2}O_2$ with the removal of lithium.

5.2 Experimental

Samples were prepared by chemically charging (delithiating) of $LiNi_{0.8}Co_{0.2}O_2$ powders provided by Enax Inc. A previous investigation of the core edges of $Li_{1-x}CoO_2$ revealed similar results for chemically and electrochemically delithiated samples. However, chemically prepared samples are preferred because spectral artifacts from binders and conductive diluents can be eliminated. The methods used for chemical delithiation are covered in Appendix A. The elemental analysis of the bulk material was performed using ICP-MS. Two methods were employed to determine the final lithium concentrations in $Li_{1-x}Ni_{0.8}Co_{0.2}O_2$. First, the amount of lithium removed from the stoichiometric material, x, was measured in the $K_2S_2O_8$ solution using ICP-MS. Secondly, the amount of lithium remaining in the delithiated oxides $(1-x)$ was measured by ICP-MS. A structural analysis was performed using XRD. Powder XRD patterns were acquired with an Inel CPS-120 diffractometer using cobalt $K\alpha$ radiation ($\lambda = 1.790$ Å).

Transmission electron microscopy and EELS measurements require an electron-transparent sample. To ensure that some of the particles in the $Li_{1-x}Ni_{0.8}Co_{0.2}O_2$ were suitably thin, the powders were crushed with a mortar and pestle in Fluorinert^{TM} and the fine particles were dispersed onto a holey carbon grid. The EELS spectra were acquired using a Gatan 666 parallel-detection spectrometer in a Philips EM 420 transmission electron microscope operated at 100 kV. The spectra were acquired with diffraction coupling (image mode), at a dispersion of 0.5 eV per channel. A large collection angle of approximately 100 mrad was used to ensure spectral contributions from the entire Bethe ridge. The energy resolution was approximately 1.5 eV.

5.3 Results

The XRD results from delithiated $Li_{1-x}Ni_{0.8}Co_{0.2}O_2$ (Figure 5.1) reveal a shift of the (003) peak to lower angles and a simultaneous shift of the (104) and (110) peaks to higher angles. The shift of the (003) peak with lithium extraction is similar to that seen in $LiCoO_2$ in

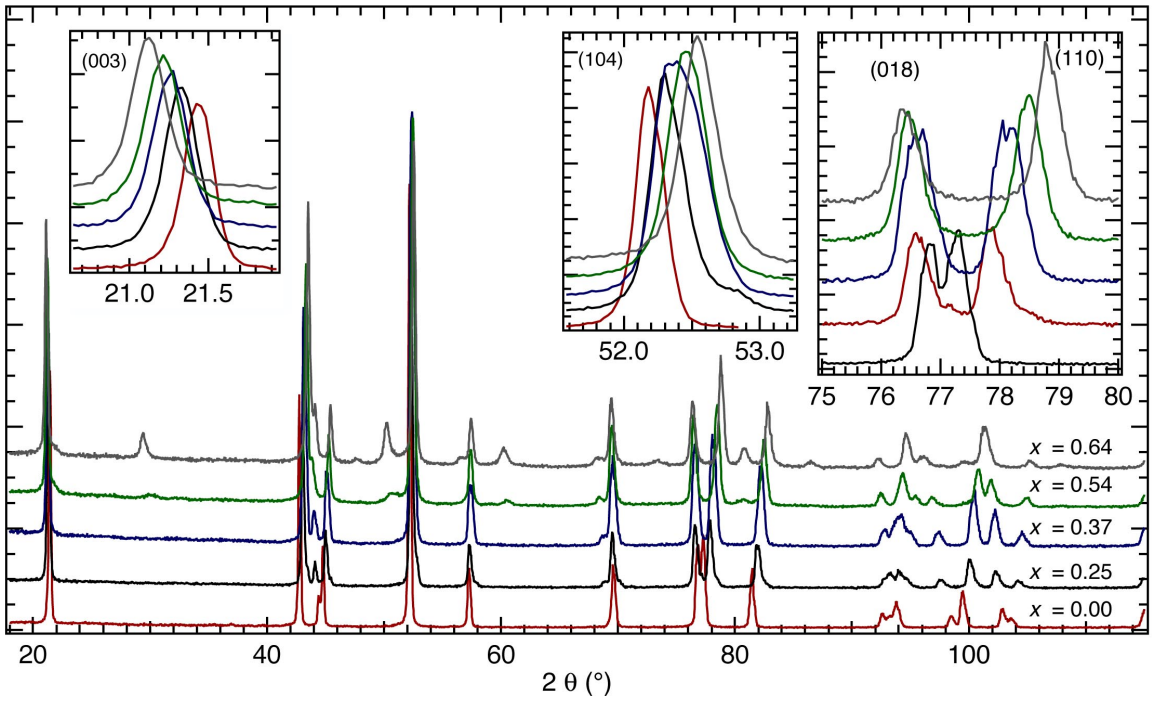

Figure 5.1: Powder x-ray diffraction from $Li_{1-x}Ni_{0.8}Co_{0.2}O_2$, labeled by x.

Chapter 4 and Appendix B. The removal of lithium reduces the screening between oxygen layers and the lattice responds by increasing the distance between basal planes. The shifts in the (104) and (110) peaks are larger than those observed in $LiCoO_2$. The lattice parameters of the delithiated samples were determined from the (018) and (110) diffraction peaks (Figure 5.2). These results are consistent with those of Ronci et al. for delithiated $LiNi_{0.8}Co_{0.2}O_2$ [83]. Therefore, the diffraction analysis corroborates the elemental analysis performed using ICP-MS and also ensures that the appropriate phases are present in the material.

The various core edges for the five samples of $Li_{1-x}Ni_{0.8}Co_{0.2}O_2$ are displayed in Figures 5.3–5.5. Detector artifacts were removed by dividing out an instrument response. The full energy-loss spectra ($0 \leq E \leq 950$ eV) were then deconvolved using the Fourier-log method (Equation 2.22). Finally, a background was fit to the pre-edge region using a power-law decay function, and subtracted from beneath the core-edges.

The lowest-lying core edges for the $Li_{1-x}Ni_{0.8}Co_{0.2}O_2$ system are shown in Figure 5.3a. The lithium K-edge onset occurs at $\sim$ 58 eV, which is shifted by approximately 3 eV with respect to lithium metal. The shift to higher energies in lithium metal oxides is the result of the ionic bonding between the lithium and the host structure. The loss of

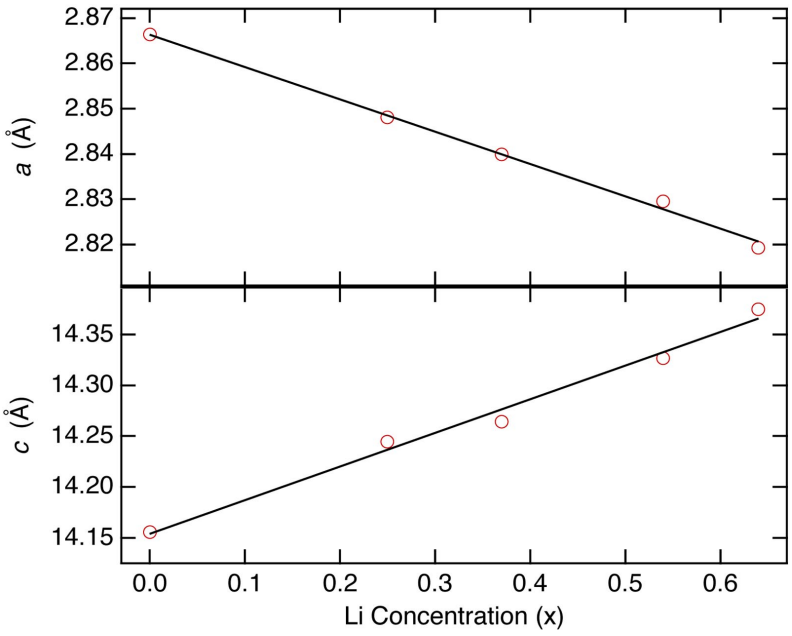

Figure 5.2: (**a**) a and (**b**) c lattice constants for $Li_{1-x}Ni_{0.8}Co_{0.2}O_2$.

the lithium $2s$ electron reduces the screening of the nuclear charge, thereby increasing the binding energy of the core electron and increasing the ionization energy. This region of the energy-loss spectrum also contains contributions from the cobalt and nickel $M_{2,3}$-edges at approximately 60 and 68 eV, respectively. The cobalt and nickel $M_{2,3}$-edges appear to be unaffected by the lithium concentration. The nickel and lithium edges are adequately separated in energy, and although the cobalt and lithium edges overlap, the contribution from cobalt is small enough so that changes at the lithium K-edge can be resolved clearly. As expected, this figure shows a decrease in the intensity of the lithium K-edge as lithium is extracted from the material.

X-ray diffraction and ICP-MS results from the bulk powders provide averaged information on the chemical composition of the delithiated samples. However, energy-loss spectra are acquired from areas of the sample less than 1 μm^2, so the composition of the analyzed region may be different from the bulk. The spectra of Figure 5.3a were used to calibrate the lithium K-edge intensity with the lithium concentration. The integrated intensity of the lithium K-edge was measured using a 5 eV window and normalized to the invariant nickel $M_{2,3}$-edge. Figure 5.3b demonstrates the linear relationship found between the lithium K-edge intensity and the bulk lithium concentration as measured by ICP-MS. Using this calibration, the quantified lithium K-edge intensity of a delithiated particle was then used to determine the lithium concentration of the region under analysis, thus avoiding errors

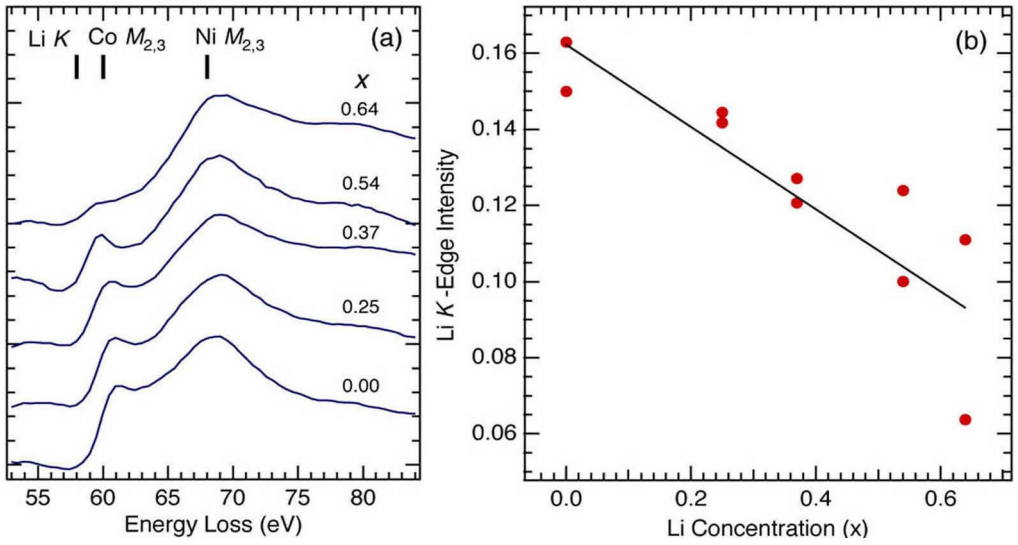

Figure 5.3: (**a**) Energy-loss spectra from from $Li_{1-x}Ni_{0.8}Co_{0.2}O_2$ displaying the lithium K-edges at different lithium concentrations. The spectra are labeled with the ICP-MS values for x. (**b**) Normalized lithium K-edge intensity vs. measured lithium concentration (ICP-MS).

due to compositional heterogeneities in the powders. Figure 5.3b exhibits a consistent edge intensity, $\pm 4\%$, in the fully lithiated powders. The largest variations in the edge intensities, $\pm 30\%$, were found in the most delithiated sample. A linear fit to these data does not extrapolate to zero at $x = 1.0$, owing to some interference from the cobalt $M_{2,3}$-edge.

The cobalt and nickel $L_{2,3}$-edges for the delithiated samples are shown in Figures 5.4a and b, respectively. The edge onset is characterized by two sharp peaks, which are the result of transitions from the $2p_{1/2}$ and $2p_{3/2}$ energy levels into unoccupied $3d$ states. In measuring the integrated white lines, the free-electron-like contributions to the core edges were approximated as step functions, and subtracted from the total intensity. The cobalt and nickel white lines were normalized to integration windows of 40 and 50 eV, respectively, just above the L_2-edge. To maximize the energy resolution over the fixed detector array, the spectra were acquired in two intervals and matched in energy scale subsequent to the acquisition. The cobalt $L_{2,3}$ white lines were used for energy calibration, so the TM and oxygen edge onset energies are not reliable.

The oxygen K-edge for five samples of $Li_{1-x}Ni_{0.8}Co_{0.2}O_2$ are displayed in Figure 5.5. The edge onset is characterized by a large pre-peak at 530 eV corresponding to a σ^* transition. The unoccupied σ antibonding state is the consequence of a hybridization of the oxygen $2p$ band with the highly localized TM $3d$ states. The spectral intensities were nor-

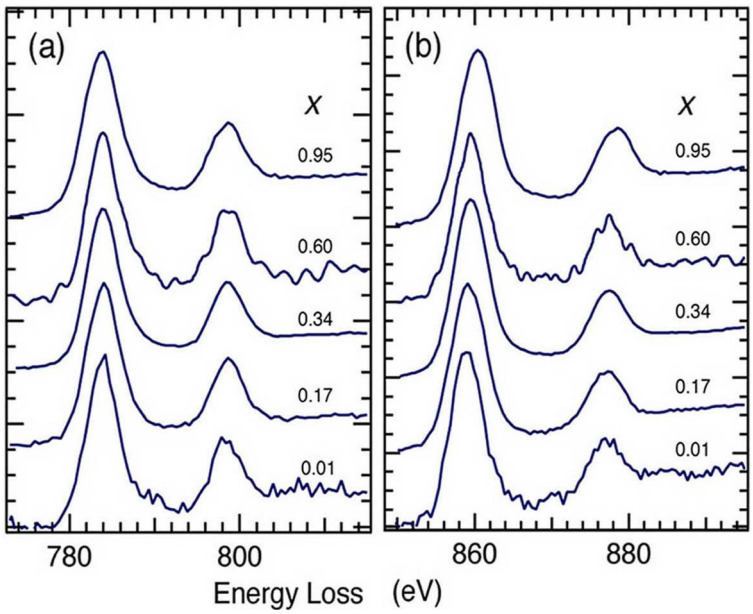

Figure 5.4: (**a**) Cobalt and (**b**) nickel $L_{2,3}$ white lines from $Li_{1-x}Ni_{0.8}Co_{0.2}O_2$, labeled by x.

malized to a 10 eV window 40 eV above the edge onset, and the deintercalation value, x, was measured using the intensity of the lithium K-edge.

5.4 Discussion

The cobalt and nickel $L_{2,3}$ white lines shown in Figure 5.4 are essentially unchanged with variations in lithium concentration. The spectral intensity of the white lines is governed by $2p \rightarrow 3d$ transitions. The integrated white line intensity is a measure of the holes in the localized $3d$ states near the transition metal. The cobalt and nickel white line intensities are displayed in Figures 5.6–5.7, respectively. These plots demonstrate a nearly-constant white line intensity over a wide range of lithium concentration. A linear fit to the cobalt $L_{2,3}$ intensity is essentially constant over the delithiated series while the nickel white line intensity increased by approximately 5%. The invariant cobalt white line intensity indicates a constant $3d$ band occupancy during delithiation. The increase in the nickel white line intensity implies a depletion of the $3d$ band, which suggests that the nickel ions may compensate for some of the lithium charge. The relationship between the white line intensity and the $3d$ occupancy in TM oxides (Chapter 3) was used to a calibrate the $3d$ states in the delithiated material. The nickel ions in the fully lithiated material were found to be predominately divalent. The 5% increase in the nickel white line intensity corresponds to a change in the nickel valence of 0.20 electrons over the delithiated series. This is

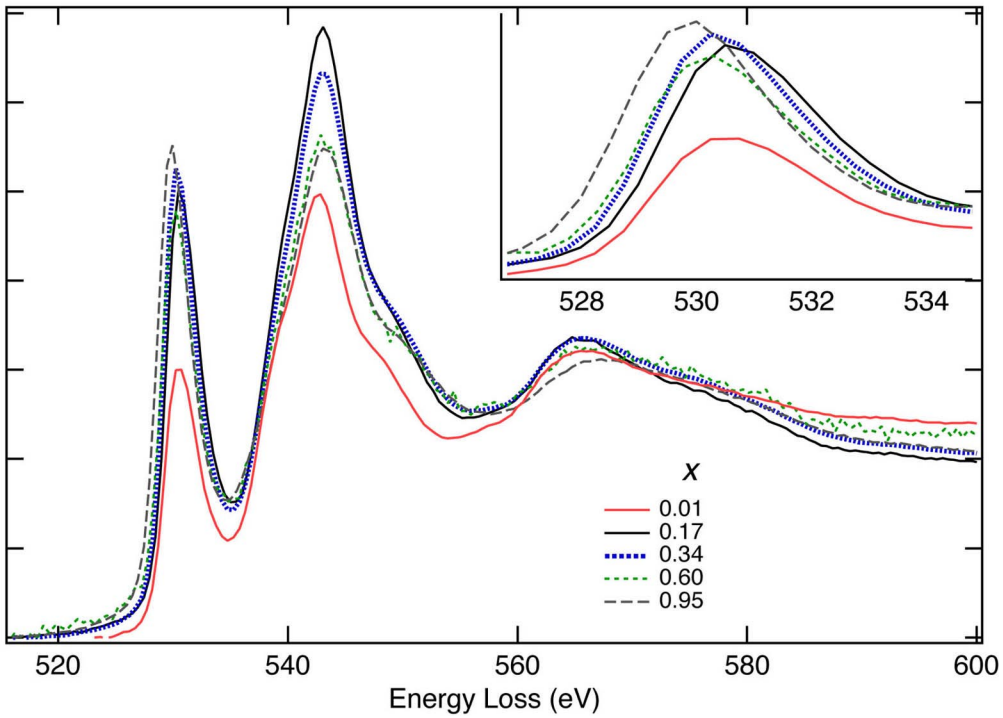

Figure 5.5: Oxygen K-edge from $Li_{1-x}Ni_{0.8}Co_{0.2}O_2$, labeled by x. The inset displays the expanded view of the pre-peak.

based on the the assumption that the oxidation of nickel occurs linearly from $0 \leq x \leq 1$. However, Montoro et al. have suggested that the oxidation of nickel reaches a plateau at $x \approx 0.5$, which is in agreement with the measured white line intensities shown in Figure 5.7. Assuming such a saturation, a linear fit from $0 \leq x \leq 0.5$ suggests that the nickel ions may compensate up to 0.50 electrons during lithiation.

The total intensity difference over the delithiated series (5% in nickel) is near the detectable limit, given the variations between points of similar lithium concentration. Therefore, the total charge compensation measured is not absolute, but should be regarded as an upper bound. These charge compensation measurements apply to changes only occurring in the $3d$ band because the transition probabilities are governed approximately by the dipole selection rule ($\Delta l \leq \pm 1$). Intraband transitions are negligible, so the TM $L_{2,3}$-edge is insensitive to the occupancy of the TM $4p$ states. The cobalt and nickel L_3/L_2 ratios are displayed in Figures 5.6 and 5.7, respectively. Although the absence of a perceptible trend in the nickel white line ratios makes them difficult to interpret, the constant cobalt white line ratios lends credence to the notion of an invariant cobalt valence with delithiation.

The stability of the white lines suggests that the TM ions are not responsible for ac-

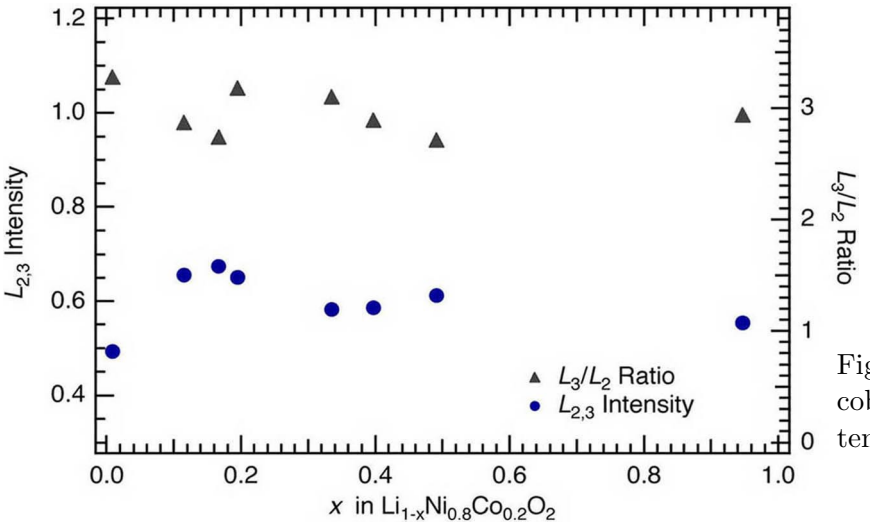

Figure 5.6: Normalized cobalt $L_{2,3}$ white line intensity and L_3/L_2 ratio.

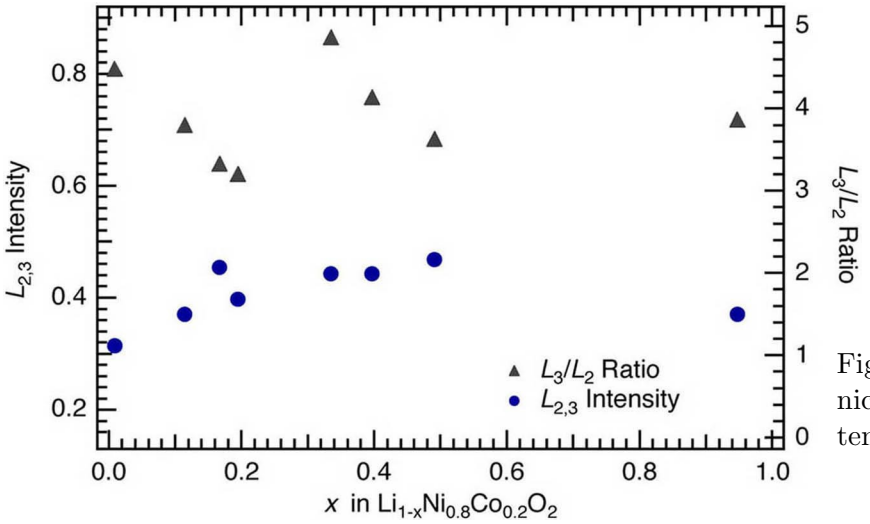

Figure 5.7: Normalized nickel $L_{2,3}$ white line intensity and L_3/L_2 ratio.

cepting all of the lithium charge, and therefore implies that the oxygen ions may play a significant role in charge compensation. As previously mentioned in Chapter 3, in $LiTMO_2$ the oxygen $2p$ band is hybridized with localized TM $3d$ states. The near-edge structure (530 eV) of the EELS spectra shown in Figure 5.5 is the result of transitions into oxygen $2p$ holes (unoccupied σ^* molecular orbital) formed by the hybridization.

The oxygen K-edges for the delithiated series (Figure 5.5) demonstrate an increase in the integrated intensity of the pre-peak at 530 eV. These changes indicate an increase in unoccupied $2p$ states or, equivalently, a decrease in charge density about the oxygen with delithiation. The behavior of the oxygen K-edge corroborates the trends in the TM white lines and verifies the claim that the oxygen ion compensates for much of the lithium $2s$ electron. This method of charge compensation suggests the oxidation of oxygen, which

is contrary to conventional chemistry. A resolution to this paradox, originally proposed by Wolverton and Zunger for $LiCoO_2$, is that the delithiation drives the $Co^{3+} \rightarrow Co^{4+}$ redox process but simultaneous changes in the Co-O hybridization leads to a decrease in the charge density near the oxygen ions [69]. These calculations revealed a constant charge density about the cobalt ion as the lithium content is reduced [69].

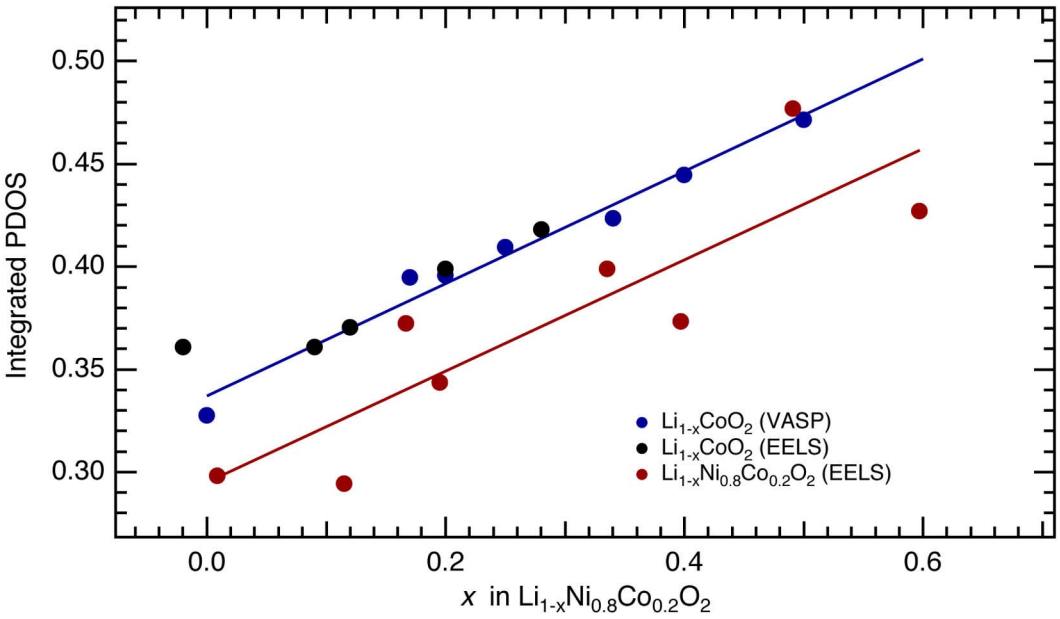

Figure 5.8: Normalized intensity of antibonding peak in the calculated oxygen PDOS (VASP) for $Li_{1-x}CoO_2$ and measured pre-peak of the oxygen K-edge (EELS) for $Li_{1-x}CoO_2$ and $Li_{1-x}Ni_{0.8}Co_{0.2}O_2$. The experimental data were normalized by the atomic cross section.

The relationship between the number of oxygen $2p$ holes and the state of charge is quantified in Figure 5.8, which compares the integrated intensity of the oxygen K-near-edge structure in $LiNi_{0.8}Co_{0.2}O_2$ with lithium concentration. A linear fit was made to the data between $0 \leq x \leq 0.6$ to compare with previous results for $LiCoO_2$. This fit reveals a 60% increase in the intensity of the oxygen K near-edge structure. Previous EELS data for $LiCoO_2$, and the partial density of states (PDOS) as calculated for $LiCoO_2$ using the VASP code are also displayed in Figure 5.8 [80]. The energy-loss data used in this plot were corrected for their inelastic form factor, which were calculated with Hartree-Slater wavefunctions (Chapter 4). The plot indicates that the intensity of the unoccupied antibonding state is correlated linearly to the lithium concentration. The slopes for the cobalt and (Ni,Co) systems are approximately 0.26 and 0.28, respectively. The difference in the initial intensity is likely due to the different number of oxygen $2p$ holes present in the

stoichiometric material of the two systems. The Li(Ni,Co)O_2 material has fewer oxygen $2p$ holes than $LiCoO_2$.

Van der Ven et al. recently found that lithium intercalation into a CoO_2 host results in a polarization of the e_g^b bond between oxygen and cobalt, with the bulk of the electron density residing near the oxygen ion. It was also shown that the net charge about the oxygen atom increases linearly with lithium intercalation. Their relationship between the oxygen valence and lithium concentration exhibits a slope of 0.28–0.30 [64] which is in agreement with our measured slopes for this system. This group has also found that the net change near the cobalt ion is rather constant with lithium concentration [54, 64, 82]. Their predicted behavior of the TM valence with lithium concentration is in agreement with our measured white line intensities.

5.5 Conclusion

The near-edge structure of the oxygen K-edge exhibits large changes over a range of lithium content in Li(Ni,Co)O_2. Smaller changes are observed in the nickel $L_{2,3}$ white lines, while no perceptible change was observed for the cobalt $L_{2,3}$ white lines. The nickel ions were found to be divalent in the fully lithiated state. The upper bound on the total charge transferred from lithium to the nickel ions was determined to be 1/2 of an electron, while no charge transfer was observed to the cobalt ions. These trends suggest that the oxygen compensates for much of the depleted electronic charge during deintercalation of Li(Ni,Co)O_2. This mechanism of charge compensation allows the net cobalt valence to remain constant and the nickel valence to change slowly over a wide range of lithium concentration. The modest changes occurring in the electronic structure of the transition metals may be partially responsible for the structural stability of the TMO_2 host during cycling.

Chapter 6 High Lithium Capacity and High Rate Capabilities in Nanostructured Silicon

6.1 Introduction

There is currently considerable interest in the development of binary lithium alloys for their use as anodes in lithium secondary electrochemical cells. From the criterion of lithium density, the ultimate anode would be lithium metal itself. Unfortunately, issues of safety have confined lithium anodes to small rechargeable cells. A framework material seems necessary for preserving the anode shape, and metallic alloys can provide this function. Most lithium alloys have average operating voltages below 500 mV versus lithium, and the Li-Si system has the potential for one of the highest gravimetric capacities. Electrochemical alloying of lithium with silicon has shown a number of stable crystalline phases [84, 85, 86, 87, 88]:

$$\mathrm{Si} + x\mathrm{Li} + x\mathrm{e} \rightarrow \mathrm{Li}_x\mathrm{Si} \qquad x = \begin{cases} 1.71 \\ 2.33 \\ 3.25 \\ 4.40 \end{cases}$$

where the four values of x correspond to the compositions of stable compounds. For a range of x from 0 to 4.4 the theoretical specific capacity of pure silicon is 4200 mAh/g, far greater than the theoretical capacity of 372 mAh/g for graphitic carbons that are presently the standard anode material in lithium secondary cells. Furthermore, lithium alloys do not suffer from the solvent cointercalation that can occur in graphitic carbons, and may degrade the storage capacity [89, 90, 91, 92, 93]. The advantages of silicon anodes are well known, but it is also well known that a 300% volume dilatation is associated with alloying 4.4 lithium atoms per silicon atom. This generates enormous mechanical stresses within the brittle material, which is pulverized during the first few charge/discharge cycles [92, 93, 94, 95, 96]. Ultimately, the capacity is considerably reduced due to the loss of electrical integrity between the particles and the current collector. Li et al. have recently demonstrated that bulk silicon loses approximately 90% of its initial capacity after 5 cycles

at ambient temperature [97].

The properties of nanostructured materials have received intense interest over the last decade. These materials may offer improved performance as anodes and cathodes. One potential advantage of nanostructured materials for electrodes, likely originating with their high surface area, is fast kinetics of lithium transport. The rate capabilities of the typical lithium cell are limited by the solid state diffusion of lithium in the host electrodes. Nanostructured electrodes of C [98], Sn [99, 100], $LiMn_2O_4$ [101], and V_2O_5 [102] have found very high rate capabilities with respect to their thin film counterparts. In addition, Sn-based anodes are one example of electrodes which exhibit improved cycle life with nanoscale particles [103, 104]. When dimensions in a material are tens of nanometers, the conventional mechanisms for deformation and fracture are expected to be altered. The presence of a high concentration of grain boundaries that act as diffusion pathways may also contribute to the kinetics of lithium transport. Finally, it is possible that the grain boundaries may also act as storage regions for lithium [103], which would suggest a theoretical capacity in excess of 4200 mAh/g.

In a recent report, silicon nanoparticles (80 nm) were shown to exhibit reversible capacities of up to 1700 mAh/g on the 10^{th} cycle [97]. This is a large improvement over bulk silicon, which loses all capacity after a few cycles (fifth cycle capacity of less than 400 mAh/g [97]). However, the success of these electrodes depends upon the addition of 40% carbon black to act as conductive diluent and provide a matrix for the embedded silicon nanoparticles. This, combined with the necessary 20% binder, degrades the volumetric capacities of these materials considerably. Capacities of 1700 mAh/g have also been reported for silicon nanowires [105]. Similar investigations into nano-sized intermetallic silicon alloys have shown some reversibility with reduced additives, but with lower gravimetric capacity (1100 mAh/g on the second cycle [106]). Other attempts to suppress particle decrepitation include the replacement of the large metallic host crystals with a nanophase host material such as Sn/SnSb [92, 94]. In addition to nanoparticles, thin films (1.2 μm) of silicon have been prepared by chemical vapor deposition in an attempt to mitigate the capacity loss in the silicon system. Although this study has demonstrated capacities up to 1000 mAh/g, the films appear to be plagued by large alloying strains, leading to the mechanical disintegration of the electrode after 20 cycles [96].

In the present work we utilized direct depositions of nanomaterials onto a metallic

current collector. The electrodes were intentionally made very thin, without binders or conductive diluents, so that the intrinsic properties of nanostructured materials could be measured. We report a promising capacity for charge/discharge cycling of two types of nanostructured silicon anodes, and we suggest that the extended cycle life of these electrodes originates with the unique micromechanics of nanostructured materials.

6.2 Experimental

6.2.1 Methods and Measurements

Electrochemical tests were performed using a metallic lithium anode in a stainless steel 2016 coin cell. Between 45 and 210 μg of the silicon electrode was used in the test cells. The mass of silicon was determined using TEM and a Metler micro-balance sensitive to 1 μg. A 0.50 mm thick fiberglass separator was used to isolate the silicon cathode from the lithium anode. A mixture of ethylene carbonate and dimethyl carbonate (EC DMC) with $LiPF_6$ (Mitsubishi Chemical Co.) was used as an electrolyte. All of the test cells were assembled in an argon atmosphere and cycled using an Arbin Instruments BT2000 battery cycler.

X-ray diffraction was performed with an INEL CPS-120 diffractometer using Co $K\alpha$ radiation. The samples for XRD were prepared by a deposition directly onto a glass slide. Scanning electron microscopy (SEM) was performed using a Hitachi S-4100 at 30 kV. SEM samples of cycled electrodes were rinsed in acetone to remove any residual electrolyte from the surface. The uncycled electrodes were studied as-deposited. Transmission electron microscopy was performed in a Philips EM 420 at 100 kV and high resolution electron microscopy (HREM) in a Philips EM 430 at 200 and 300 kV. The TEM samples of the as-deposited materials were prepared by depositing directly onto a holey carbon grid, while the samples from the cycled electrode were prepared by brushing off particles in acetone and floating the detached particles onto a holey carbon grid. All of the lithiated samples (SEM and TEM) were prepared and transported in an argon atmosphere with less than 30 s of air exposure. Electron energy-loss spectroscopy was performed with a Gatan 666 parallel-detection spectrometer on a Philips EM 420 transmission electron microscope operated at 100 kV. The spectra were acquired at a dispersion of 0.2 eV/channel for the lithiated samples and 0.5 eV/channel for the as-deposited samples, with energy resolutions of 1.2 eV and 1.5 eV, respectively. The full energy-loss spectra were deconvolved using the Fourier-log

method (Equation 2.22).

6.2.2 Physical Vapor Deposition and Ballistic Consolidation

Nanostructured silicon electrodes were prepared by two different processes. In one process, nanostructured films of silicon were prepared by evaporation and physical vapor deposition. A charge of elemental silicon was evaporated under a vacuum of 6×10^{-6} torr in a tungsten wire heating basket. A nickel/copper substrate was placed directly below the tungsten basket, and the evaporated silicon atoms were deposited onto the substrates in a continuous thin film of approximately 100 nm in thickness.

The nanocrystalline silicon clusters were prepared by inert gas condensation and ballistic consolidation [107]. Figure 6.1 displays a schematic of the deposition chamber. A "forming

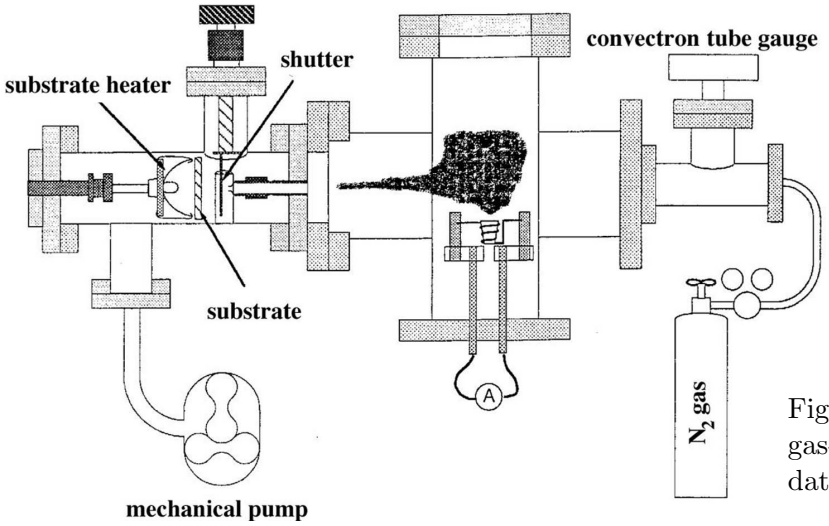

Figure 6.1: Schematic of the gas-phase ballistic consolidation chamber.

gas" of 90% N_2 and 10% H_2 was streamed along the axis of the chamber with a pressure differential of 2 torr. An elemental silicon charge was heated in a tungsten wire basket and evaporated into the gaseous atmosphere. The rate of evaporation was up to 10^{-3} g/cm^2/s (approximately 1800 °C). In the gas, the silicon atoms are cooled rapidly, and nanocrystals are nucleated as the atoms collide. The nanocrystals move by Brownian motion in the gas, forming loose agglomerates when they meet. These particles, entrained in the gas, approach the sound velocity as the gas is drawn through a nozzle. The particles form a thin film of ballistically consolidated nanocrystals when they hit the substrate at high speed.

A variety of substrates were used in the depositions. A thin layer of metal (nickel or copper) was evaporated onto a nonwoven Crane fiberglass consisting of a web of uniformly

distributed fibers, approximately 8 μm in diameter. This provided a high surface area conductive substrate for the electrochemical cells. The nanophase silicon particles were deposited directly onto the metal-coated fiberglass. Other electrodes were prepared by first roughening the surface of the 2016 stainless steel coin cell using 400 grit sandpaper. A thin nickel/copper coating (~100 nm) was then evaporated on the surface and finally, the silicon was deposited directly onto the nickel/copper-coated planar substrate.[1]

6.3 Sample Characterization: As-Deposited Silicon

The ballistically deposited samples were found to be predominately crystalline. The XRD pattern of the ballistically deposited silicon material displayed in Figure 6.2 clearly shows sharp peaks corresponding to the diamond cubic positions of crystalline silicon. The large

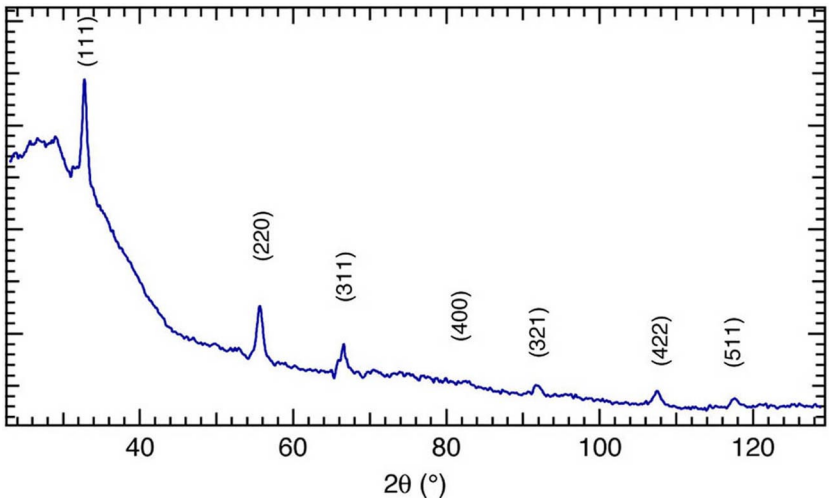

Figure 6.2: X-ray diffraction of nanocrystalline silicon on a glass substrate.

broad peak at ~ 30° is due predominately to the glass substrate, but may also mask contributions from an amorphous component, such as an a-silicon oxide that forms readily on the surface of silicon.

A more direct analysis of the microstructure of the ballistically deposited sample was performed by TEM. A bright-field/dark-field image pair and the associated electron diffraction pattern of the as-deposited nanophase silicon is displayed in Figures 6.3a-b. In the ballistically deposited electrode, the silicon nanocrystals form a web of interconnected particles. The most obvious features of these images are the small crystallites (5–20 nm in

[1]The planar substrate with a rough metallic surface has been used in similar experiments of Li et al. [97, 108] and Wang et al. [106].

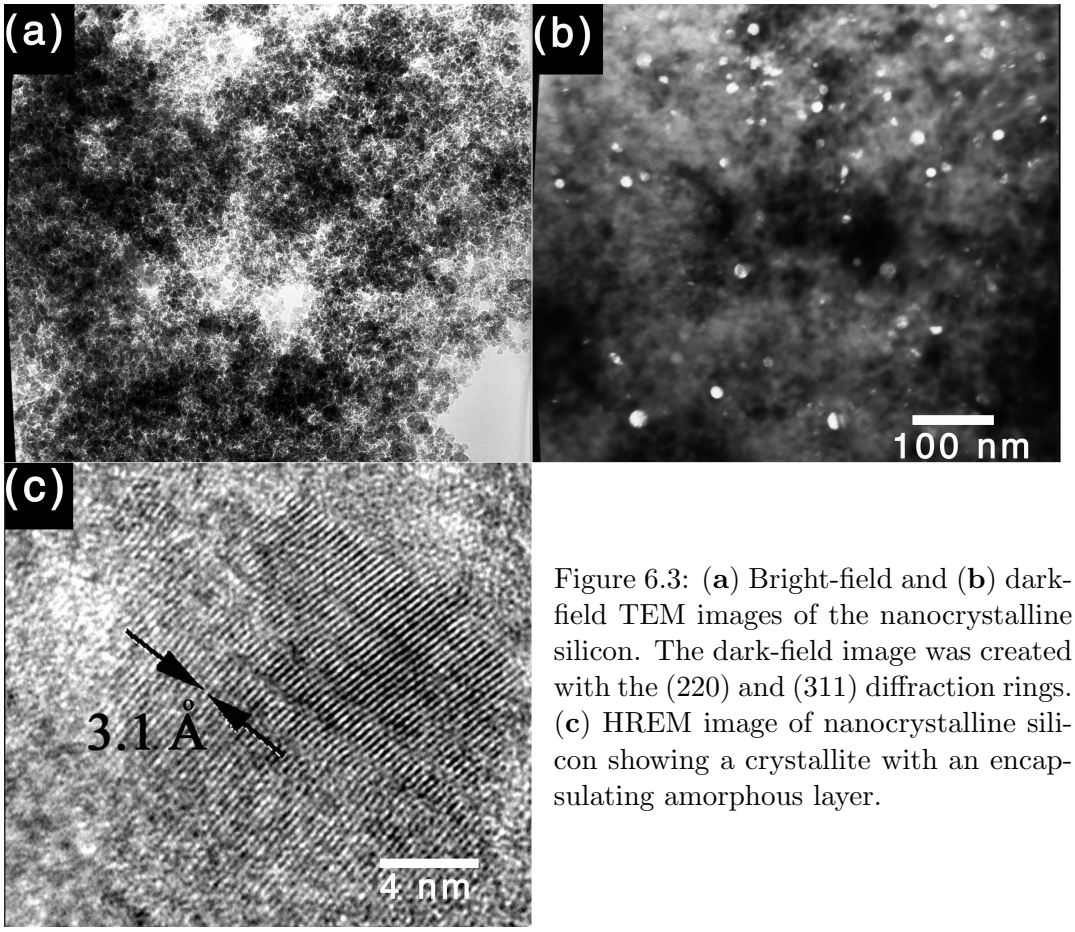

Figure 6.3: (**a**) Bright-field and (**b**) dark-field TEM images of the nanocrystalline silicon. The dark-field image was created with the (220) and (311) diffraction rings. (**c**) HREM image of nanocrystalline silicon showing a crystallite with an encapsulating amorphous layer.

diameter) and the low density of the material. The bright spots in the dark-field image correspond to small diamond cubic crystals of silicon having similar crystallographic orientations. HREM images displayed in Figure 6.3c clearly illustrate the complexity of the microstructure with the presence of crystallite and amorphous regions. The lattice fringes from the small crystallite in the center originate with silicon (111) planes separated by 3.1 Å. The region surrounding the crystallite appears to be an amorphous shell approximately 25 Å in thickness.

To quantify the concentration of oxide on the ballistically deposited silicon nanocrystals, EELS was performed on various regions of the sample. Figure 6.4a shows the silicon $L_{2,3}$-edges from standard samples of silicon and SiO_2 [5], a spectrum from the average of the two $1/2(I_{Si} + I_{SiO_2})$, and a spectrum from the ballistically deposited sample. Qualitative analyses of the near-edge structures from these samples confirm that the ballistically deposited samples consist of crystalline silicon and a-SiO_2. Taking the average of the silicon and SiO_2 silicon $L_{2,3}$-edges yields a spectrum that closely resembles that of the as-deposited

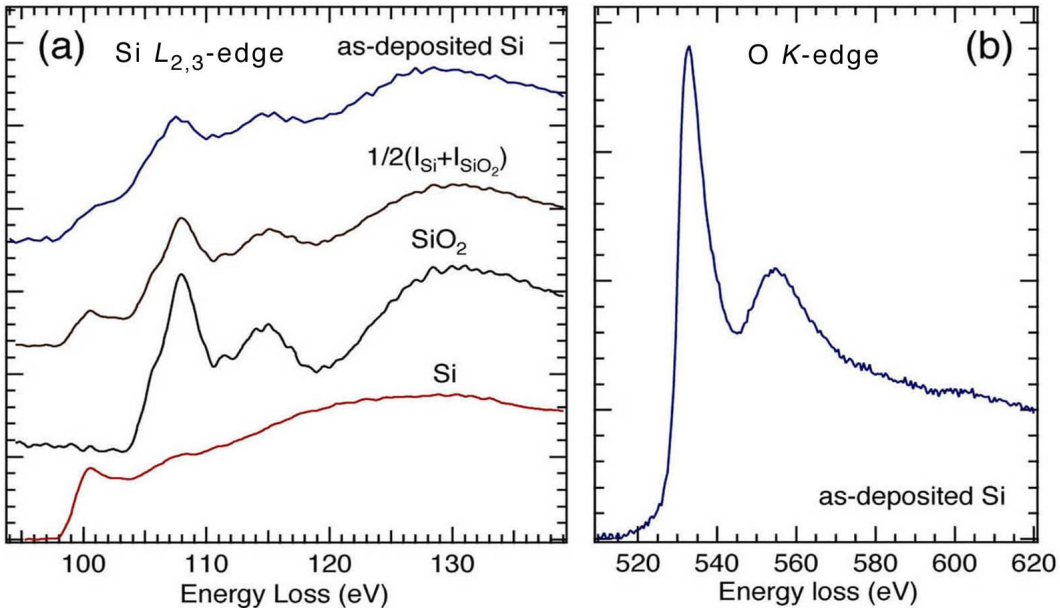

Figure 6.4: (**a**) Silicon $L_{2,3}$-edges from silicon and SiO_2 standards [5], the averaged spectrum from silicon and SiO_2, and the nanocrystalline silicon, as deposited. (**b**) Oxygen K-edge of ballistically deposited silicon nanocrystals confirming the presence of oxygen.

material. The oxygen K-edge from the silicon nanocrystals is shown in Figure 6.4b and further confirms the presence of oxygen. The shape of the O K-edge is characteristic of SiO_2, confirming that the oxygen contribution is not from a suboxide (such as SiO).

An elemental analysis was performed using the silicon $L_{2,3}$ and oxygen K-edges. The integrated intensity of the inner-shell edge was used to determine the atomic ratio of silicon to oxygen, $N_{\mathrm{Si}}/N_{\mathrm{O}}$. Using the thin film approximation (Equation 2.24), the atomic ratio ($N_{\mathrm{Si}}/N_{\mathrm{O}}$) for three different regions were measured to be 0.8-1.0 suggesting that the ballistically consolidated silicon films contain between 50-67% SiO_2. The evaporated silicon thin films contain far less oxygen.

X-ray diffractometry and TEM were also employed to characterize the structure of the evaporated silicon thin film. Figure 6.5 displays TEM bright-field images of the evaporated silicon in the planar and cross-sectional views. The TEM cross section indicates a film thickness of 100 nm. The absence of sharp peaks in the electron diffraction patterns (inset of Figure 6.5a) demonstrates that the material is entirely amorphous. The absence of long-range order was confirmed by XRD. The lack of structure in these images indicates that the silicon is deposited as a contiguous film, unbroken by grain boundaries, dislocations, or cracks.

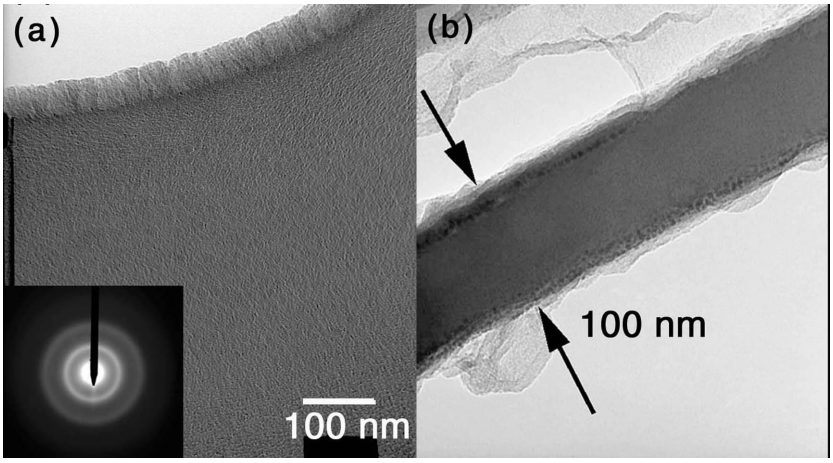

Figure 6.5: (**a**) Bright-field plan-view and (**b**) cross-sectional TEM images from evaporated amorphous silicon revealing the uniform, contiguous nature of the as-deposited 100 nm film.

6.4 Electrochemical Results

The nanocrystalline silicon clusters were initially prepared by deposition onto a nickel-coated fiberglass. Figure 6.6 displays SEM images of the nickel-coated fibers before and after the silicon deposition, and after the first complete electrochemical alloying with lithium (discharge). The nickel-coated fibers in Figure 6.6a have a smooth metallic surface and are approximately 8 μm in diameter. Figure 6.6b shows a conformal deposition of the silicon particles onto the metal-coated fibers. The nanoparticles are assembled into small islands of secondary particles (aggregates) approximately 100 nm in diameter. The smooth irregular surface of Figure 6.6c is indicative of the formation of a passivation layer upon lithiation.

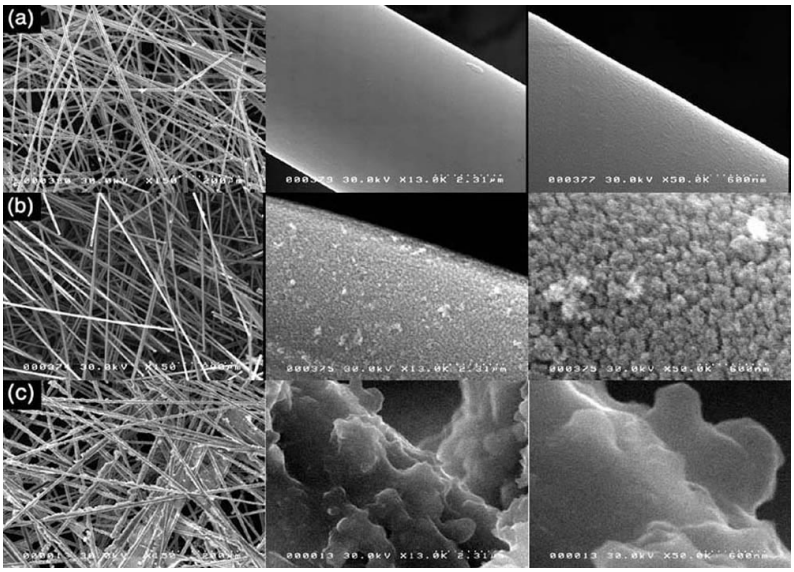

Figure 6.6: SEM images of (**a**) nickel coated fiberglass substrate, (**b**) nanocrystalline silicon on fibrous nickel substrate, and (**c**) nanocrystalline silicon after the first electrochemical alloying with lithium (discharged)

A plot of the voltage profile for cycles 1, 15, and 30 of the nanocrystalline silicon on a

nickel-coated fibrous substrate is shown in Figure 6.7a. Figure 6.7b displays a plot of the differential capacity, $\mathrm{d}|x|/\mathrm{d}E$, where $|x|$ is the absolute value of the lithium concentration and E is the cell potential. A large irreversible capacity was evident on the first cycle, which exhibited a discharge capacity (Q_d) of 5100 mAh/g and a charge capacity (Q_c) of 2250 mAh/g. This disparity yields a low coulombic efficiency ($Q_\mathrm{c}/Q_\mathrm{d}$) of 44%. The second cycle demonstrates a reversible capacity of 2100 mAh/g. A plot of the cycle life of the nanocrystalline silicon electrode prepared on a fibrous substrate is included in Figure 6.8. The coulombic efficiency was found to steadily increase during the electrochemical cycling reaching 98 % by cycle 30 (Figure 6.9). This suggests that in the early stages of cycling more lithium is inserted into the host than removed. The low coulombic efficiency is likely due to a high cell impedance. The increase in the cell efficiency is accompanied by a significant decrease in specific capacity.

Additional electrodes of nanocrystalline silicon clusters were prepared by ballistic consolidation on a rough, planar substrate. The voltage profiles from electrochemical cycles 1, 25, and 50 are displayed in Figure 6.7c. The differential capacity for these cycles is shown in Figure 6.7d. This electrode exhibited an initial discharge capacity of 2400 mAh/g during the first insertion of lithium, and a subsequent charge capacity of 1000 mAh/g, giving a coulombic efficiency of 41% for the first cycle. This high irreversible capacity was limited to the first cycle, however. Cycles 2–50 demonstrate a stable specific capacity of approximately 1000 mAh/g (Figure 6.8). The capacity fade correlates inversely with the coulombic efficiency, which was found to increase steadily up to 96% by cycle number 9 (Figure 6.9). In this reversible region, the nanocrystalline electrode exhibited a mean capacity loss of approximately 20 mAh/g per cycle with a final capacity of 525 mAh/g on cycle number 50.

Even better electrochemical performance was found for the thin amorphous films. The voltage profiles obtained from cycles 1, 25, and 50 are displayed in Figure 6.7e. The differential capacity is shown in Figure 6.7f. The initial discharge capacity of $\sim$3500 mAh/g suggests that up to 3.6 lithium atoms per silicon atom are involved in the initial alloying. The following charge capacity of 2500 mAh/g (2.6 lithiums per silicon atom) yields a coulombic efficiency of 71% on the first cycle. Upon subsequent cycling, the electrode exhibited a rather stable specific capacity $\sim$ 2000 mAh/g (Figure 6.8). The capacity stabilization corresponds to an increase in the coulombic efficiency to 98% on cycle number 9 (Figure 6.9). After 20 cycles, the amorphous thin film exhibited a mean capacity loss of

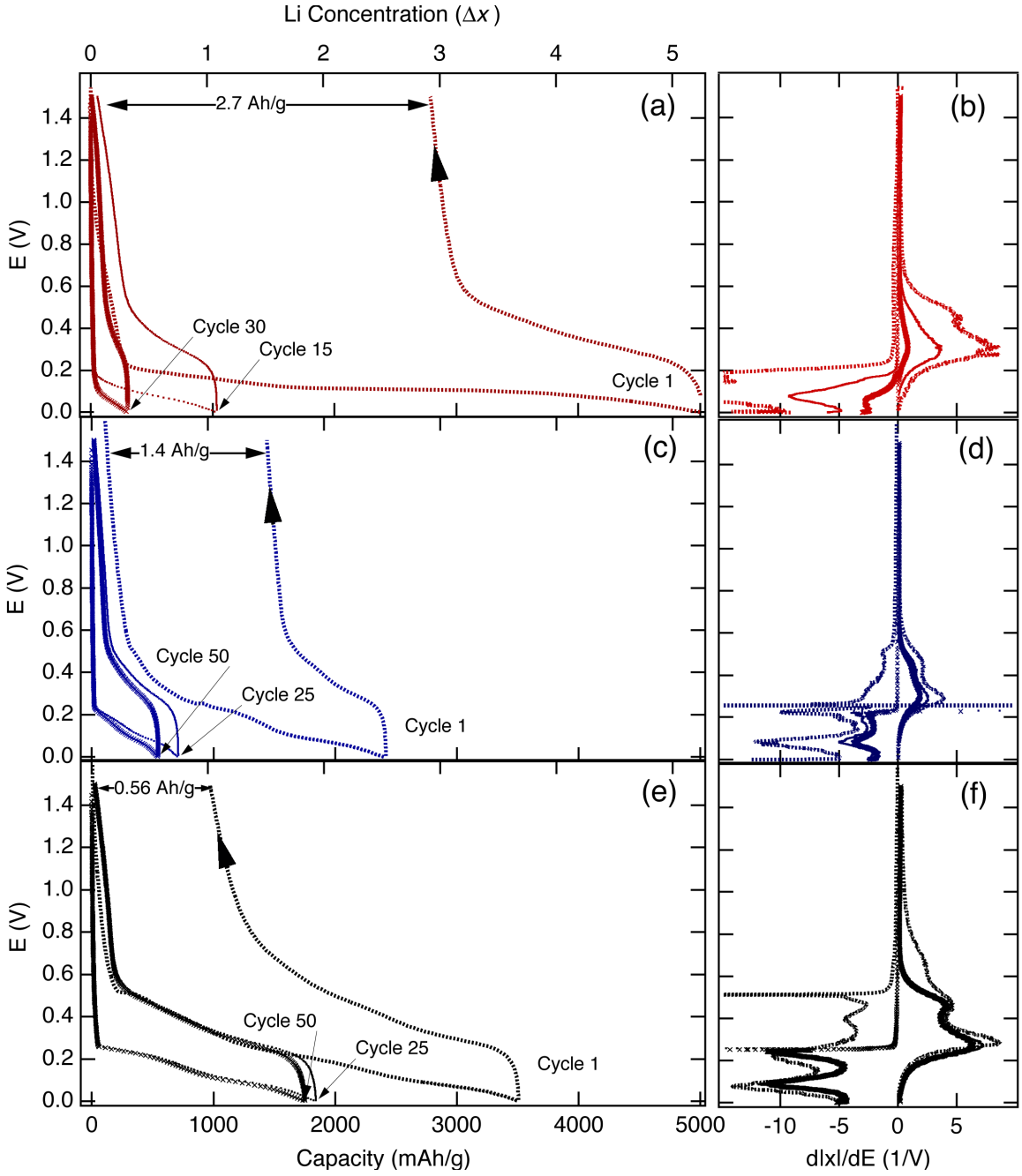

Figure 6.7: (**a**) Voltage profile and (**b**) differential capacity, $\mathrm{d}|x|/\mathrm{d}E$ for cycles 1, 15, and 30 from ballistically deposited silicon on a fibrous substrate. (**c**) Voltage profile and (**d**) differential capacity for cycles 1, 25, and 50 from ballistically deposited silicon on a planar copper substrate. (**e**) Voltage profile and (**f**) differential capacity for cycles 1, 25, and 50 from evaporated silicon. The arrows indicate the charge step of the first cycle. Δx corresponds to a change in lithium concentration of $\mathrm{Li}_x\mathrm{Si}$.

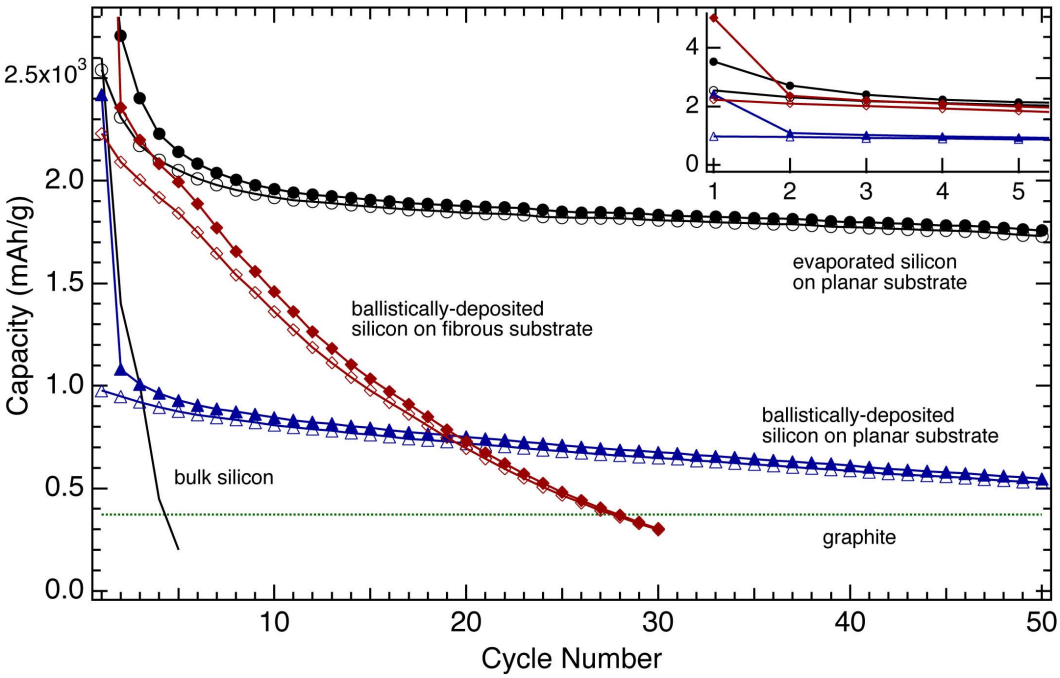

Figure 6.8: The gravimetric capacity of ballistically deposited silicon on a fibrous substrate, planar substrate, and evaporated silicon on a planar substrate. Light and shaded markers indicate charge and discharge steps, respectively.

only 8 mAh/g per cycle.

The kinetics of lithium diffusion in the silicon nanofilm were investigated using variable-rate electrochemical cycling. The charge/discharge rate is expressed in terms of half-cycles per hour. In this notation, a rate of $C/4$ denotes the current density required to completely charge/discharge the cell in 4 hours. The rate is normalized to correspond to the time required to lithiate the material to the empirical maximum capacity, C_0:

$$C \text{ Rate} = \frac{1}{t}\frac{C}{C_0}, \tag{6.1}$$

where t is the time (hours) required to reach the maximum voltage and C is the measured capacity. A 40 nm thick evaporated film was cycled four times at a typical rate of $0.25C$ (8 hour full cycle) to establish a stable capacity. Subsequent cycles were increased up to approximately $200C$ on the initial series. The electrode was then reduced back to $0.25C$ and the process was repeated up to approximately $500C$. Figure 6.10a displays a plot of the dependence of the gravimetric capacity on the cycling current. An evaporated silicon thin film of similar thickness ($\sim$ 40 nm) was cycled at a rate of approximately $100C$ to

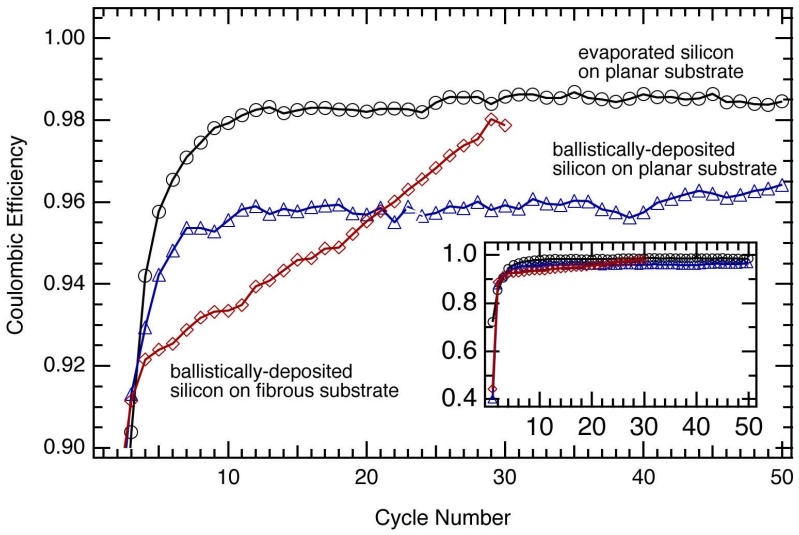

Figure 6.9: The coulombic efficiency of ballistically deposited silicon on fibrous and planar substrates, and evaporated silicon on a planar substrate.

determine the lifetime of the electrode when cycled at a high rate (Figure 6.10b). The capacity is stable $\sim$ 1600 mAh/g for a lifetime of 40 cycles.

6.5 Sample Characterization: Lithiated Silicon

An elemental analysis of the fully lithiated ballistically consolidated silicon was performed using quantitative EELS. The energy-loss spectrum in Figure 6.11 clearly shows a strong lithium K-edge at $\sim$ 54 eV. The edge intensity was determined using a 20 eV integration window about the lithium K-edge (55–75 eV) and silicon $L_{2,3}$-edge (99–119 eV). An atomic ratio was calculated using the ratio of the edge intensities weighted by the hydrogenic cross sections in the thin film approximation (Equation 2.24) [25]. The quantitative EELS analysis revealed an atomic ratio $N_{\mathrm{Li}}/N_{\mathrm{Si}}$ as large as 4.3 after the first discharge. This suggests that the lithiated stoichiometry is close to that of the $Li_{22}Si_5$ phase, and confirms that the lithium is not simply plated onto the surface but is actually inserted into the silicon host.

A TEM bright-field image and an electron diffraction pattern of the fully lithiated, ballistically deposited silicon are displayed in Figure 6.12. The broad diffuse rings of the electron diffraction pattern of Li-Si (Figure 6.12) indicate that the nanocrystalline silicon is amorphous in the lithiated state. These results lend credence to the notion that crystalline silicon transforms into a metastable glassy phase at room temperature through a mechanism known as electrochemically driven solid-state amorphization [109]. This transformation is

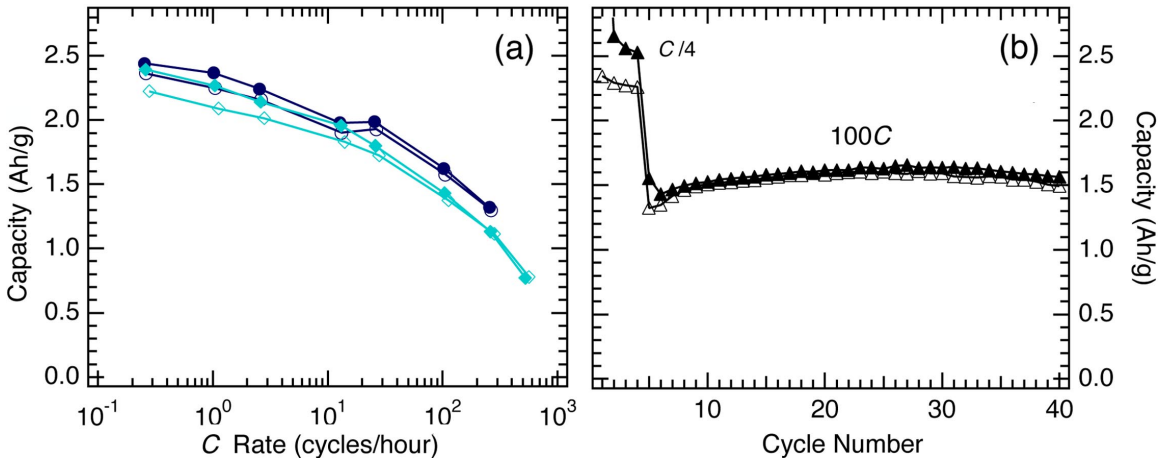

Figure 6.10: (**a**) Gravimetric capacity of an evaporated silicon nanofilm electrode at variable cycling rates (log scale). Light and shaded markers indicate charge and discharge steps, respectively. (○) First round of cycles up to $\sim 200C$. (◇) Second round of cycles (same electrode) up to $\sim 500C$. (**b**) Gravimetric capacity of evaporated silicon thin film at an initial rate of $C/4$ and a high rate of $\sim 100C$ exhibiting a stable cycle life.

also supported by the voltage profiles of Figures 6.7. The charge and discharge curves do not exhibit multiple flat plateaus, which appear when passing through different crystallographic phases.[2]

Although the voltage profiles vary slowly and continuously during cycling, there appear to be reproducible slope changes in the potential. These changes are manifested as peaks in Figs 6.7b,d,f, which plot the differential capacity ($\mathrm{d}|x|/\mathrm{d}E$) vs. cell potential. The 500 mV peak, which is only observed on the first few cycles, is indicative of a reaction of lithium with the surface of the electrode and electrolyte. The two primary peaks at 100 mV and 200 mV are relatively unchanged with cycling and suggest that some local preferential ordering does occur during lithiation. However, the smooth voltage profiles and diffuse electron diffraction pattern suggest that the long-range order is absent in the lithiated phase.

6.6 Discussion

6.6.1 Irreversible Capacity

The low coulombic efficiencies of the first cycles can be attributed in part to the formation of a solid-electrolyte interphase (SEI). This passivation layer is expected to form through

[2] According to the Gibbs phase rule, invariant regions of the voltage profile are indicative of a coexistence region.

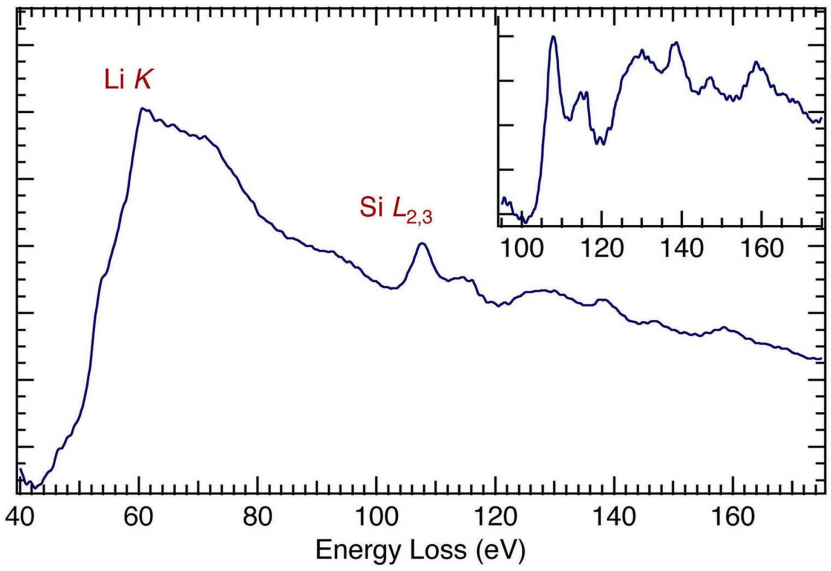

Figure 6.11: Lithium K-edge and silicon $L_{2,3}$-edge of fully lithiated silicon (discharged). The inset shows background subtracted silicon $L_{2,3}$-edge.

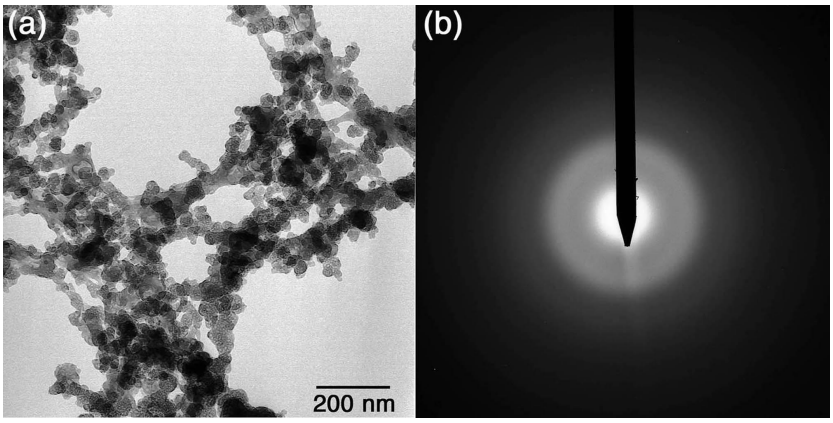

Figure 6.12: (**a**) Bright-field TEM image and (**b**) electron diffraction pattern of silicon electrode after the first discharge (fully lithiated).

a reaction of the lithium with the solvent (EC DMC) and the salts ($LiPF_6$) of the electrolyte. SEM images of the ballistically deposited silicon clusters after the first discharge (Figure 6.6c) reveal smooth electrode surfaces, in contrast with the fine-scale roughness of the as-deposited material. Although the change in the surface appearance could be partially attributed to the volume expansion during lithiation, there appears to be a contiguous passivation layer, which also emerges after the first lithium insertion. The formation of an SEI is also supported by the 500 mV peaks in the differential capacity plots of Figures 6.7b,d,f, which disappear after a few cycles. The formation of an SEI leads to an irreversible capacity through two mechanisms, the loss of lithium to the formation of the SEI and an increase in the cell impedance. Since the sharp capacity fade is limited to the first few cycles, we believe that the reactions contributing to the SEI layer occur during the initial cycles.

It is thermodynamically favorable for lithium to reduce SiO_2 (the native oxide on silicon)

through a displacement reaction:

$$4\mathrm{Li} + \mathrm{SiO_2} \rightarrow \mathrm{Li_2O} + \mathrm{Si}.$$

The formation of Li_2O is driven by the difference in the formation energies between a-SiO_2 ($\Delta G_f^\circ = -849.8$ kJ/mol) and $2Li_2O$ ($\Delta G_f^\circ = -1121.0$ kJ/mol) [110]. The free energy difference is equivalent to 704 mV. The formation of Li_2O from a convertible oxide is well documented in the SnO system, which has approximately twice the thermodynamic driving force of 1.58 V [111]. This irreversible reaction occurs in the early stages of the first discharge. It is followed by the alloying of the remaining lithium with elemental silicon. In the subsequent cycles the lithium is reversibly alloyed with silicon while the Li_2O remains inactive. The large irreversible capacity on the first cycle is considerably reduced in the cycling characteristics of the thin film electrode due to the low mass of the surface oxide relative to the bulk. It is likely that the large quantity of SiO_2 in the high-surface area nanocrystals is partially responsible for the reduced capacity observed in this material.

6.6.2 Adhesion

After cycle number 20 or so, the capacity fade may originate with a different mechanism. In the ballistically deposited silicon, we believe it originates with the spallation of silicon from the metal contact because such particles were found in the cell after extensive cycling. The absence of binder, coupled with a large volume change, are likely causes for the spalling of the silicon aggregates off the current collector. This later-stage capacity fade depended on the type and preparation of the substrate surface. Although this was not investigated systematically, the capacity fade was greatest for the nickel fibers, suggesting that the silicon aggregates are less prone to spalling off the planar substrate.

To demonstrate the variability in the cycling from the ballistically deposited silicon on the fibrous substrate, a total of 14 electrodes were prepared under similar conditions (with some variation in silicon mass) and cycled at a rate of around $C/4$. The cycling behavior of six of these electrodes is displayed in Figure 6.13, revealing reversible gravimetric capacities of up to 2500 mAh/g. The electrodes not shown exhibited cycling characteristics similar to those of Figure 6.13. A linear fit to these data demonstrates a reasonably consistent capacity fade during the initial cycling. However, a large variation is observed in the initial gravimetric capacity of these electrodes.

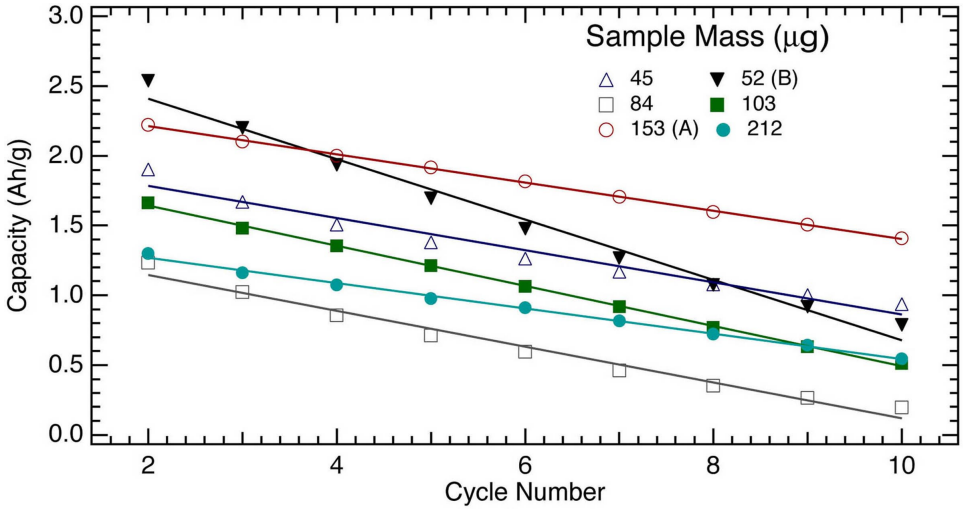

Figure 6.13: Average gravimetric capacities of cycles 2-10 for six nanocrystalline electrodes on nickel fibers. A linear fits to these data exhibit variable initial capacities with slopes of around −100 mAh/g per cycle. Electrode B exhibits a decay closer to −200 mAh/g per cycle.

The disparity in capacity fade was found to be greatest between electrodes labeled A and B. The capacity of electrode A faded at a rate of –100 mAh/g per cycle, while the capacity of electrode B decayed at a rate of –191 mAh/g per cycle. This variation appears to be independent of the total silicon mass, which was varied from 45 to 210 μg. The SEM image from the delithiated, cycled electrode A (Figure 6.14A), reveals recesses and cracks between particles, suggesting that much of the lithium has been removed. The passivation

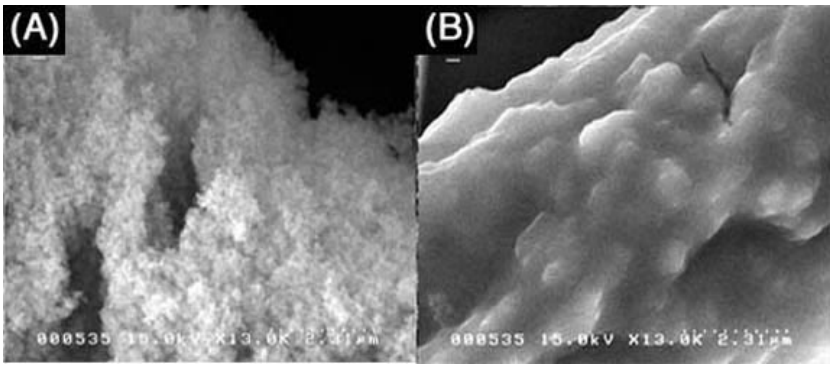

Figure 6.14: SEM images of electrode A and B after 30 cycles.

layer is broken apart during delithiation as the aggregates shrink back to their original size. After similar cycling, electrode B (Figure 6.14B) retains a smooth surface in the delithiated state, which resembles the surface of the fully lithiated electrode. Much of the lithium may be retained in these silicon particles suggesting that the increased capacity fade is due to a

loss of contact with the current collector during cycling.

6.6.3 Cycle Life: Strain Reduction and Defect Elimination

Compared to bulk silicon, which has essentially no cycle life, both types of nanostructured silicon have far superior performance during charge/discharge cycling. We attribute this improved cycle life to the absence of conventional mechanisms for microstructural damage. Dislocations have never been reported in crystals with dimensions of those considered in this study ($<$ 20 nm), probably because any such dislocations are quickly drawn to the surface by image forces. For brittle materials such as silicon, decrepitation occurs through the formation of cracks and their propagation by dislocation emission from the crack tip. For a crack to propagate, however, it must exceed a critical size, a_c:

$$a_c = \frac{2}{\pi}\frac{K_{1c}^2}{\sigma^2}. \tag{6.2}$$

The fracture toughness, K_{1c}, and yield strength, σ, in polycrystalline silicon are approximately 0.751 MPa/m$^{1/2}$ [112] and 1.1 GPa [113], respectively. These values yield a critical flaw size of $\sim$ 300 nm, much larger than the dimensions of our nanostructured electrode materials. Although this calculation is for pure silicon, the critical flaw size of lithiated silicon is not expected to be comparable to the dimensions of our films, which are nearly an order of magnitude smaller.

Gradients in strain can cause defect generation in solids, so gradients of lithium concentration could perhaps cause microstructural damage in bulk silicon. An advantage of nanostructured materials is that their relaxation times, τ, for diffusion are short, owing to their small dimensions, d, since $\tau = d^2/D$, where D is the diffusivity. The lithium concentration should be more uniform in nanostructured materials cycled at moderate rates.

The relatively open structure of the ballistically consolidated nanocrystalline silicon material seems capable of accommodating the large volume expansions of lithiation. We find it more difficult to understand why the amorphous silicon nanofilms were even more robust during electrochemical cycling. Both electrodes appear to be amorphous in the lithiated phase, and although this may suppress stress gradients, it is nevertheless expected that the volume expansion would lead to the decohesion of the film from its metal substrate. It is plausible, however, that the film is separated from the substrate along much of its interface,

making electrical contact at a few points. Perhaps the film bows outwards during lithiation, but remains anchored adequately for electrical continuity.

6.6.4 Kinetics

Extremely fast kinetics are observed in Figure 6.10a where the evaporated thin film was cycled at variable rates across three order of magnitude. These results indicate that the silicon film can be completely discharged in only a few seconds while maintaining close to half the empirical capacity (about 1100 mAh/g). This process can by equivalently described as the rapid alloying ($\sim 200C$) of lithium with silicon up to a stoichiometry of $Li_{1.2}Si$. The rapid lithium kinetics are made possible by the short diffusion lengths involved in the alloying process. Since the time scales for diffusion are proportional to the square of the diffusion length, nanostructured particles and films are generally able to accommodate high cycling rates.

In a typical electrode, the rapid insertion of lithium drastically reduces the gravimetric capacity and can lead to microstructural damage. Assuming a constant diffusivity, the strain gradients increase with the rate of lithium insertion. The increase of the strain energy raises the driving force for nucleating dislocations and cracks. An interesting feature of Figure 6.10a is that the there is no irreversible capacity associated with increasing the cycling rate by three orders of magnitude. The capacity at a $C/4$ rate is equivalent before and after the high-rate cycling, indicating that high current densities in the silicon nanofilm do not decrepitate the host. Figure 6.10b indicates that even at the high rate of $100C$, the electrode retains 67% of its original capacity. Remarkably, the fast cycling does not appear to degrade the overall cycle life of the electrode.

6.7 Conclusion

Nanostructured silicon electrodes prepared by gas-phase ballistic consolidation and evaporation were found to exhibit large reversible electrochemical capacities. The high capacity is expected from phase diagram of the Li-Si system, but the cycle life and fast diffusion kinetics depend on the nanostructured nature of the materials. Evaporated thin films demonstrated capacities of ~ 2000 mAh/g stable over 50 cycles. These films also exhibited rate capabilities up to $100C$ while retaining two-thirds of the original capacity. The silicon clusters formed

by ballistic deposition onto a high surface area fibrous substrate displayed reversible capacities as high as 2500 mAh/g with an attenuated cycle life. The absence of defects inherent in nanophase materials and their intrinsic ability to mitigate stress gradients, permits reversible lithium alloying with silicon without the particle decrepitation commonly observed in the bulk. The capacity fade in the ballistically deposited silicon clusters is attributed to decohesion and poor conductivity between aggregates and the current collector, which suggests that improvements will be made with the addition of a binder and a conductive diluent to maintain coherence between particles.

Chapter 7 High Lithium Capacity and High Rate Capabilities in Nanostructured Germanium

7.1 Introduction

Binary lithium alloys (Li-X) are currently of interest for anodes in electrochemical cells. In addition to their low operating voltage versus lithium (∼300 mV), these alloys exhibit large theoretical energy densities. The largest gravimetric capacity of the group IV alloys is found in Li-Si, which can accommodate up to 4.4 lithium atoms per silicon. Despite the promising energy densities of these alloys, a large volume expansion is associated with lithiation and the resulting stresses tend to decrepitate the host after a few cycles [92, 93, 94, 95, 96]. In addition, the slow kinetics of lithium transport have limited the application of these anodes to medium and high temperature cells using molten electrolytes [84, 85, 114].

Recent investigations into the electrochemical properties of the Li-Si system have demonstrated an improved room temperature cycle life in nanocrystalline and thin film electrodes [96, 97, 105, 115]. However, investigations of an analogous system, Li-Ge, have received little attention owing to the high cost and larger mass of germanium. The Li-Ge system has a theoretical capacity of of 1.6 Ah/g, which is only 40 percent of the Li-Si capacity. Despite the reduced energy density, germanium does not have a strong affinity to form a native oxide layer. In a high surface area material such as a nanostructured material, a thin contamination layer can be detrimental to the total capacity. Therefore, Li-Ge is a model alloy for investigating the properties of the Li-X (X = Si, Ge, Sn, Pb) system while avoiding artifacts due to a native oxide layer (such as the displacement reaction involving lithium oxidation and tin reduction in the SnO_2 system).

In addition to providing general insights into the Li-X system, Li-Ge may be a logical candidate anode for lithium secondary cells. The high cost of elemental germanium has limited research efforts on this system in the past. However, germanium is an abundant element in the earth's crust and the current price is maintained by the lack of demand. The Li-Ge anode has a number of advantages over Li-Si, one of which is the reduced affinity to form a native oxide. In addition, the diffusivity of lithium in germanium is approximately

15 times greater than that of lithium in silicon at 360° C (2.14×10^{-7}cm^2/sec for Ge and 1.47×10^{-8} cm^2/sec for Si) [116]. The room temperature diffusion rates can be approximated using the empirical diffusion equation:

$$D = D_0 \exp[-Q/RT], \tag{7.1}$$

where T is the temperature, Q is the activation energy, and D_0 is the $T = 0$ diffusion constant. This equation suggests that the diffusivity of lithium in germanium may be over 400 times that of lithium in silicon at 300 K (using values Q(kJ/mol)/D_0(cm^2/sec$\times 10^7$), 64/0.0023 for silicon and 49/0.0025 for germanium [116]).

7.2 Experimental

Electrodes were prepared by two different methods utilizing physical vapor deposition. In the first, evaporation, a charge of elemental germanium was heated resistively above the melting point (1210 K) in a tungsten wire basket. The material was evaporated in a vacuum of 2×10^{-6} torr and deposited directly onto a substrate located below the evaporating basket. The second method, gas-phase ballistic consolidation, used a "forming gas" of 90% Ar_2 and 10% H_2 (2×10^{-3} torr), which was streamed through the deposition chamber. The elemental charge was evaporated and cooled quickly in the forming gas, thereby nucleating nanoscale crystallites within the gas. The Brownian motion of the germanium nanoparticles entrained in the gas generates nanocrystalline aggregates that form a "web" of nanocrystalline material on the substrate.

The germanium electrodes were prepared as-deposited on planar nickel substrates. The surface of the substrates were roughened using 400 grit sandpaper. The mass of the deposited material was determined using a Metler micro-balance accurate to 1 μg. In the interest of a purely fundamental investigation of the electrochemical behavior of nanoscale germanium, no conductive additives or binders were used in the nanostructured electrodes.

Electrodes of bulk germanium were prepared by crushing elemental germanium into a powder of particle size less than 38 μm. A binder of 10 wt.% polyvinylidene fluoride and a conductive diluent of 8 wt.% acetylene black (graphite) were added to the powder to improve the cycling characteristics. The electrode powder was pressed into a pellet using a

pressure of approximately 90 MPa.

The germanium electrodes were cycled in 2016 coin cells using lithium metal as a counter electrode. A standard mixture of ethylene carbonate and dimethyl carbonate (EC DMC) with $LiPF_6$ was used as the electrolyte and a 0.50 mm thick strip of fiberglass was used as a separator. A polyethylene separator was used in the bulk germanium cell. The electrochemical tests were performed with an Arbin Instruments BT2000 battery cycler.

Transmission electron microscopy was performed in a Philips EM 420 at 100 kV. The TEM samples were prepared by physical vapor deposition onto a holey carbon grid. X-ray diffraction was performed with an INEL CPS-120 diffractometer using Cr $K\beta$ radiation ($\lambda = 2.0848\,\text{Å}$).

7.3 Sample Characterization

The two deposition methods generated unique films with distinct microstructures. Bright and dark-field TEM images of the germanium film prepared by ballistic consolidation are displayed in Figure 7.1a–b. The dark-field images were created using the (111) diffraction ring. The film consists of a web of interconnected nanocrystalline germanium with a mean particle diameter of 10 nm. The crystalline structure is clearly visible from the distinct bright spots in the electron diffraction pattern displayed in the inset of Figure 7.1. The diamond cubic structure was confirmed by x-ray diffraction as shown in Figure 7.1c. The broad peaks are are indicative of a small particle diameter. The mean particle diameter was approximated from the diffraction peak widths using the Scherrer equation [2] and determined to be ~ 12 nm.

A very different microstructure was obtained when the germanium was simply evaporated in high vacuum. In this method, the germanium formed a continuous thin film as seen in the bright-field TEM images displayed in Figure 7.2a-b. The broad rings of the electron diffraction pattern displayed in the inset of Figure 7.2a suggest the material is entirely amorphous. In the middle of the film the material appears to be contiguous and uniform, while the material on the edge of the holey carbon substrate appears to have a columnar structure. It is likely that this structure is not representative of the entire film and is simply an artifact of the substrate edge.

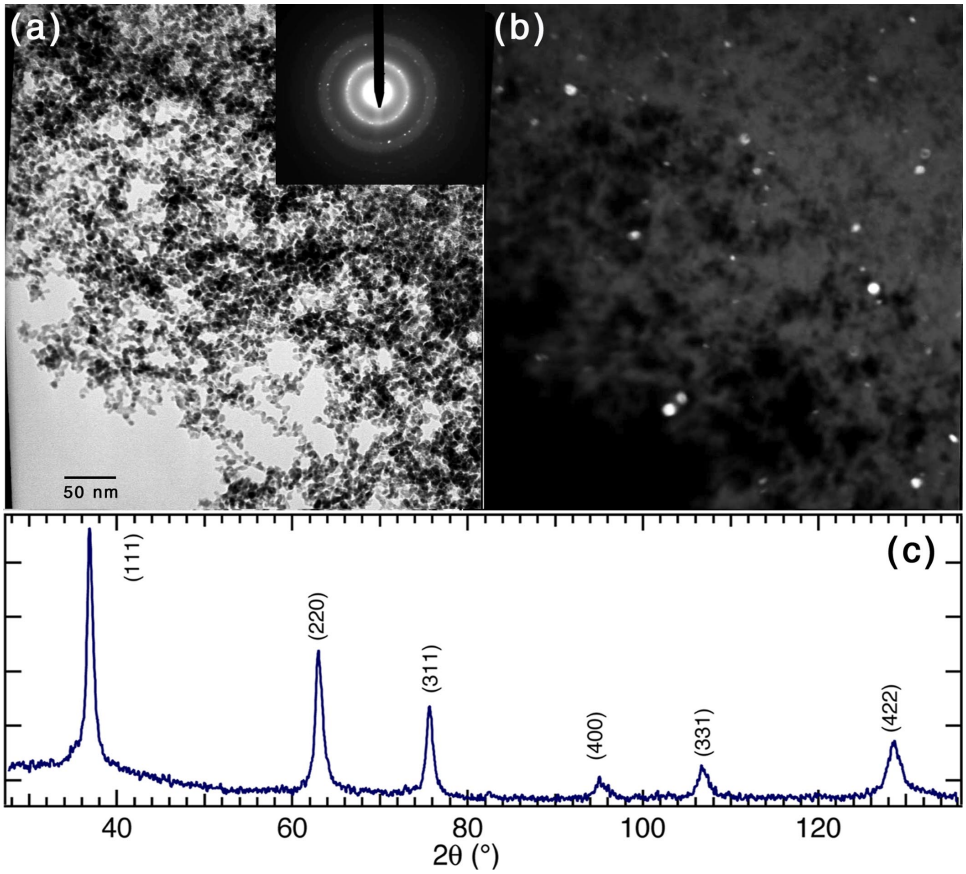

Figure 7.1: (**a**) Bright-field and (**b**) dark-field TEM image of ballistically deposited germanium nanocrystals. The electron diffraction pattern is displayed in the inset. (**c**) X-ray diffraction pattern of germanium nanocrystals showing diamond-cubic peak positions.

7.4 Electrochemical Results

A plot of the voltage profiles from a 236 μg electrode of ballistically deposited nanocrystalline germanium and a 42 μg electrode of an evaporated germanium nanofilm are shown in Figure 7.3. The most salient feature of this plot is the high reversible capacity of the nanostructured electrodes. The evaporated germanium nanofilm accommodates approximately 4.5 lithium atoms per germanium atom, which is slightly higher than the theoretical limit for crystalline $Li_{22}Ge_5$. The film thickness is estimated to be 60 nm based upon the electrode mass and bulk material density. Thicker films of up to 250 nm (180 μg) were cycled at slower rates and demonstrated similar results. The ballistically deposited material hosts up to 3.8 lithium atoms per germanium atom. A plot of the differential capacity, $\mathrm{d}|x|/\mathrm{d}E$, is displayed in Figure 7.3b and Figure 7.3d, where x is the lithium concentration in Li_xSi and E is the cell potential. The peaks are indicative of lithium insertion into equipotential sites.

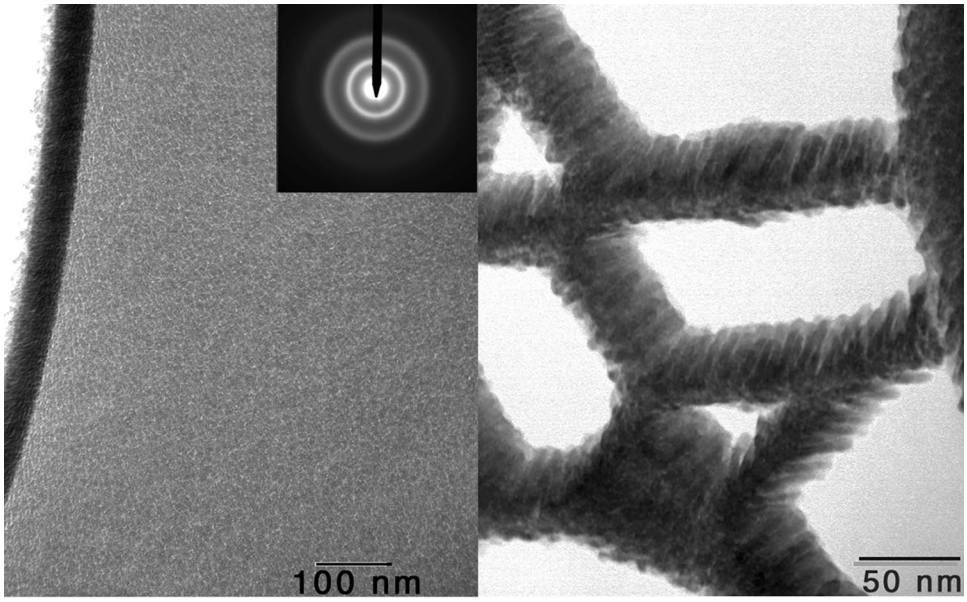

Figure 7.2: Bright-field TEM images of the evaporated film showing (**a**) the uniform film surface and (**b**) the columnar structure apparent at the edges of the film. The electron diffraction pattern is displayed in the inset.

These plots suggest that in both electrodes the lithium insertion and extraction occurs at ~ 200 mV and ~ 500 mV, respectively. The disparity is due to the over potential resulting from the constant current, or nonequilibrium state. The potential for lithium insertion and extraction at equilibrium can be approximated by the average of the charge and discharge values, which is ~ 350 mV at room temperature.

Plots of the cycle life for bulk crystalline germanium (grain size ≤ 38 μm) and the two types of nanostructured germanium electrodes are displayed in Figure 7.4. The nanostructured electrodes were cycled at a rate of approximately $C/4$ between 0 and 1.5 V, whereas the bulk electrode was cycled a much slower rate ($\sim C/30$) to maximize the specific capacity. Despite the gentle cycling conditions, bulk germanium exhibited a poor cycle life, with nearly complete capacity loss by the seventh cycle. The germanium nanofilm exhibits a large first-cycle irreversible capacity with a remarkably constant specific capacity ~ 1.7 Ah/g. A similar first cycle capacity loss is observed with the ballistically deposited germanium. Although the initial stable capacity is similar to that of the evaporated nanofilm (~ 1.4 Ah/g), the ballistically deposited electrode exhibits a constant capacity fade of approximately 0.01 Ah/g per cycle.

The rate capabilities of the nanostructured electrodes were also investigated. A 250

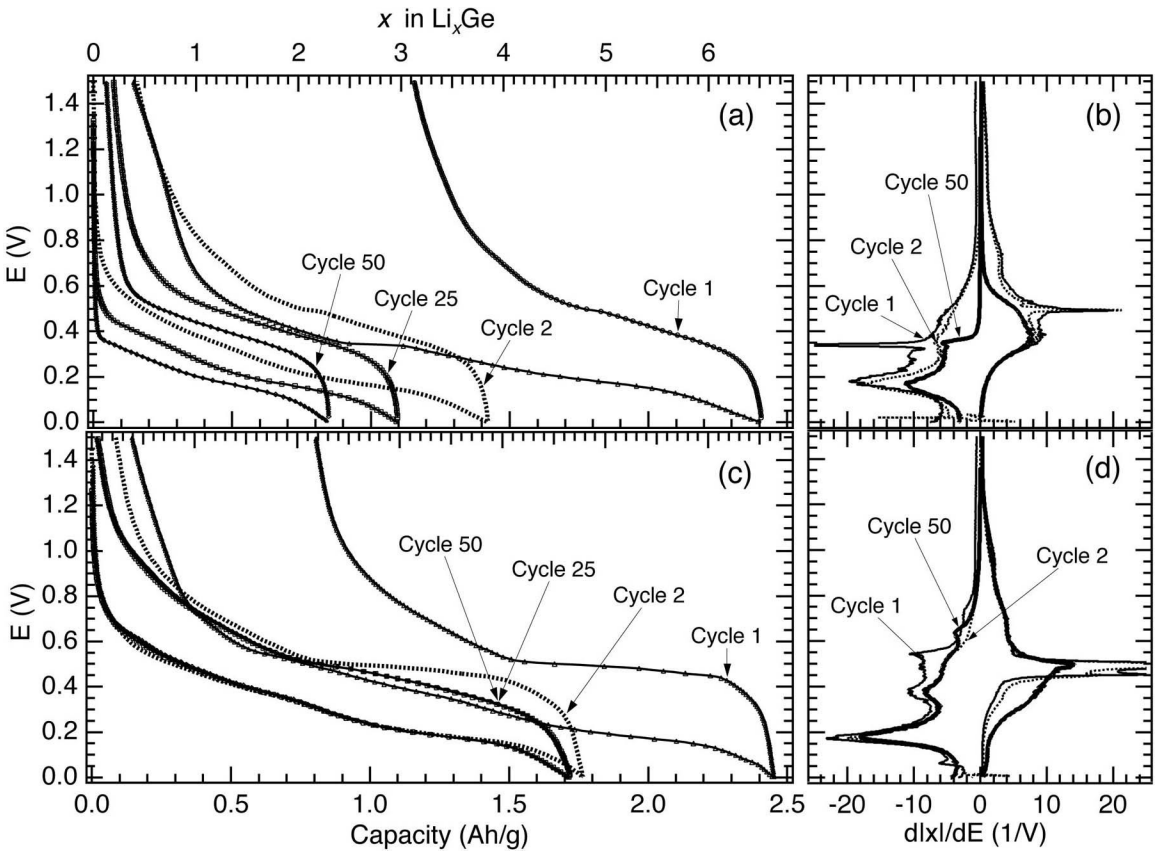

Figure 7.3: (**a**) Voltage profiles and (**b**) differential capacities from ballistically deposited germanium. (**c**) Voltage profiles and (**d**) differential capacities from evaporated germanium. The arrows indicate the charge step of the first cycle.

nm evaporated film of amorphous germanium (180 μg) was cycled at a constant discharge rate of $0.5C$ and a variable charge rate between $0.5C$ and $1000C$. A ballistically deposited nanocrystalline film (314 μg) was cycled under similar conditions. Figure 7.5 shows a plot of the normalized capacity (Q/Q_0) at various discharge rates. The vertical error bars reflect the uncertainty associated with the data acquisition system and are only visible when the charging times are short. Remarkably, only a moderate capacity loss is observed between $1C$ and $1000C$.

A test of the cycle life at high rates was also performed on the amorphous thin film electrode. In this experiment the 250 nm germanium film was cycled at a discharge rate of $0.5C$ and a charge rate of $1000C$. Figure 7.5b displays a plot of the charge and discharge capacities over 30 cycles.

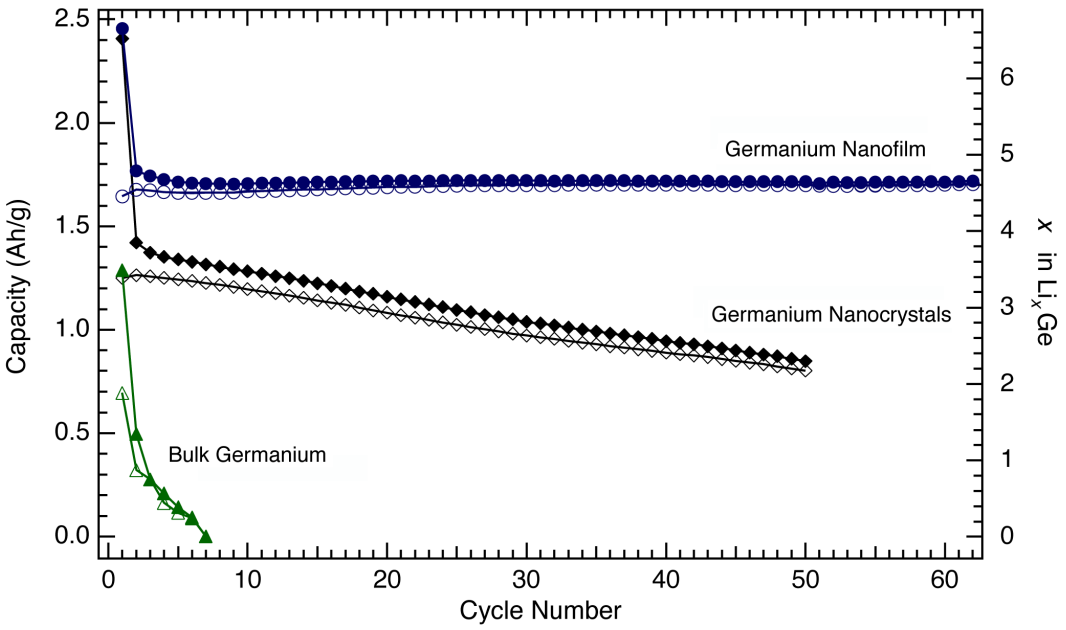

Figure 7.4: Cycle life of germanium from ballistically deposited nanocrystals, an evaporated amorphous nanofilm, and bulk crystalline germanium. The light and shaded markers represent the charge and discharge cycles, respectively.

7.5 Discussion

The occurrence of phase transitions in lithium alloys is typically a detriment to the cycle life. Phase transitions are easily identified by plateaus in the voltage profile. Gibbs' phase rule prohibits any variation in the chemical potential (or cell voltage) when two simultaneous phases are present. In a two phase region the potential is fixed over changes in lithium concentration as one phase grows at the expense of the other. The voltage profiles of Figure 7.3a and Figure 7.3c exhibit a reasonably smooth slope on the charge and discharge cycles for both of the nanostructured electrodes. The differential capacity (Figure 7.3b and Figure 7.3d) is used to accentuate changes in the slope of the potential curve. Peaks in the differential capacity indicate regions of the potential where lithium ions are entering nearly equipotential sites. The occurrence of multiple small peaks suggests that some local ordering does occur during cycling. However, the multiple sharp peaks expected from the crystallographic phase transitions observed at high temperatures are not observed in the nanocrystalline material at room temperature. In addition, the nanocrystalline voltage profile is remarkably similar to that of the amorphous film suggesting that both electrodes remain amorphous in the lithiated state.

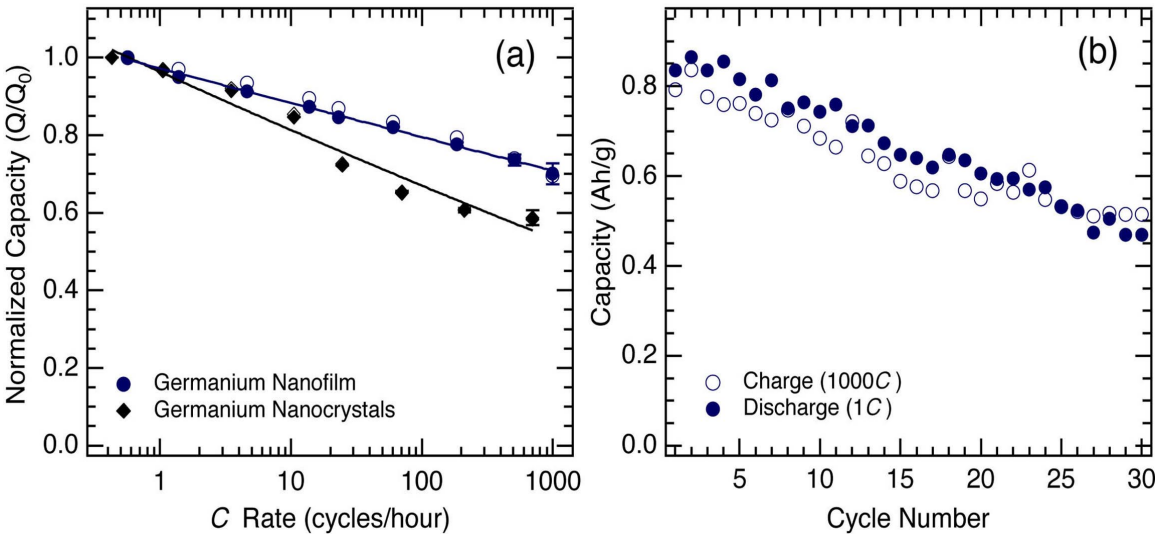

Figure 7.5: (**a**) Rate capabilities of ballistically deposited germanium and an evaporated thin film. The electrodes were lithiated (discharged) at a constant rate of $1C$ and delithiated (charged) at a variable rate. (**b**) Cycle life of the amorphous germanium thin film at a lithiation rate of $1C$ and a delithiation rate of $1000C$. The light and shaded markers represent the charge and discharge cycles, respectively.

The transformation from crystalline to amorphous germanium occurs by a mechanism known as electrochemically driven solid-state amorphization (ESA). This phase transition is well documented in the silicon system where electrochemical alloying of lithium has been shown to form a metastable glassy phase at room temperature [109]. The single flat plateau in the voltage profile suggest that ESA also occurs in the germanium system. As originally suggested by Limthongkul et al., the amorphization is driven by the room temperature thermodynamics and kinetics and is not attributed to the nanoscale microstructure [109].

The large irreversible capacity observed on the initial cycle is likely attributed to the formation of a solid-electrolyte interphase (SEI). A reaction of lithium with the electrolyte accompanies the initial lithiation of the germanium electrode forming a passivation layer. This reaction is beneficial when using a carbon electrode because it prevents solvent cointercalation during lithiation. The passivation layer is unnecessary in lithium alloy electrodes since they are not affected by solvent cointercalation. However, the SEI layer does not appear to be detrimental to the specific capacity or cycle life. The first cycle capacity loss is approximately 70% of what was observed in the Li-Si system [115]. The decrease in the first cycle irreversible capacity may be attributed to the lack of a native oxide on germanium,

which might otherwise contributed to the SEI.[1]

The high specific capacities of the nanostructured germanium electrodes were found to be stable for over 50 cycles (Figure 7.4). Although the high capacities are expected from the high solubility of lithium in germanium, the complete lithiation of germanium has never been observed at room temperature on these time scales. Similarly, the slow kinetics of lithium in germanium are expected to create large stresses within the material causing the decrepitation of the host. This is clearly observed in the attenuated cycle life of the bulk germanium electrode (Figure 7.4). Remarkably, there is no capacity loss observed in the amorphous nanofilm over 62 cycles. Similarly, the nanocrystalline electrode exhibits only a slow loss of capacity over 50 cycles. These results indicate that the active germanium particles do not severally decrepitate during electrochemical cycling. The constant capacity loss observed in the nanocrystalline system is attributed to the spallation of particles off the surface of the current collector resulting from changes in the sample volume by up to 300% during cycling.

The stability of the amorphous nanofilm during cycling is rather surprising. Although this electrode is thin, suggesting rapid lithium transport perpendicular to the film, the electrode is attached to a rigid substrate. The 300% volume expansion that occurs during lithiation is expected to create considerable strain gradients as the lithium front propagates in and out of the film. The strains are more than sufficient to overcome the surface energy bonding the film to the substrate. However, there cannot be a complete decohesion of the film during cycling because the film is electrically intact. It is possible that during lithiation there exist localized low energy sites that are preferentially filled. The preferential ordering is supported by the voltage profiles in Figure 7.3 which exhibit a number of minor slope changes that are consistent with the insertion/extraction of lithium from different sites. The local ordering of lithium would effectively reduce the mechanical strains of lithiation by allowing the volume changes to occur more homogeneously. Although the preferential ordering may reduce some of the alloying strains, another mechanism is necessary to explain the adherence of the film to the substrate. It is possible that the film may "buckle" in some regions, which would dissipate much of the lattice stress while maintaining contact with the current collector.

[1]The native oxide in germanium is limited to a few monolayers, whereas in silicon the surface oxide extends up to ~ 25 Å.

The cycling stability of lithium in the ballistically deposited germanium is easier to understand. The reversibility is attributed to the absence of conventional mechanisms for microstructural damage in nanoscale materials [115]. The formation and propagation of cracks is prohibited due to the absence of dislocations and the large critical flaw size, with respect to the particle diameter. The mitigation of particle decrepitation is also attributed to the short timescales required for lattice relaxation in nanostructured materials. As mentioned in Chapter 6, the relaxation time is proportional to the square of the diffusion distance. The diffusion of lithium into the host distorts the lattice parameter, a, to approximately $3^{1/3}a$. The strain is not intrinsically harmful to the host, but rather it is the gradients in strain that are responsible for breaking apart the electrode during cycling. When the diffusion lengths are short, the relaxation times are short and the material is strained uniformly.

The reversible cycling of 4.5 Li/Ge in the amorphous thin film and 3.8 Li/Ge in the nanocrystalline film are considerably larger than the capacities measured in the analogous silicon system. Silicon electrodes prepared and cycled under similar conditions exhibited reversible capacities of 2.1 Li/Si in the amorphous thin film and 1.1 Li/Si in the nanocrystalline film. The increase in reversible lithium uptake in the germanium system is attributed to the higher diffusivity, D, of lithium in germanium at room temperature ($D_{\mathrm{Ge}} \approx 400 D_{\mathrm{Si}}$). In addition, the 25 Å native oxide on the surface of the silicon electrode reduces the overall specific capacity and likely contributes to SEI formation, which increases the cell impedance.

High rate capabilities are expected in nanostructured electrodes due to the short relaxation times and the fast kinetics of lithium transport. For solid state diffusion, the time required for a system to relax is proportional to the square of the diffusion distance (i.e., particle diameter or film thickness). Therefore, diffusion through a 10 nm particle will occur 10,000 times faster than through a 1 μm particle. The high rate capabilities of nanostructured electrodes are well documented and cycling rates of up to $4000C$ have been demonstrated in vanadium oxide [102]. Therefore, it is not surprising that the results of Figure 7.5 indicate high rate capabilities in the nanostructured germanium electrodes. The capacities measured at variable charging rates (Figure 7.5a) indicate a slow power-law (linear on a log scale) capacity decay up to $1000C$. There is no indication of a catastrophic loss of capacity typically associated with an electrochemical cell limited by solid state diffusion. The voltage profiles at $1000C$ are similar to those at $0.5C$ indicating that the lithium is alloyed with the host and not simply plated on the electrode surface.

7.6 Conclusion

Electrodes of nanostructure elemental germanium were found to electrochemically alloy $\sim$ 80 at.% lithium, consistent with the $Li_{22}Ge_5$ phase in crystalline Li-Ge. A high initial specific capacity was measured in bulk germanium. However, the complete loss of capacity after only a few cycles suggests that large particles decrepitate during cycling as a result of the large alloying strains. In contrast, thin films of amorphous germanium exhibited capacities of 1.7 Ah/g with no capacity loss over 62 cycles. Nanocrystalline germanium was found to transform into an amorphous alloy upon lithiation and exhibited capacities of up to 1.4 Ah/g with $\sim$ 60% capacity retention after 50 cycles. The high reversibility is attributed to nanoscale microstructure of these electrodes. The short diffusion paths reduce strain fields and mitigate microstructural cycling damage. The short diffusion distances are also responsible for the high rate capabilities of these electrodes, which withstood rates of up to $1000C$ with only a moderate reduction of capacity. These results suggest that nanoscale microstructures can be used to increase diffusion rates and reduce particle decrepitation in lithium alloy electrodes.

Chapter 8 Future Work

8.1 Introduction

The market for lithium batteries is currently dominated by consumer electronics (e.g., laptops and cell phones) and presently lithium batteries are a three-billion-dollar industry. Potential new markets such as hybrid and electric vehicles will likely drive the research in new directions in the future. Research on lithium storage materials will continue to address fundamental questions concerning the electronic structure and thermodynamics of the lithium hosts during lithiation. However, new markets will increase the demand for fast kinetics of lithium transport with higher gravimetric and volumetric capacities while maintaining a high level of consumer safety.

Nanomaterials for electrodes in lithium batteries have shown the best combination yet achieved of high storage capacity plus cycle life. The necessity for enhanced rate capabilities will continue to inspire studies of the rapid solid-state diffusion in nanostructured electrodes. The high concentration of grain boundaries will require investigations into grain boundary diffusion and the possibility of lithium storage in grain boundaries. Finally, the promising electrochemical results of Chapters 6–7 indicate the need for a better understanding of stresses in nanomaterials, especially thin films.

8.2 Electronic Structure

The voltage of a secondary cell depends on the redox processes that occur during cycling. The results of Chapters 4–5 suggest that the oxygen ion plays a significant role in charge compensation during cycling and that the stability of at least one transition-metal ion in the host may be a critical component to maintaining a long cycle life. An obvious extension of this work is to investigate charge compensation in other systems such as $LiNiMnO_2$ and the $LiTMPO_4$. Recent calculations of Reed and Ceder have predicted that in $LiNiO_2$ and $LiNiMnO_2$ the nickel ions will disproportionate into Ni^{2+} and Ni^{4+} [117]. The disproportionation of the nickel ions in $LiNiMnO_2$ allows the manganese ions to remain fixed at

Mn^{4+}. The stability of the manganese valence could be confirmed by studying the $L_{2,3}$-edge at different states of charge. The disproportionation of the nickel ions would be difficult to confirm through the integrated white line intensities. Characteristic features of the edge, such as the L_3/L_2 ratio, may be used to identify multivalent nickel ions. The dependence of the white line ratio on d occupancy is well characterized for the $3d$ transition-metal series (Chapter 3). The nickel valence may also be characterized using the near-edge structure from high resolution energy-loss spectra acquired with a field emission gun or soft x-ray absorption spectra acquired with synchrotron radiation. The reduced nickel ion (Ni^{2+}) should exhibit narrower white lines that are shifted in energy with respect to (Ni^{4+}). It may be possible to resolve the peak multiplets using high resolution spectra with line widths of < 0.5 eV.

Recent Mössbauer results from the $LiFePO_4$ [118] and $LiFeMnPO_4$ [119] systems indicate that during lithium insertion/extraction the iron valence varies between Fe^{2+} to Fe^{3+}. A two-phase region exists during delithiation, where the $FePO_4$ phase grows at the expense of the $LiFePO_4$ phase. The growth of the trivalent iron phase is evident in the Mössbauer spectra from our own analysis of the $LiFePO_4$ system (Figure 8.1).[1] Mössbauer

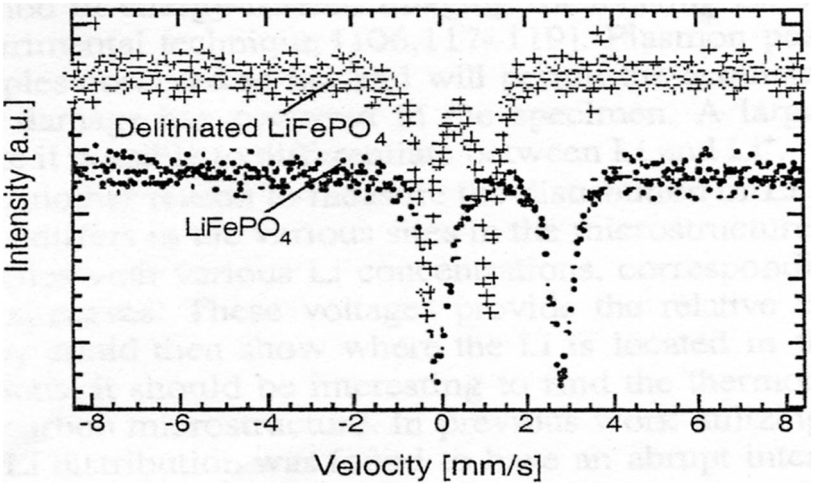

Figure 8.1: Mössbauer spectra from $LiFePO_4$ and delithiated $LiFePO_4$ acquired in transmission geometry.

spectroscopy is a useful technique for studying valence changes in the $LiFePO_4$ system due to the Mössbauer nucleus of the ^{57}Fe isotope and the disparity between the Fe^{3+} and Fe^{2+} hyperfine fields. However, a different approach must be used to understand the role of other transition-metal ions in this system ($LTMPO_4$ and $Li(Fe,TM)PO_4$). Such an investigation may be performed through an analysis of the $L_{2,3}$ white lines and near-edge structure using

[1] Mössbauer experiments were performed by Alex Papandrew and Joanna Dodd.

EELS or XAS.

8.3 Chemical and Valence Mapping

Heterogeneities in lithium concentration have been observed in chemically delithiated samples of $LiNiCoO_2$ (Chapter 5). It is logical to assume that heterogeneities of this nature are also present in the electrochemically delithiated material. If so, it will be important to know how the lithium varies throughout the material at different states of charge. Microbeam energy-filtered imaging with the lithium K-edge can be used to produce a map of the lithium distribution in a material. This information will lead to a better understanding of the role of the grain boundaries in lithium electrodes. In addition, the distribution of lithium in the delithiated material will yield insights into how concentration gradients stress the system and how the stresses are distributed throughout the material.

Producing a chemical or valence map requires a series of energy-filtered images and care must be take when interpreting the image. As an example, a chemical map was produced from a series of energy filtered images acquired with the oxygen K-edge (Figure 8.2). The

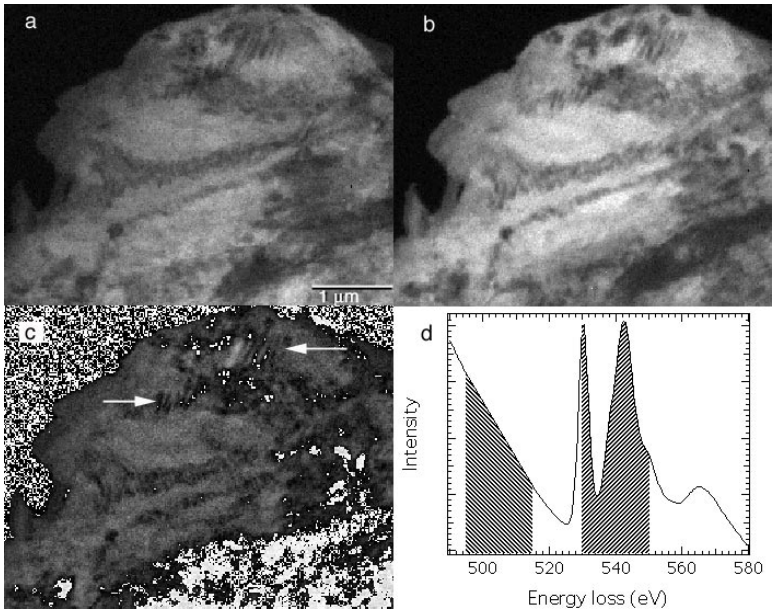

Figure 8.2: Chemical map of oxygen in Li_xCoO_2 using the oxygen K-edge. (**a**) Image taken using the spectrum window just before the edge. (**b**) Image taken using the spectrum window just after the edge. (**c**) Image (a) – image (b). (**d**) The oxygen K-edge demonstrating the different spectral windows. The arrows indicate possible oxygen deficient regions.

lack of contrast in Figure 8.2c suggests that the oxygen distribution in this material is

predominantly homogeneous. The arrows in the image indicate regions that appear to be oxygen deficient around a collection of Moiré fringes. The Moiré fringes are a disordered region of the sample where two planes have undergone a small relative rotation about the c-axis. It is possible that oxygen has evolved from this defective region. However, it is also likely that the strong diffraction contrast in this region may be responsible for the loss of intensity.

Energy-loss spectrometry and energy-filtered imaging may also be used to differentiate between lithium ions in the bulk and ions in grain boundaries. There are currently a number of questions concerning the possibility of reversible lithium storage in grain boundaries. One obvious step to resolve this issue is to produce chemical maps of lithium using the low-lying lithium K-edge. In addition to insights into the role of grain boundaries as diffusion pathways, a study of the grain boundaries in cycled electrodes may yield clues as to whether these regions contribute to the total lithium storage.

Valence mapping may also yield some insight into the distribution of valences within the material. This unique method of imaging is only possible because of the large lithium K-edge shifts observed in ionic lithium compounds (Figure 8.3a). In a recent investigation, the edge onset was found to scale linearly with the anion electronegativity (Figure 8.3). We believe an energy-filtered image with the lithium K-edge can be used to produce a

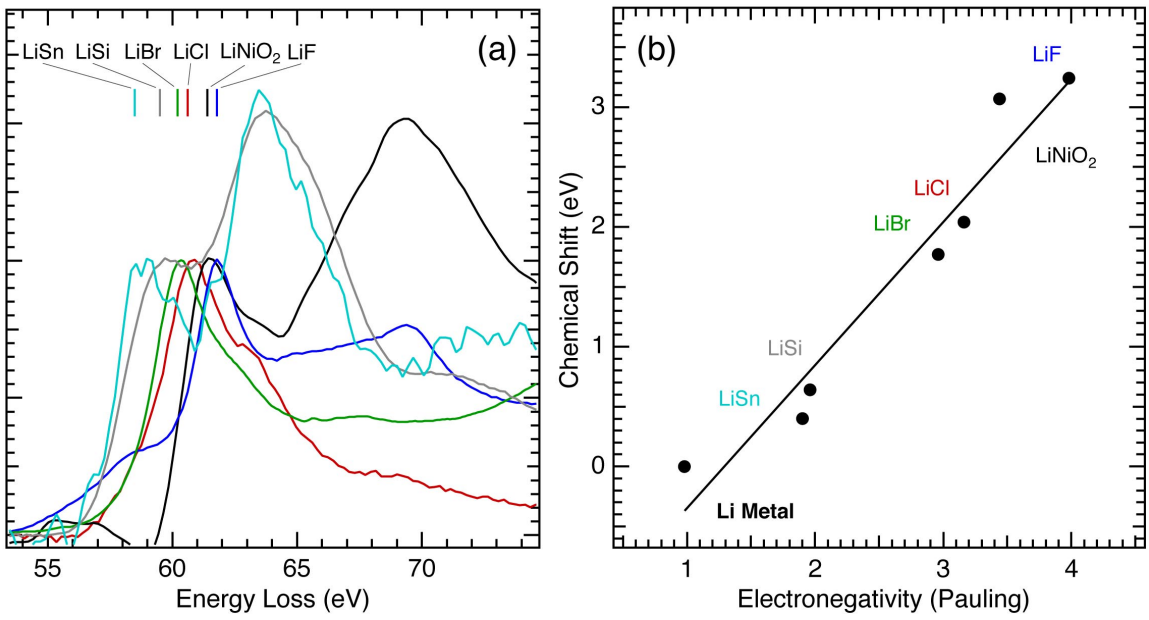

Figure 8.3: (**a**) The lithium K-edge from a series of binary lithium alloys and $LiNiO_2$. (**b**) Plot of the edge onset energy with Pauling electronegativity.

valence map of lithium ions in the electrode. This experiment will not only identify where the lithium is located, but will also distinguish between lithium ions at different chemical potentials, or different states of charge. An understanding of where the lithium resides and how it affects the electronic environments of the host is critical to the future development of lithium electrodes.

8.4 Thermodynamics

Recent thermodynamic studies of lithiation in layered cathodes have revealed surprising entropy changes in $LiCoO_2$ [120]. Thomas reports a large negative entropy of $-7k_B$/atom at $x \approx 0.8$ with a large increase in the entropy around $Li_{0.6}CoO_2$. Our temperature dependent electrochemical experiments on $LiCoO_2$ confirm these results.[1] The entropy was determined by measuring changes in the full cell potential with temperature, $d\epsilon/dT$. These measurements were performed at different lithium concentrations on both the charge and discharge cycles. A plot of the measured entropy from an electrochemical cell of $LiCoO_2$ versus lithium metal is displayed in Figure 8.4. The entropy maximum occurs around $Li_{0.6}CoO_2$ and is

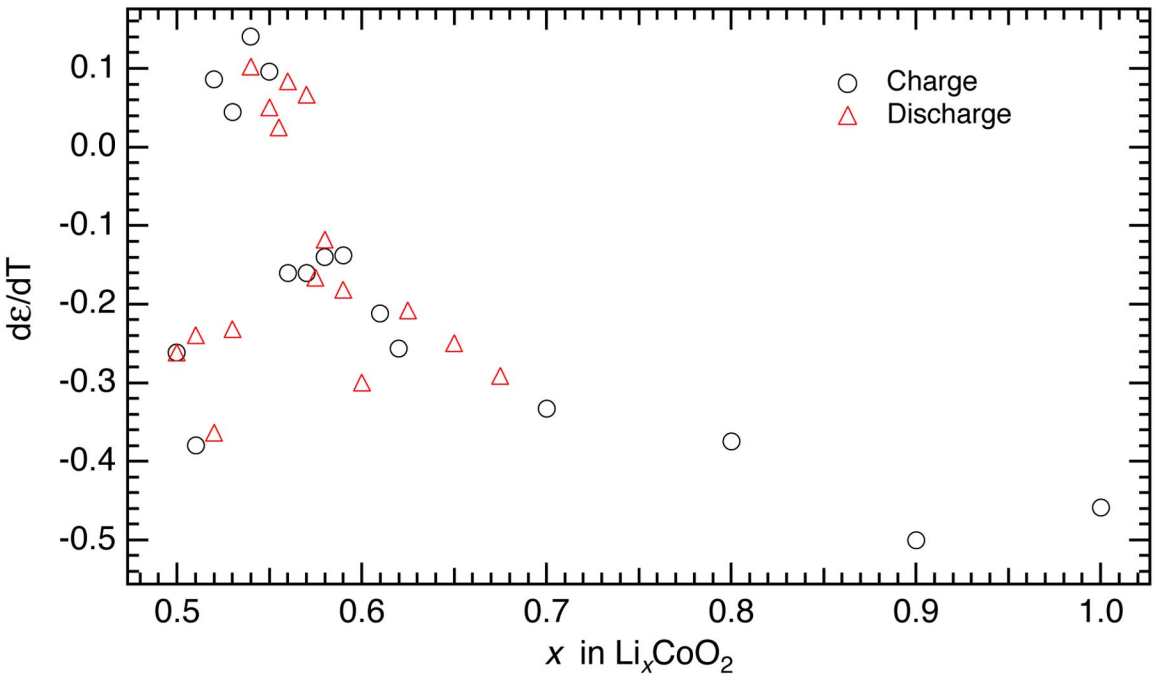

Figure 8.4: Entropy variations in $LiCoO_2$ during charge (○) and discharge (△) where x denotes the lithium concentration in Li_xCoO_2.

[1] Temperature-dependent studies of $LiCoO_2$ were performed by Yasunori Ozawa.

likely attributed to a first order phase transition (hexagonal to monoclinic). The most interesting region of Fig 8.4 is the large negative entropy values at higher lithium concentrations. As lithium is inserted into the host, the number of energetically equivalent sites decreases creating a decrease in the configurational entropy. However, the configurational contribution to the entropy is minimal at large lithium concentrations ($Li_{0.85}CoO_2$). It is speculated that the large negative entropy values may be attributed to a vibrational component of the entropy. To confirm these results, work has begun to experimentally measure the phonon density of states (DOS) in a series of delithiated compounds of $LiCoO_2$. The DOS will be extracted from inelastic thermal neutron scattering data acquired with a high-resolution chopper spectrometer (PHAROS) at the Los Alamos Neutron Science Center (LANSCE). The large changes in vibrational entropy predicted by the temperature dependent studies of lithiation should be easily visible in the phonon DOS of the delithiated material.

8.5 Kinetics

The kinetics of charging and discharging an electrochemical cell are typically limited by the solid-state diffusion of lithium. Recent interest in high-rate electrodes have inspired a number of investigations into the kinetics of lithium transport in nanostructured anode and cathode materials. Patrissi et al. have recently shown discharge rates as high as $4000C$ for a nanostructured V_2O_5 cathode [102]. The fast kinetics of lithium transport in nanoscale materials can in part be attributed to the large volume fraction of grain boundaries, which provide additional diffusion pathways and also have a lower activation barrier. However, the short diffusion distances in these materials are a more significant factor in improving the kinetics. The time, τ, for a lithium ion to diffuse a distance d through a material is $\tau = d^2/4D$, where D is diffusivity constant. Figure 8.5 displays a plot of the timescales required for lithium to diffuse through bulk germanium, silicon, $LiCoO_2$ and $LiNi_{1-x}Co_xO_2$ at 300 K. The diffusivities of lithium in $LiCoO_2$ and $LiNi_{1-x}Co_xO_2$ are 10^{-10} cm^2/s [121] and 5×10^{-10} cm^2/s [122], respectively. The diffusivities of lithium in germanium and silicon at room temperature are 1.8×10^{-14} cm^2/s and 7.7×10^{-12} cm^2/s, respectively (Chapter 7). Figure 8.5 shows that fast cycling rates can be achieved even in materials with low diffusivity, provided the diffusion lengths are short. The full lithiation of a 10 nm particle occurs 10,000 times faster than in a 1 μm particle. These results indicate that

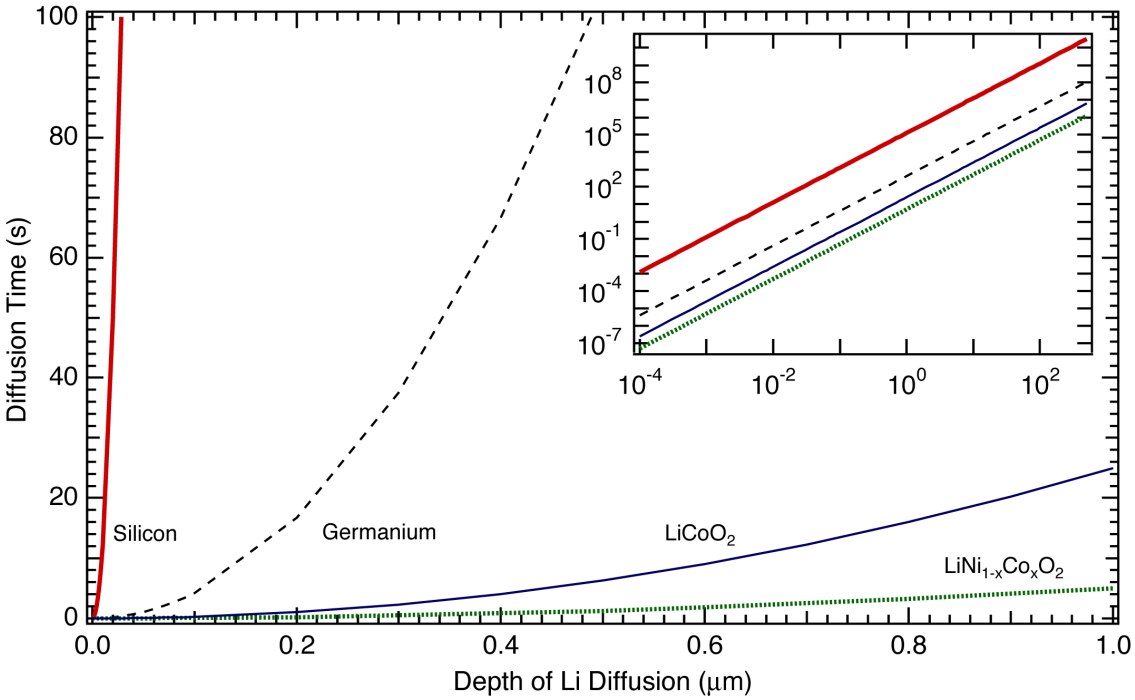

Figure 8.5: Timescales for lithium diffusion in bulk silicon, germanium, $LiCoO_2$ and $LiNi_{1-x}Co_xO_2$ at ambient temperature. The inset demonstrates the same relationship displayed logarithmically.

nanostructured (10–100 nm) cathodes of Li(Ni,Co)O_2 should cycle up to and beyond $4000C$ ($\sim$ 1 second charge/discharge). Similarly, nanophase lithium alloys will tolerate rates of at least $100C$ in germanium and a few C in silicon without a considerable reduction in cell capacity. The results of these simple calculations warrant additional electrochemical studies concerning the rate capabilities of nanostructured electrodes.

8.6 Mechanical Properties of Lithium Hosts

Despite the recent interest in nanostructured lithium electrodes, the underlying materials science behind the unique properties of these materials is still not well understood. Many of the current questions may be cleared up through an investigation of stress management and defects in nanostructured materials. Lithium electrodes often develop enormous strain gradients as a result of volume changes that occur during the absorption of lithium. The strain often leads to microstructural damage and eventually, a complete loss of capacity. Nanoscale materials are believed to be able to change dimensions quickly and uniformly, without developing large strain fields. An analysis of the local crystallographic structure

is necessary at different states of lithiation. X-ray micro-diffraction is well suited for these measurements. This experiment will provide a map of strain distributions on the micron scale and should allow us to better understand how stresses are managed in this system. A comprehensive study of strains and defects is necessary to determine if the microstructural damage is sufficiently mitigated in nanostructured electrodes to allow reversible cycling.

8.7 Technology

The development of new electrode materials for lithium rechargeable batteries will likely continue to have a profound technological impact in the future. Advances in thin film solid-state cells will allow for the miniaturization and the integration of the lithium cell with system electronics (e.g., "battery on a chip" [123, 124]). The resulting impact on microelectronics and wireless communications will lead to a number of improvements in existing technologies such as cellular phones, laptop computers, implantable medical devices, and hybrid-electric vehicles. Advances in lithium storage materials will also provide a catalyst for the adoption of new technologies.

Considerable improvements are also to be expected with purely electric vehicles. Although the electric vehicle is not a new concept, the commercialization of these automobiles has been severely limited by the progress of battery development. Electric vehicles are a demanding market, requiring a combination of high gravimetric and volumetric energy densities, high rate capabilities (high power), long life, complete safety even under extreme conditions, and a low production cost. However, the high energy and power densities available in lithium cells may provide the necessary impetus for the widespread conversion form the petroleum to the electric vehicle.

Appendix A Chemical Delithiation of $LiTMO_2$

A.1 Introduction

A number of $LiTMO_2$ cathodes were delithiated chemically for the experiments in this study. The general process involves mixing the cathode material in an aqueous solution of potassium persulfate ($K_2S_2O_8$). The amount of lithium extracted from the material was varied by altering the amount of oxidizing solution. The large chemical potential difference between lithium ions in the oxide and in the solution generates a strong thermodynamic driving force for the removal of lithium from the TMO_2 host. The reaction is halted when solution has reached equilibrium. This appendix presents the specific procedures involved in removing a fixed amount of lithium as well as a characterization of contaminants in the materials subsequent to delithiation.

A.2 Thermodynamics of Delithiation

The chemical delithiation process involves the following chemical reaction:

$$2LiCoO_2 + xK_2S_2O_8 \rightarrow 2Li_{1-x}CoO_2 + xK_2SO_4 + xLi_2SO_4, \tag{A.1}$$

which can be divided into the following subreactions:

$$LiCoO_2 \rightarrow Li^+ + CoO_2 + e^- \tag{A.2}$$

$$2e^- + S_2O_8 \rightarrow 2SO_4^{2-}. \tag{A.3}$$

The equilibrium lithium concentrations are determined through the thermodynamics involved in the reaction. The potential of each component of the reaction is given by the Nernst equation (Equation 1.8), which states that the full potential is the sum of the standard potential, ε^{00}, and the concentration energy:

$$\text{Reaction A.2}: \qquad \varepsilon_1^0 = \varepsilon_1^{00} + \frac{RT}{F}\log\left[\frac{4x^2}{1-x}\right] \tag{A.4}$$

$$\text{Reaction A.3}: \qquad \varepsilon_2^0 = \varepsilon_2^{00} + \frac{RT}{2F}\log\left[\frac{n_0 - x}{4x^2}\right], \tag{A.5}$$

where R is the universal gas constant, T is the reaction temperature, F is the Faraday constant, x is the amount of lithium removed, and n_0 is the molar ratio ($K_2S_2O_8/LiTMO_2$). The delithiation process is complete when the system has reached equilibrium and the two potentials are equivalent $\varepsilon_1^0 = \varepsilon_2^0$. Setting Equation A.4 equal to Equation A.5 yields an expression relating the molar ratio (amount of oxidizing material) to the amount of lithium removed from $LiTMO_2$:

$$n_0 = x + \left(\frac{4x^3}{1-x}\right)^2 \exp\left[\frac{\Delta\varepsilon F}{RT}\right]. \tag{A.6}$$

A more useful expression is the inverse of Equation A.6, which gives the amount of $LiTMO_2$ required to remove x lithium atoms:

$$\frac{n_{LiTMO_2}}{n_{K_2S_2O_8}} = \left(x + \left(\frac{4x^3}{1-x}\right)^2 K^2\right)^{-1}, \tag{A.7}$$

where the following substitution has been made:

$$K = \exp\left[\frac{\Delta\varepsilon F}{RT}\right]. \tag{A.8}$$

A plot of the relationship between the molar ratio (expressed in $LiTMO_2/K_2S_2O_8$) and the amount of lithium removed from the TMO_2 host is shown in Figure A.1. Samples of $LiCoO_2$, $LiNi_{0.8}Co_{0.2}O_2$, and $LiMn_2O_4$ are included in this plot.[1] Using a single fitting parameter, K, Equation A.7 was fit to the experimental data. The fit returned values for K of $0.0005 \leq K \leq 0.002$.

Although the fitting function of Figure A.1 has some physical meaning, it is clearly not the best fit to the data. A more useful plot is shown in Figure A.2, which identifies the relationship between the mass ratio (expressed in $LiTMO_2/K_2S_2O_8$) and the amount of lithium removed. The data in Figure A.2 were fit to an inverse square function, which provided the best overall fit:

$$\frac{M_{LiTMO_2}}{M_{K_2S_2O_8}} = f(x) = \alpha + \frac{\beta}{x^2}, \tag{A.9}$$

[1]Technically, these data do not belong on the same plot because the chemical potential of lithium is unique for each cathode. Therefore, the fitting function is a rough approximation and should only be used as a guide

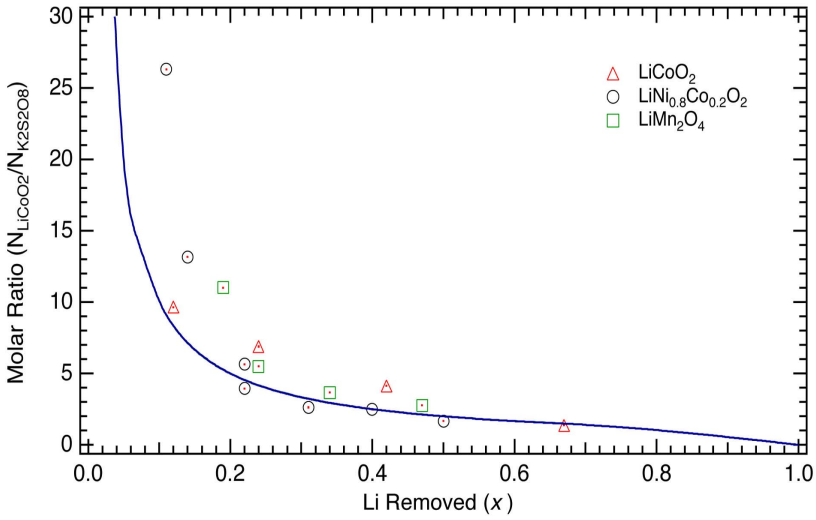

Figure A.1: Relationship between the molar ratio and the amount of lithium removed from various $LiTMO_2$. All of the data were fit using Equation A.7.

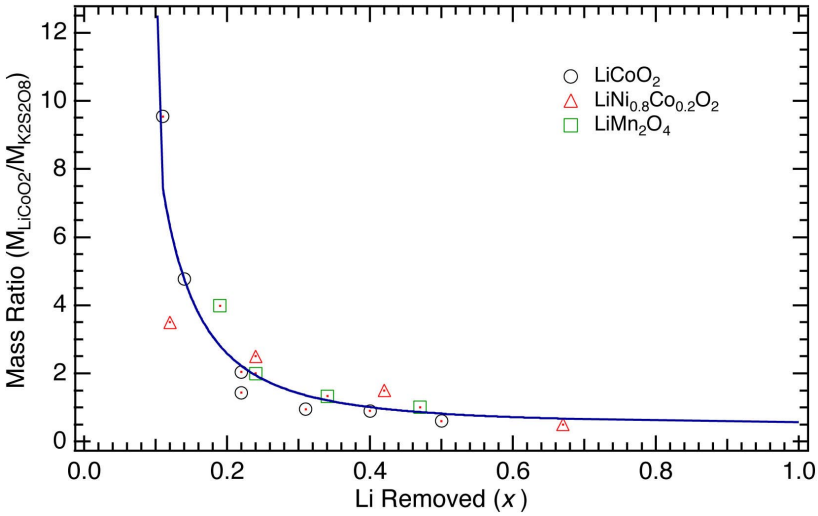

Figure A.2: Relationship between the mass ratio and the amount of lithium removed from various $LiTMO_2$. All of the data were fit using an inverse square function (Equation A.9).

where M is the mass of the material used in the reaction and α and β are fitting parameters ($\alpha = 0.48$ $\beta = 0.084$).

A.3 Delithiation Procedure

Given the delithiation characteristics above, the procedure for chemical delithiation is as follows:

1) Determine the mass ratio of $LiTMO_2/K_2S_2O_8$. This can be calculated using Equation A.9 with $\alpha = 0.48$ $\beta = 0.084$.

2) Mix $K_2S_2O_8$ in H_2O at a recommended ratio of 40 g $K_2S_2O_8$/1L H_2O. This ratio is not critical, however, $K_2S_2O_8$ does not dissolve well in water and trying to increase the

amount of oxidant may be difficult. Conversely, lowering this ratio will increase the total amount of solution. This will create difficulties in the agitation and washing stages.

3) To dissolve the $K_2S_2O_8$ in H_2O, the water should be heated to around 50° C. Add $K_2S_2O_8$ and agitate until the powder is completely dissolved. At 50° C this will take about an hour.[2]

4) Add the $LiTMO_2$ to the aqueous solution of potassium persulfate. Heat 50–60° C and agitate for $\sim$ 24 hours. The flask should be covered with waxed paper (or lightly plugged with a cork) to reduce the loss of solution from evaporation.

5) Filter and rinse with clean de-ionized H_2O. The solution can be filtered using a standard funnel and filter paper (or equivalent method capable of removing particles $\geq$ 1μm). Remove the powder from the filter and add the material to a flask of water and agitate for 15–30 min. This process of filtering and rinsing should be completed 2–3 times.

6) Remove the material from the filter and dry in vacuum (or air) at 50–60° C for 12–24 hours.

Although the delithiated samples may be structurally stable in air (at 300 K), they will likely absorb/adsorb H_2O and should therefore be kept in a dry atmosphere.

A.4 Characterization of Delithiated Material

Mass spectrometry and thermal gravimetric analysis (TGA) were used to determine the amount of residual H_2O, OH, and H in the chemically delithiated samples. Figure A.3 shows the TGA results from a series of $Li_{1-x}CoO_2$ that were delithiated using procedures above and dried in vacuum for 12 hours. In this experiment the temperature was raised at a rate of 10° C per minute. The fully lithiated material was found to be stable up to 500° C, whereas the delithiated samples evolved up to 4.5% of their original mass at temperatures of around 290° C. Mass spectrometry was used to characterize the evolved compounds. Figures A.4a–c show the mass spectrometry results for masses 2 (H_2), 18 (H_2O), and 32 (O_2). There is a simultaneous evolution of oxygen and water in the delithiated material at temperatures of around 300° C. The total mass evolved during the experiment scaled directly with the depth of delithiation, with a maximum of 4.5% in the most delithiated

[2]Heating $K_2S_2O_8$ will likely lead to some decomposition of the $K_2S_2O_8$ compound. This is probably the cause of much of the scatter in the data in Figures A.1–A.2. The loss of a little $K_2S_2O_8$ should not disturb the reaction but it will reduce the amount of lithium removed.

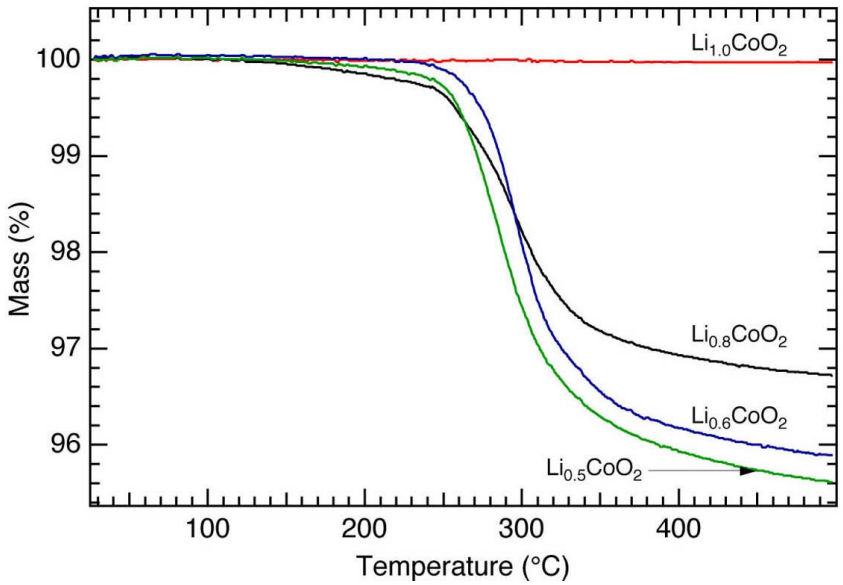

Figure A.3: TGA from delithiated $Li_{1-x}CoO_2$ showing a decrease in mass in the delithiated samples at 300° C.

sample. These results suggest that delithiated $LiTMO_2$, prepared in an aqueous solution, can be dried at ambient temperature to reduce the water contamination to less than 4.5%.

The evolution of water found in Figure A.4c suggests that the water contaminants can be eliminated completely if the drying temperature in step 6 were increased to 300° C. Although the removal of all of the water is possible at this temperature, the oxygen evolution (Fig A.4b), which also occurs at 300° C, is indicative of other changes occurring in the material. Recent results of Dahn et al. have shown that delithiated $LiCoO_2$ is thermally unstable [125]. Above 200° C the delithiated material undergoes the following transformation:

$$Li_xCoO_2 \rightarrow \frac{1-x}{3}Co_3O_4 + xLiCoO_2 + \frac{1-x}{3}O_2. \tag{A.10}$$

The delithiated material is decomposed into a spinel phase of Co_3O_4 and stoichiometric $LiCoO_2$. Therefore, any attempts to remove the excess water from the structure will not only create Co_3O_4 contaminants, but will also return the delithiated material to the more stable stoichiometric phase.

The thermal decomposition described by Dahn et al. was confirmed by our own diffraction analysis of thermally treated $Li_{1-x}CoO_2$ (Figure A.5). The delithiated $LiCoO_2$ shows a consistent shift in the (003) peak to lower 2θ angles with delithiation. This is due to the increase in the c lattice parameter that accompanies lithium extraction, and is described in more detail in Appendix B. The 300° C thermal treatment of the delithiated samples

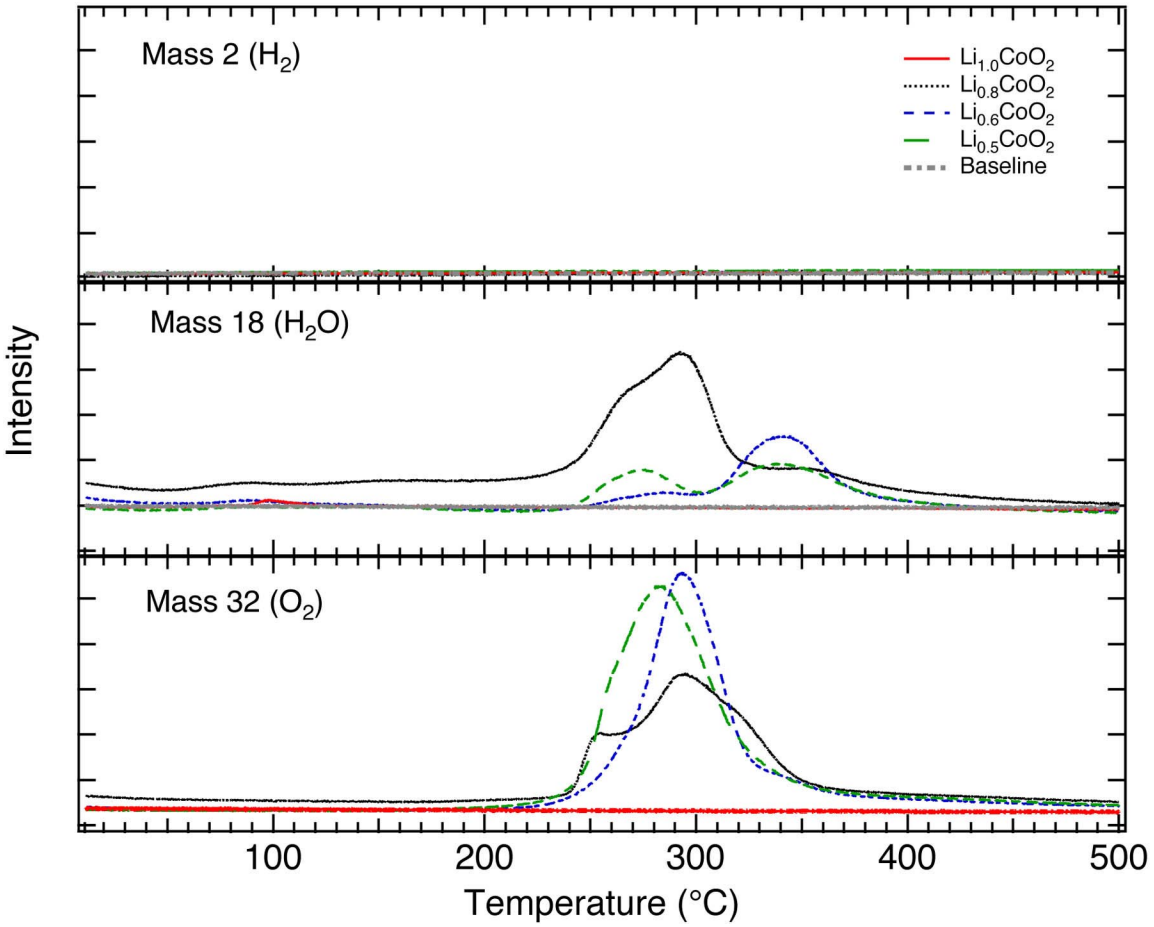

Figure A.4: Mass spectrometry from delithiated $Li_{1-x}CoO_2$ showing the evolution of (**a**) hydrogen, (**b**) water, and (**c**) oxygen at 300° C.

results in a shift of the (003) peak back to the fully lithiated position at $2\theta|_{CoK\alpha} = 21.45°$. This is consistent with the claim that the delithiated material returns to the stoichiometric phase during the heat treatment. The thermal decomposition reaction of Dahn et al. is further confirmed by the emergence of a (220) spinel peak ($2\theta = 36.5°$) that is indicative of the formation of Co_3O_4 (Figure A.5b).[3]

A.5 Alternative Methods

The water contamination in the delithiated material (less than 4.5%) is unavoidable when using an aqueous oxidizing solution. Contaminants may be reduced by using a nonaqueous

[3]The overlap of the Co_3O_4 and $LiCoO_2$ diffraction patterns makes it difficult to differentiate between the two compounds. The lowest unique peak is the Co_3O_4 (220), which has a low relative intensity. Co_3O_4 is therefore best identified using TEM where local regions of individual particles can be analyzed.

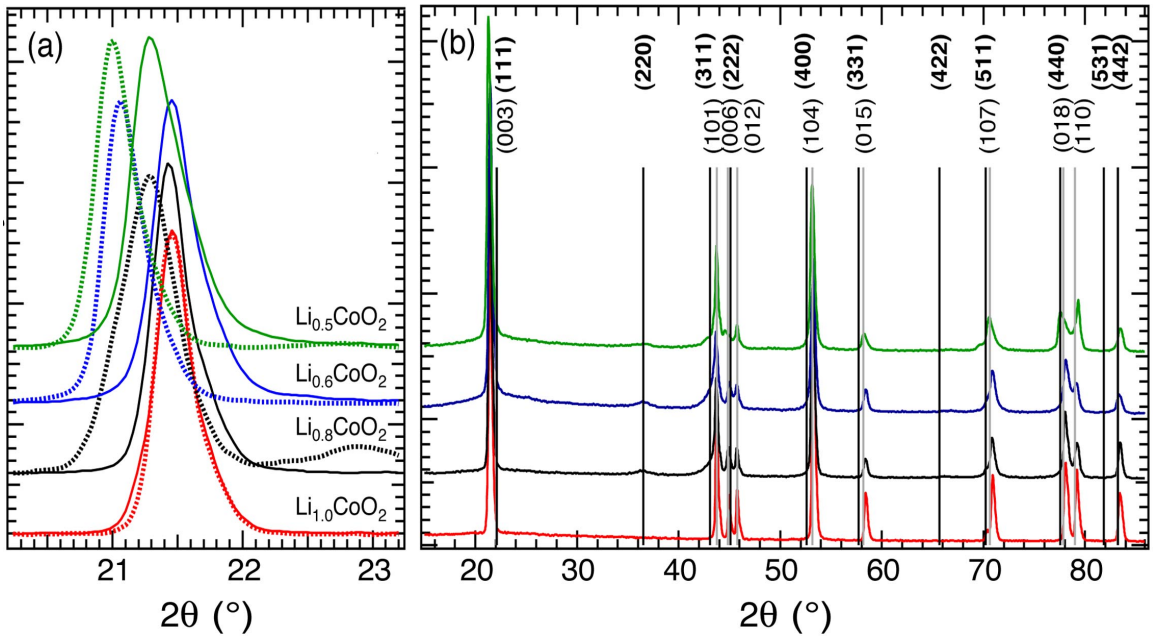

Figure A.5: X-ray diffraction patterns from $Li_{1-x}CoO_2$ showing (**a**) the shift of the (003) peak before (dotted) and after (solid) the thermal treatment. (**b**) The diffraction patterns of the delithiated material after thermal treatment, showing contributions from rhombohedral $LiCoO_2$ (hkl) and Co_3O_4 spinel (***hkl***).

solvent in the oxidizing solution. One method of nonaqueous chemical delithiation uses an oxidizer of NO_2PF_6 in a medium of acetonitrile in the following reaction [126, 127]:

$$LiTMO_2 + xNO_2PF_6 \rightarrow Li_{1-x}TMO_2 + xNO_2 + xLiPF_6. \tag{A.11}$$

This procedure must be carried out in a dry, inert atmosphere, and the final products should be washed in acetonitrile to remove $LiPF_6$. Using a nonaqueous oxidizing solution will eliminate the residual water in the samples, but may lead to other contaminants.

Another method for preparing "water-free" samples is through electrochemical delithiation. In this procedure an electrochemical cell is cycled a few times and then charged to a voltage[4] corresponding to the desired lithium concentration. This process has its own drawbacks in that the delithiated material will likely be contaminated with binders, conductive additives, and components of the electrolyte.

[4]To achieve the desired lithium concentration it is important to use the open circuit voltage after the cell has reached equilibrium.

Appendix B *In Situ* X-Ray Diffractometry

B.1 Introduction

In situ XRD of electrodes during electrochemical cycling is a relatively new but powerful technique for understanding the structural properties of electrode materials how they are affected by electrochemical cycling. *In situ* studies have been used to characterize structural changes in a number of different cathodes, revealing first and second-order phase changes [60, 128, 129]. The experiment described in this section is unique in that it identifies a new, inexpensive method for performing *in situ* XRD without the use of synchrotron radiation. The electrochemical cells were constructed using thin coin cells and the traditional beryllium window was replaced with a polymer window. By reducing the size of each component of the cell and eliminating extraneous strong scatterers, the diffracted intensity of the relevant material was sufficient to enable an *in situ* study using conventional cobalt $K\alpha$ radiation. In addition, replacing beryllium with an inexpensive nontoxic window considerably reduced the cost of assembling an *in situ* cell.

B.2 Experimental Methods

In situ cells were prepared by inserting an x-ray transparent window(s) into a conventional 2016 coin cell. The cells were constructed and tested in two different diffraction geometries, reflection and transmission. The most promising results were obtained for the transmission cells, so the procedures explained in this section will pertain solely to a transmission cell. The preparation of the electrochemical cell began with the removal of sections of the stainless steel on the anode and cathode cell casings. The window size was varied to obtain an optimal configuration while maintaining a working electrochemical cell. The optimal window size using a beam width of 0.5 mm was around 6 mm $\times$ 8 mm. The alignment of the cell in the center of the goniometer circle was progressively more difficult with the reduction of the window width. Kapton^{TM} was sealed over the opening in the cell casing and used as an x-ray window. The window was attached to the casing using a robust, high vacuum

sealant, Torr Seal^{TM} (Varian Instruments). Other adhesives, such as M-bond^{TM} (Micro-Measurements) and various other epoxies were also used with limited success. The strong solvents in the organic electrolyte used in these cells are easily able to decompose most resins and epoxies.

The insulating Kapton^{TM} and Torr Seal^{TM} completely destroys the continuity between the current collector (cell casing) and the region of the electrode covering the window. $LiCoO_2$ is a poor conductor (a semiconductor in the fully lithiated phase) and only the material in contact with the cell casing is electrochemically active during cycling. Therefore, a ~ 1 μm layer of aluminium was evaporated over the inside of the window on the cathode terminal.[1] The evaporated thin film of aluminum is reasonably transparent to x-rays, and the addition of this surface layer ensures a high conductivity across the current collector. The application of a conductive coating is unnecessary on the anode terminal because the metallic lithium is conductive and pressed into the cell casing.[2]

The cell was designed so that the dominant scattering was from the cathode ($LiCoO_2$), the material of interest. A schematic of the full *in situ* transmission cell is shown in Figure B.1. As the x-rays penetrate the cell they pass through the amorphous Kapton^{TM}

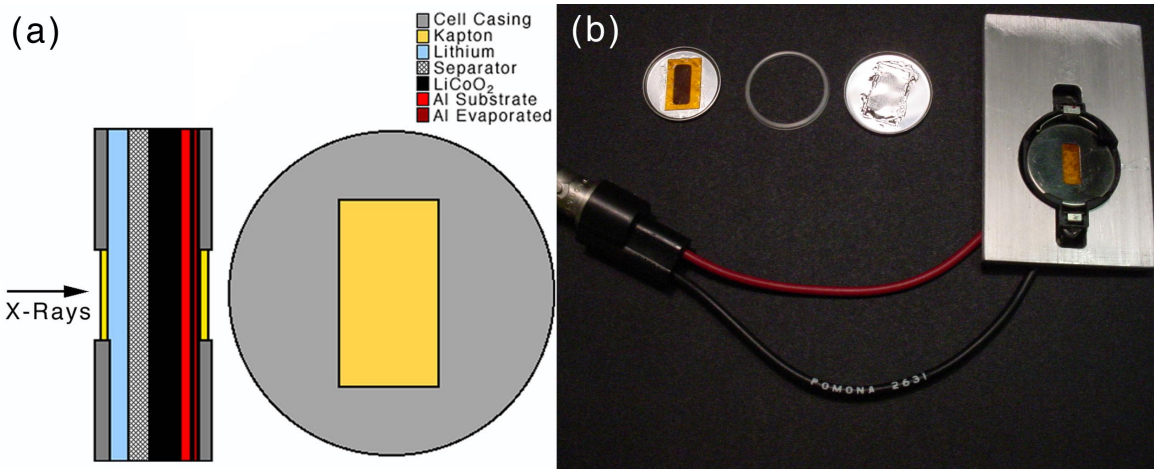

Figure B.1: (**a**) Schematic of *in situ* transmission cell and (**b**) an image of the cell components (left) and the custom cell holder (right).

window and thin aluminium layer, both of which are relatively x-ray transparent. The x-rays are scattered strongly by the cathode and are passed into the liquid electrolyte and

[1] In this case, the $LiCoO_2$ cathode is on an aluminium substrate so this step is probably not necessary, but was performed for consistency.

[2] Aluminium should not be used to coat the anode cell because it will alloy with the lithium forming Li_xAl.

a thin polyethylene separator. Before emerging from the cell, the x-rays traverse the metallic lithium anode and a Kapton^{TM} window. The Kapton^{TM}, separator, and the liquid electrolyte have a weak effect on the coherent x-ray scatterings and produce a diffuse background at low angles. The bcc lithium is a coherent scatterer, but the low atomic number of lithium provides only a weak contribution to the diffraction pattern.

An INEL CPS120 diffractometer and an Igor (Wavemetrics) data analysis package were modified to perform the *in situ* experiment. A custom cell holder and diffractometer sample holder were designed to accommodate a 2016 coin cell. The center of the cell window was aligned with the center of the goniometer circle. A lead beam stop was used to protect the detector from the transmitted beam. A photograph of the experimental setup (around the goniometer circle) is shown in Figure B.2. The data acquisition was performed with a

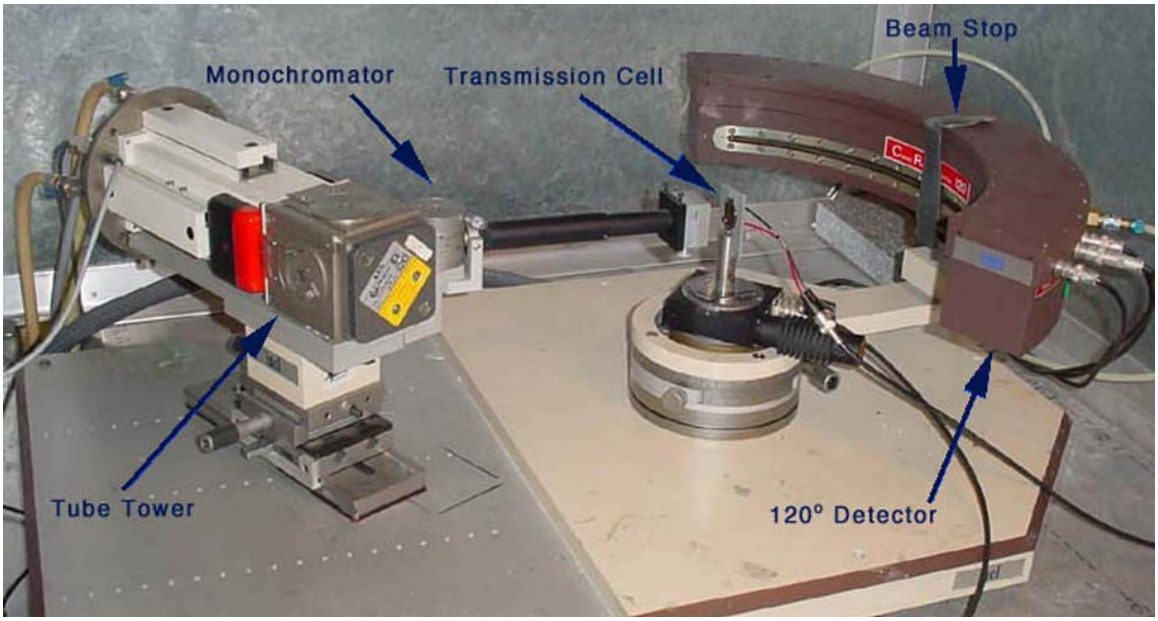

Figure B.2: Image of the experimental setup around the goniometer circle. The leads from the transmission cell were connected to the battery cycler.

software macro for the data analysis package Igor listed in Section B.4.1. The macro was programmed to acquire data in discrete intervals while a battery cycler (Arbin Instruments BT2000) charged and discharged the cell and recorded the cell voltage. In these experiments the cells were charged using a constant current. Since the cycling currents were low (10–15 mA/g), the diffraction patterns were acquired from an electrode close to equilibrium. To achieve a set of diffraction patterns from a fully equilibrated electrode, the cycler should

be programmed to include steps of constant voltage. In this experiment, the battery cycler was programmed to apply a constant current for a time, t_0. At a time, t, where $t > t_0$, the current was set to zero for a time, t_1. During this time, the potential, ϵ, slowly returns to its equilibrium value. The diffraction scan should be taken at the end of t_1 when the electrode is near equilibrium. Equilibrium is defined when the derivative of the potential is approximately zero ($\mathrm{d}\epsilon/\mathrm{d}t \approx 0$). The typical cathodes used in this study required a minimum of 1800 s to equilibrate.

B.3 Results

The *in situ* x-ray diffraction patterns of $LiCoO_2$ provide a direct measurement of changes in the lattice that occur as lithium ions are inserted and removed from the CoO_2 host. A cell composed of a $LiCoO_2$ cathode and a metallic lithium anode was prepared in the discharged state (fully lithiated $LiCoO_2$). X-ray diffraction scans were acquired *in situ* during electrochemical cycling. The cell was cycled up to 4.0 V on the first cycle and up to 4.1 V on the second cycle. In each cycle the cell was discharged to 2.8 V and all of the cycling was performed with a cell current of 11 mA/g ($C/14$). The full diffraction patterns

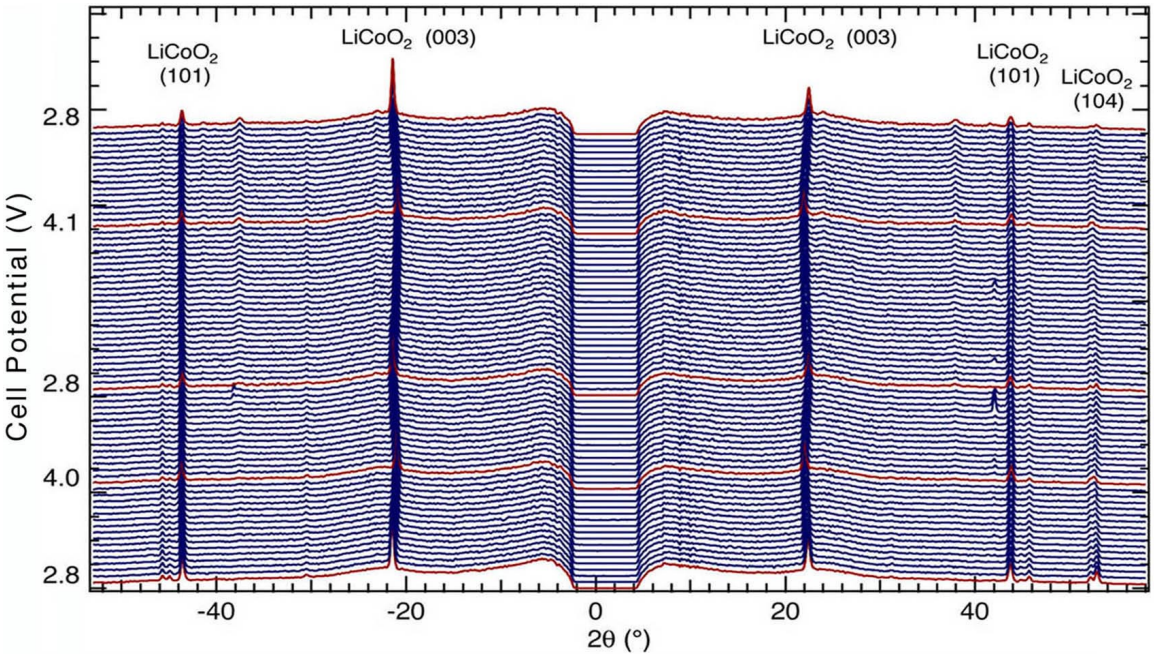

Figure B.3: Normalized transmission XRD pattern measured *in situ* while electrochemically cycling a cell of $LiCoO_2$ vs. lithium. The loss of intensity around $2\theta = 0°$ is due to a lead beam stop used to protect the detector from the transmitted beam.

from the transmission cell (Figure B.3) show the that the scattering is dominated by the $LiCoO_2$ cathode. Spectra were acquired on a 1800 s cycle with an acquisition time of 600 s and an idle time of 1200 s. The data were normalized by the integrated intensity over all detector elements (4096 channels). An Igor macro (Section B.4.2) was written to handle the normalization of the numerous data sets. In Figure B.3 the data are displayed with an intensity offset that scales with the scan number (or time at which the pattern was acquired). An Igor macro for inserting an intensity offset is displayed in Section B.4.3.

In the transmission configuration, the 120° detector captures intensity at $2\theta \leq 60°$. This configuration is well-suited for studying the low-order Bragg reflections since each peak is acquired in duplicate at different points on the detector. Folding the data about the origin, or simply averaging the two peaks, will reduce some of the inconsistencies due to detector aberrations.

The (003) Bragg peak was used to quantify changes in the lattice along the c direction in $LiCoO_2$. Figure B.4 shows a plot of the normalized (003) reflection during the two electrochemical cycles. The (003) Bragg reflection shifts to lower angles as the cell is charged,

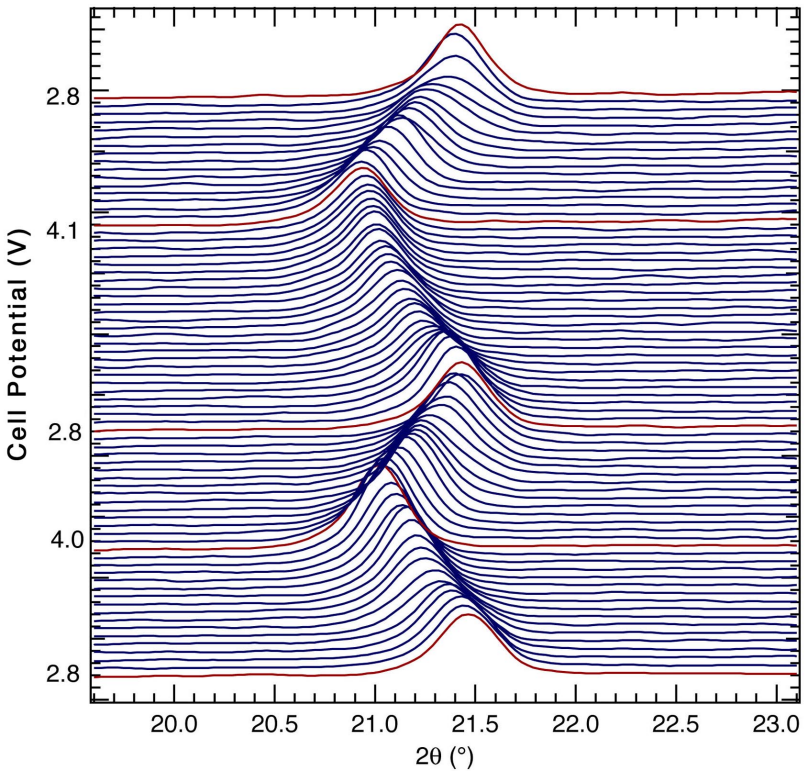

Figure B.4: (003) Bragg reflection measured *in situ* while electrochemically cycling a cell of $LiCoO_2$ vs. lithium.

which corresponds to the delithiation of the $LiCoO_2$ cathode. The peak shift is indicative of changes in the interplanar distance between the basal planes. To quantify the changes

that occur during electrochemical cycling, a Lorentzian function was fit to each Bragg peak using the Igor macro listed in Section B.4.4.

Figure B.5a shows the voltage profile over the two cycles for which approximately 70 scans were performed. Figure B.5b–c show the peak position and the peak width of the (003) diffraction for each scan. The position of the (003) diffraction appears to change

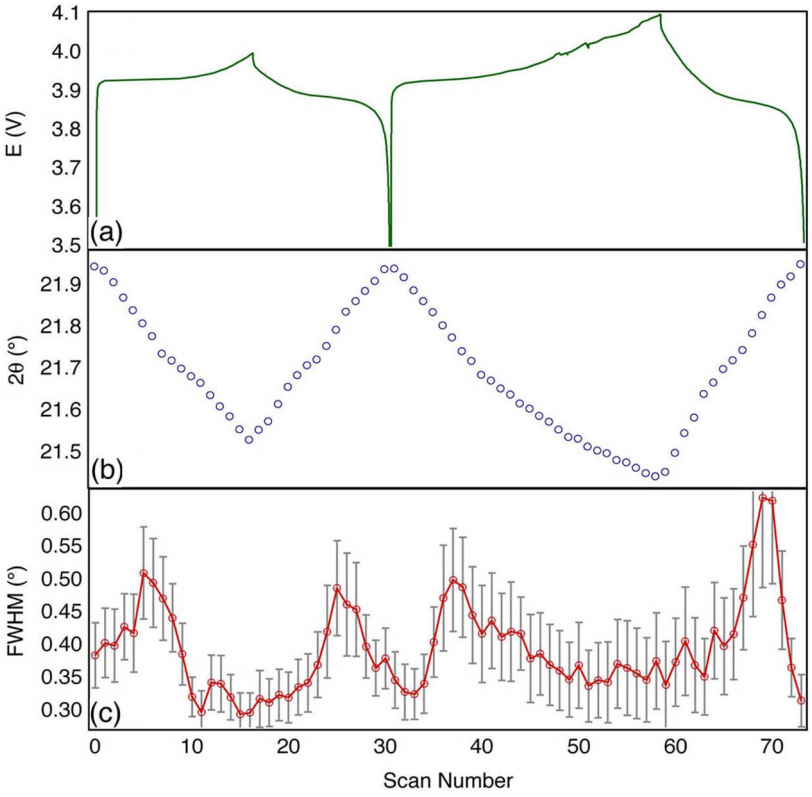

Figure B.5: (**a**) Full cell potential over two cycles. (**b**) Peak position and (**c**) the FWHM of the (003) diffraction measured *in situ* while cycling the cell.

linearly with the cell voltage, indicating a continuous change of the c lattice parameter during cycling.

The most salient feature of these plots is the change that occurs in the (003) peak width during lithium insertion/extraction (Fig B.5c). The full width at half-max (FWHM) is a measure of the mechanical strain in the lattice. The following expression for the strain, ε, is obtained by differentiating Bragg's Law ($2d\sin\theta = n\lambda$) with respect to the interplanar distance, d:

$$\varepsilon = -\frac{\Delta\theta}{\tan\theta}, \tag{B.1}$$

where $\Delta\theta$ is the FWHM ($\Delta 2\theta$ is the FWHM in a typical 2θ plot) and θ is the position of the Bragg reflection. Equation B.1 suggests that $\Delta\theta$ is directly proportional to the strain

in the lattice.[3] A sudden increase in the FWHM is apparent in Figure B.5c just before and just after the complete cell discharge. Each of these peaks occurs at a lithium concentration of $0.2 \leq x \leq 0.1$ in $Li_{1-x}CoO_2$. This behavior can easily be explained by the presence of a two-phase region at these lithium concentrations. Figure B.6 shows the phase diagram for $Li_{1-x}CoO_2$. The onset of a first-order phase transition occurs at $x = 0.93$. Two phases exist

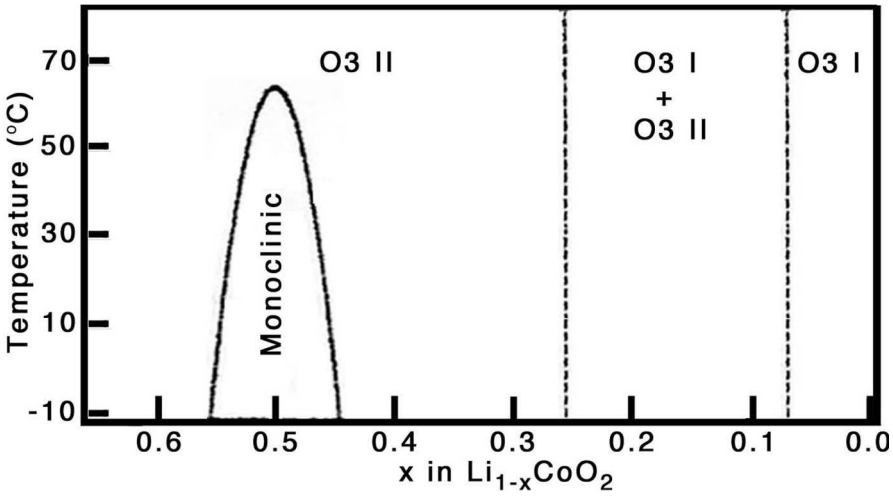

Figure B.6: Global phase diagram for $Li_{1-x}CoO_2$ showing the onset of a two phase region at $x = 0.93$ [60].

in the region $0.13 \leq x \leq 0.25$ and therefore two (003) Bragg reflections appear at slightly different angles in this coexistence region [60]. Since only a single Lorentzian was fit to the (003), the two-phase region becomes evident as an increase in the FWHM. Strain effects are greater at higher angles and therefore, higher-order peaks can be used to differentiate broadening from different sources (such as the appearance of a new peak or size broadening). An analysis of the (101) reflection did not show any broadening during lithium insertion or extraction. This is additional evidence suggesting that the peaks in Figure B.5c are not due to strain broadening, but rater due to the appearance of a new phase. To correctly quantify $\Delta 2\theta$ in this region, two Lorentzian functions should be used to fit to the two Bragg peaks.

Although the (003) peak depends only on the c lattice parameter, quantitative information concerning the a parameter can be extracted from other diffraction peaks, such as the (101). Figure B.7 shows the changes that occur in the a and c lattice parameters during electrochemical cycling. The removal of the positively-charged lithium ions from the host

[3]The FWHM ($\Delta\theta$) is also a function of the number of diffracting planes. However, the size dependence is independent of the diffraction vector, g. Therefore, extracting strain information from $\Delta\theta$ requires an analysis of peaks at different g, such as the (003) and the (006). The method of Warren and Averbach can also be used to determine simultaneous strain and size broadening [2]. However, these procedures are not practical with these data due to the low signal to noise ratio of the (006) diffraction and because the (006) diffraction overlaps with the (101) at low lithium concentrations ($x \leq 0.5$).

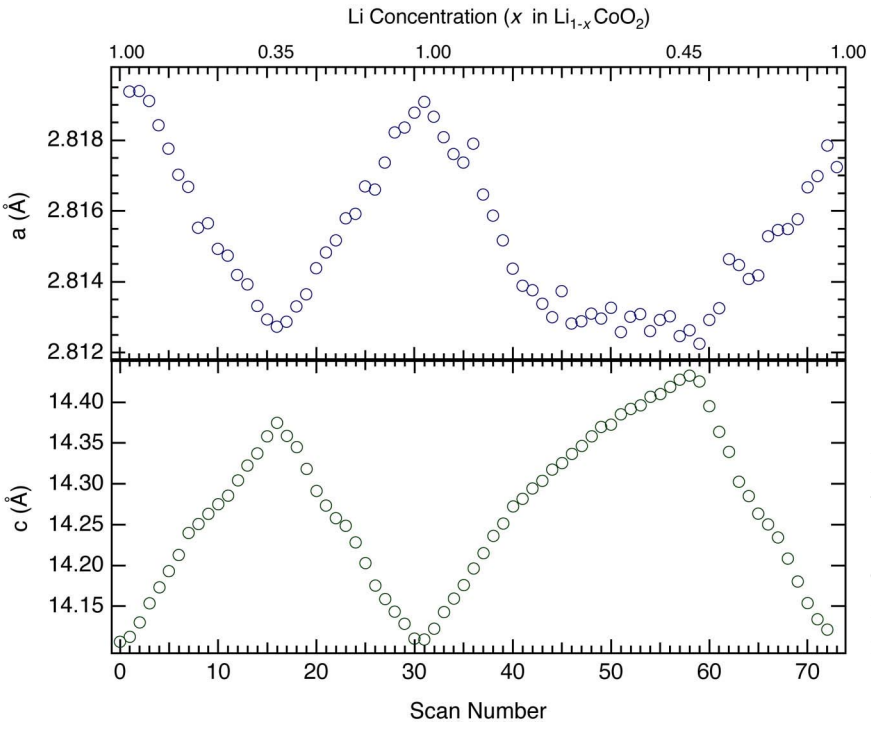

Figure B.7: Variations in the (**a**) a and (**b**) c lattice parameters during lithium insertion/extraction from the CoO_2 host.

reduces the screening between the oxygen planes. The coulomb repulsion of the oxygen layers causes the lattice to expand along the c-axis. An equivalent description is that the Li^+ ions provide an attractive "glue" in a Madelung summation. A smaller change is observed along the a direction where the interatomic distance within the basal plane decreases with the removal of lithium.

B.4 Acquisition and Data Reduction Software

B.4.1 Data Acquisition

This script acquires a diffraction pattern over a given time interval, *scantime*. Upon completion of a single diffraction scan, the wave is saved with a time stamp corresponding to the time when the acquisition began. The acquisition begins again after sleeping for a designated interval, *idletime*. These steps are repeated for a given time interval, *totaltime*, or until the macro is interrupted. The output is labeled by the wave name, *wavename*, and the time at which the scan began, *elapsetime* (*wavename_elapsetime*). The electrochemical cycling and data acquisition must be initiated simultaneously since the test time is the only parameter by which the two data sets can be correlated.

```
#pragma rtGlobals=1 // Use modern global access method.

Macro StartWindowInel(scantime, idletime, totaltime, wavename)

Variable scantime, idletime, totaltime // how long we take data during one data
set in seconds
String wavename

Variable elapsetime=0 //how much time our macro has run, in seconds
Do

MacInel clear 2
MacInel start 2
Sleep/S scantime
MacInel stop 2
MacInel get 2
Duplicate/O blueinel $(wavename+"_"+num2str(elapsetime))
Sleep/S idletime
elapsetime = elapsetime + scantime + idletime
while(elapsetime<totaltime)

EndMacro
```

B.4.2 Normalization

Although the diffraction patterns are acquired over an equivalent time interval, it may still be necessary to normalize the spectra. This script integrates each spectrum over 4096 channels (0–4095) and normalizes the spectra by the intensity of the initial scan (*wavename*_0). The input parameters are *scantime*, *idletime*, *totaltime*, and *wavename*. These values/names are used to reconstruct the name of each spectrum (*wavename_elapsetime*). To avoid overwriting the input wave, the output wave is labeled *wavename*_norm_*elapsetime*.

```
#pragma rtGlobals=1 // Use modern global access method.

Macro normalization(scantime, idletime, totaltime, wavename)
Variable totaltime, scantime, idletime
String wavename
Variable iter=0

Variable elapsetime=0 //how much time our macro has run, in seconds
Do
Duplicate/O $(wavename+"_"+num2str(elapsetime))
   $(wavename+"_"+num2str(elapsetime)+"_int")
Duplicate/O $(wavename+"_"+num2str(elapsetime))
   $(wavename+"_norm"+"_"+num2str(elapsetime))
integrate $(wavename+"_"+num2str(elapsetime)+"_int")
$(wavename+"_norm"+"_"+num2str(elapsetime))
   =($(wavename+"_0"+"_int")[4095]/$(wavename+"_"+num2str(elapsetime)+"_int")[4095])
   *$(wavename+"_"+num2str(elapsetime))

elapsetime = elapsetime + scantime + idletime

iter = iter +1

while(elapsetime<totaltime)

EndMacro
```

B.4.3 Offset

There are a number of ways to display the data and one simple method is to offset each diffraction pattern. The following procedure offsets each pattern by a given intensity. The input parameters *scantime*, *idletime*, *totaltime*, and *wavename* are used to reconstruct the name of each diffraction pattern (*wavename_elapsetime*). The value for the offset, *offset*, must also be given. To avoid overwriting the input wave, the output wave is labeled *wavename_elapsetime*_off.

```
#pragma rtGlobals=1 // Use modern global access method.

Macro offset(scantime, idletime, totaltime, offset, wavename)
Variable scantime, idletime, totaltime, offset
String wavename
Variable iter=0

Variable elapsetime=0 //how much time our macro has run, in seconds
Do
Duplicate/O $(wavename+"_"+num2str(elapsetime))
   $(wavename+"_"+num2str(elapsetime)+"_off")
   $(wavename+"_"+num2str(elapsetime)+"_off") += (offset*iter)

elapsetime = elapsetime + scantime + idletime
iter = iter +1
while(elapsetime < totaltime)

EndMacro
```

B.4.4 Peak Fits

Individual diffraction peaks were characterized by fitting to a Lorentzian function of the following form:

$$L(\theta) = L_0 + \frac{\alpha}{(2\theta - 2\theta_0)^2 + \beta}, \tag{B.2}$$

where L_0, α, $2\theta_0$, and β are fitting constants. The interesting peak information is given by the values of the peak position at the peak maximum, $2\theta_0$, the maximum peak intensity, $L_0 + \alpha/\beta$, and the full width at half-maximum, $\Delta 2\theta$, which is given by:

$$\Delta 2\theta = 2\left(\frac{2\alpha}{\alpha/\beta - L_0} - \beta\right)^{1/2}. \tag{B.3}$$

The following procedure file fits a single Lorentzian peak for each diffraction pattern in the series. The input values include the channel number of the first point to included in the fit (just below the peak), *startpoint*, and the total number of points to include in the fit, *totalpoints*. The initial point and total points are given in channel number (0–4095) not 2θ. In addition, the input parameters *scantime*, *idletime*, *totaltime*, and *wavename* are

used to reconstruct the name of each spectrum (*wavename_elapsetime*). This procedure creates a number of single column output waves of length equal to the number of spectra. The output waves are the peak maximum, $y0$, the peak position at the peak maximum, *twotheta*0, the error associated with the peak position, *twotheta*0_*error*, the full width at half-max, $fwhm$, the error associated with the full width at half-max, $fwhm\_error$, and the fitting constants, A and B. The error is calculated by including one standard deviation in the peak position and the FWHM.

```
#pragma rtGlobals=1 // Use modern global access method.

Macro LorentzianFit(scantime, idletime, totaltime, startpoint, totalpoints, wavename)
Variable scantime, idletime, totaltime, startpoint, totalpoints
   // startpoint and totalpoints are trimming values
   //choose startpoint just below peak and totalpoints to be number of
   points in peak
String wavename
Variable iter=0

Variable elapsetime=0 //how much time our macro has run, in seconds

//trim twotheta wave and rename as twotheta_trim
Duplicate/O twotheta twotheta_trim
DeletePoints 0, startpoint, twotheta_trim
DeletePoints totalpoints,4096, twotheta_trim

Make/N=(totaltime/(scantime+idletime))/D/O y0,A,twotheta0,B,
   fwhm,fwhm_error, twotheta0_error,imax //make waves for lorentzian
   coefficients

Do
Duplicate/O $(wavename+"_"+num2str(elapsetime))
   $(wavename+"_"+num2str(elapsetime)+"trim")

//trim wave about (003) peak
DeletePoints 0, startpoint, $(wavename+"_"+num2str(elapsetime)+"trim")
DeletePoints totalpoints,4096, $(wavename+"_"+num2str(elapsetime)+"trim")

//fit peak to lorentzian
CurveFit lor $(wavename+"_"+num2str(elapsetime)+"trim") /X=twotheta_trim /D

//insert coefficients into their respective waves
y0[iter]=W_coef[0]
A[iter]=W_coef[1]
twotheta0[iter]=W_coef[2]
twotheta0_error[iter]=W_sigma[2]
B[iter]=W_coef[3]
fwhm[iter]=2*SQRT(W_coef[1]/(W_coef[1]/(2*W_coef[3]))-W_coef[3])
fwhm_error[iter]=
   2*SQRT(2*(W_coef[1]+W_sigma[1])/((W_coef[1]-W_sigma[1])/(W_coef[3]
   +W_sigma[3])-(W_coef[0]+W_sigma[0]))-(W_coef[3]-W_sigma[3]))-fwhm[iter]
imax[iter]=W_coef[1]/W_coef[3]
elapsetime = elapsetime + scantime + idletime

iter = iter +1

while(elapsetime<totaltime)

EndMacro
```

Bibliography

[1] R. A. Huggins. Binary Electrodes under equilibrium or near-equilibrium conditions. In C. Julien and Z. Stoynov, editors, *Materials for Lithium-Ion Batteries*, pages 47–74. Kluwer Academic Publishers, 2000.

[2] B. Fultz and J. Howe. *Transmission Electron Microscopy and Diffractometry of Materials*. Springer-Verlag, New York, 2000.

[3] D. M. Sherman. The Electronic-Structures of Manganese Oxide Minerals. *Am. Mineralogist*, 69:788–799, 1984.

[4] T. G. Sparrow, B. G. Williams, C. N. R. Rao, and J. M. Thomas. L3/L2 White-Line Intensity Ratio in the Electron Energy-Loss Spectra of 3d Transition-Metal Oxides. *Chem. Phys. Lett.*, 108:547–550, 1984.

[5] C. C. Ahn and O. L. Krivanek. *EELS Atlas*. 1983. Copies ($US15) from Center for Solid State Science, Arizona State University, Tempe, AZ 85287, or from Gatan Inc., 780 Commonwealth Dr., Warrendale, PA 15086.

[6] J. Yamaki and S. Tobishima. Rechargeable Lithium Anodes. In Jurgen O. Besenhard, editor, *Handbook of Battery Materials*, pages 339–357. WILEY-VCH, New York, 1999.

[7] B. Scrosati. Insertion Compounds for Lithium Rocking Chair Batteries. In Jacek Lipkowski and Philip N. Ross, editors, *Electrochemistry of Novel Materials*, pages 111–140. VCH, 1994.

[8] E. Plichta, S. Slane, M. Uchiyama, M. Salomon, D. Chua, W. B. Ebner, and H. W. Lin. An Improved Li/Li_xCoO_2 Rechargeable Cell. *J. Electrochem. Soc.*, 136:1865–1869, 1989.

[9] M. G. S. R. Thomas, W. I. F. David, J. B. Goodenough, and P. Groves. Synthesis and Structural Characterization of the Normal Spinel Li[Ni_2]O_4. *Mat. Res. Bull.*, 20:1137–1146, 1985.

[10] C. Delmas and I. Saadoune. Electrochemical and Physical Properties of the $Li_xNi_{1-y}Co_yO_2$ phases. *Solid State Ionics*, pages 370–375, 1992.

[11] L. A. de Picciotto, M. M. Thackeray, W. I. F. David, P. G. Bruce, and J. B. Goodenough. Structural Characterization of Delithiated $LiVO_2$. *Mat. Res. Bull.*, 19:1497–1506, 1984.

[12] P. P. Prosini, D. Zane, and M. Pasquali. Improved Electrochemical Performance of a $LiFePO_4$- Based Composite Cathode. *Electrochim. Acta*, 46(23):3517–3523, 2001.

[13] M. M. Thackeray, P. J. Johnson, L. A. dePicciotto, P. G. Bruce, and J. B. Goodenough. Electrochemical Extraction of Lithium from $LiMn_2O_4$. *Mat. Res. Bull.*, 19:179–187, 1984.

[14] J. M. Tarascon, E. Wang, F. K. Shokoohi, W. R. McKinnon, and S. Colson. The Spinel Phase of $LiMn_2O_4$ As a Cathode in Secondary Lithium Cells. *J. Elecrtrochem. Soc.*, 138:2859–2864, 1991.

[15] T. Ohzuku and A. Ueda. Why Transition-Metal (Di) Oxides are the Most Attractive Materials for Batteries. *Solid State Ionics*, 69:201–211, 1994.

[16] W. D. Johnston, R. R. Heikes, and D. Sestrich. The Preparation, Crystallography, and Magnetic Properties of the $Li_xCo_{(1-x)}O$ System. *J. Phys. Chem. Solids*, 7:1–13, 1958.

[17] H. J. Orman and P. J. Wiseman. Cobalt(III) Lithium Oxide, $CoLiO_2$: Structure Refinement by Powder Neutron Diffraction. *Acta Cryst.*, C40:12–14, 1984.

[18] A. Rougier and C. Delmas. Non-Cooperative Jahn-Teller Effect in $LiNiO_2$: An EXAFS Study. *Solid State Comm.*, 94:123–127, 1995.

[19] A. K. Padhi, K. S. Nanjundaswamy, and J. B. Goodenough. Phospho-Olivines As Positive-Electrode Materials For Rechargeable Lithium Batteries. *J. Electrochem. Soc.*, 144:1188–1194, 1997.

[20] S. Y. Chung, J. T. Bloking, and Chiang Y. M. Electronically Conductive Phospho-Olivines As Lithium Storage Electrodes. *Nature Materials*, pages 123–128, 2002.

[21] F. Croce, A.D. Epifanio, J. Hassoun, A. Deptula, T. Olczac, and B. Scrosati. A Novel Concept for the Synthesis of an Improved $LiFePO_4$ Lithium Battery Cathode. *Electrochem. Solid State Lett.*, 5:A47–A50, 2002.

[22] Z. H. Chen and J. R. Dahn. Reducing Carbon in $LiFePO_4$/C Composite Electrodes to Maximize Specific Energy, Volumetric Energy, and Tap Density. *J. Electrochem. Soc.*, 149(9):A1184–A1189, 2002.

[23] S. Okada, S. Sawa, M. Egashira, J. Yamaki, M. Tabuchi, H. Kageyama, T. Konishi, and A. Yoshino. Cathode Properties of Phospho-Olivine $LiMPO_4$ for Lithium Secondary Batteries. *J. Power Sources*, 97-8:430–432, 2001.

[24] R. Yazami and Touzain P. H. A Reversible Graphite-Lithium Negative Electrode For Electrochemical Generators. *J. Power Sources*, 9:365–371, 1983.

[25] R. F. Egerton. *Electron Energy Loss Spectrometry in the Electron Microscope*. Plenum Press, New York, 1986.

[26] D. J. Griffiths. *Introduction to Quantum Mechanics*. Prentice-Hall, Englewood Cliffs, 1995.

[27] H. Shuman and K. Kruit. Quantitative Data Processing of Parallel Recorded Electron Energy-Loss Spectra with Low Signal to Background. *Rev. Sci. Instrum.)*, 56:231–239, 1985.

[28] D. W. Johnson and J. C. H. Spence. Determination of Single-Scattering Probability Distribution From Plural-Scattering Data. *J. Phys. D (Appl. Phys.)*, 7:771–780, 1974.

[29] M. Ruhle, J. Mayer, J. C. H. Spence, J. Bihr, W. Probst, and E. Weimer. Electron Spectroscopic Imaging and Diffraction. In G. W. Bailey and E. L. Hall, editors, *Proc. 49th Ann. Meet. Electron Microscopy Soc. Amer.*, pages 706–707, 1991.

[30] Z. L. Wang and A. J. Shapiro. Energy-Filtering and Composition-Sensitive Imaging in Surface and Interface Studies Using HREM. *Ultramicroscopy*, 60:115–135, 1995.

[31] Z. L. Wang, J. Bentley, and N. D. Evans. Mapping the Valence States of transition-Metal Elements Using Energy-Filtered Transmission Electron Microscopy. *J. Phys. Chem. B*, 103(5):751–753, 1999.

[32] Z. L. Wang, J. Bentley, and N. D. Evans. Valence State Mapping of Cobalt and Manganese Using Near-Edge Fine Structures. *Micron.*, 31(4):355–362, 2000.

[33] M. T. Otten, B. Miner, J. H. Rask, and P. R. Buseck. The Determination of Ti, Mn and Fe Oxidation States in Minerals by Electron Energy Loss Spectroscopy. *Ultramicroscopy*, 18:285–290, 1985.

[34] O. L. Krivanek and J. H. Paterson. ELNES of 3d Transition-Metal Oxides I. Variations Across the Periodic Table. *Ultramicroscopy*, 32:313–318, 1990.

[35] J. H. Paterson and O. L. Krivanek. ELNES of 3d Transition-Metal Oxides II. Variations with Oxidation State and Crystal Structure. *Ultramicroscopy*, 32:319–325, 1990.

[36] H. Kurata, E. Lefevre, C. Colliex, and R. Brydson. Electron-Energy-Loss Near-Edge Structures in the Oxygen K-Edge Spectra of Transition-Metal Oxides. *Phys. Rev. B*, 47:13763–13768, 1993.

[37] F. M. F. DeGroot, M. Grioni, J. C. Fuggle, J. Ghijsen, G. A. Sawatzky, and H. Peterson. Oxygen 1s X-Ray-Absorption Edges of Transition-Metal Oxides. *Phys. Rev. B*, 40:5715–5723, 1989.

[38] H. Kurata and C. Colliex. Electron-Energy-Loss Core-Edge Structures in Manganese Oxides. *Phys. Rev. B*, 48:2102–2108, 1993.

[39] D. D. Vvedensky and J. B. Pendy. Experimental-Study of Multiple-Scattering in X-Ray-Absorption Near-Edge Structure - Comment. *Phys. Rev. Lett.*, 54:2725, 1985.

[40] P. Rez, X. Weng, and H. Ma. The Interpretation of Near Edge Structure. *Microsc. Microanal. Microstruct.*, 2:143–151, 1991.

[41] P. Kuiper, G. Kruizinga, J. Ghijsen, and G. A. Sawatzky. Character of Holes in $Li_xNi_{1-x}O$ and their Magnetic Behavior. *Phys. Rev. Lett.*, 62:221–224, 1989.

[42] M. Pedio, J. C. Fuggle, J. Somers, E. Umbach, J. Haase, Th. Linder, U. Hofer, M. Grioni, F. M. F. de Groot, B. Hillert, L. Becker, and A. Robinson. Covalency in Oxygen Chemisorption As Probed by X-Ray Absorption. *Phys. Rev. B*, 40:7924–7927, 1989.

[43] A. F. Starace. Potential-Barrier Effects in Photoabsorption. I. General Theory. *Phys. Rev. B*, 5:1773–1784, 1972.

[44] J. A. Horsley. Relationship Between the Area of L2,3 X-Ray Absorption-Edge Resonances and the d Orbital Occupancy in Compounds of Platinum and Iridium. *J. Chem. Phys.*, 76:1451–1458, 1982.

[45] C. N. R. Rao, J. M. Thomas, B. G. Williams, and T. G. Sparrow. Determination of the Number of d-Electron States in Transition-Metal Compounds. *J. Phys. Chem.*, 88:5769–5770, 1984.

[46] D. H. Pearson, B. Fultz, and C. C. Ahn. Measurements of 3d State Occupancy in Transition Metals Using Electron Energy Loss Spectrometry. *Appl. Phys. Lett.*, 53:1405–1407, 1988.

[47] D. H. Pearson, C. C. Ahn, and B. Fultz. White lines and d-Electron Occupancies for the 3d and 4d Transition Metals. *Phys. Rev. B*, 47:8471–8478, 1992.

[48] L. A. Montoro, M. Abbate, and J. M. Rosolen. Electronic Structure of Transition Metal Ions in Deintercalated and Reintercalated $LiCo_{0.5}Ni_{0.5}O_2$. *J. Electrochem. Soc.*, 147:1651–1657, 2000.

[49] R. D. Leapman, L. A. Grunes, and P. L. Fejes. Study of the L23 Edges in the 3d Transition Metals and their Oxides by Electron-Energy-Loss Spectroscopy with Comparisons to Theory. *Phys. Rev. B*, 26:614–635, 1982.

[50] R. D. Leapman and L. A. Grunes. Anomalous L3-L2 White-Line Ratios in the 3d Transition-Metals. *Phys. Rev. Lett.*, 45:397–401, 1980.

[51] B. T. Thole and G. VanDerLann. Branching Ratio in X-Ray Absorption-Spectroscopy. *Phys. Rev. B*, 38:3158–3171, 1988.

[52] G. Wendin. Photoionization of Metallic Lanthanum, Thorium, and Uranium in a Local-Density-Based Random-Phase Approximation. *Phys. Rev. Lett.*, 53(7):724–727, 1984.

[53] B. T. Thole, G. VanderLaan, J. C. Fuggle, G. A. Sawatzky, R. C. Karnatak, and J. M. Esteva. 3d X-Ray-Absorption Lines and the 3D94FN+1 Multiplets of the Lanthanides. *Phys. Rev. B*, 32:5107–5118, 1985.

[54] M. K. Aydinol, A. F. Kohan, G. Ceder, K. Cho, and J. Joannopoulos. Ab Initio Study of Lithium Intercalation in Metal Oxides and Metal Dichalcogenides. *Phys. Rev. B*, 56:1354–1365, 1997.

[55] G. Ceder, A. Van der Ven, C. Marianetti, and D. Morgan. First-Principles Alloy Theory in Oxides. *Modell. Simul. Mater. Sci. Eng.*, 8:311–321, 2000.

[56] J. VanElp, J. L. Wieland, H. Eskes, P. Kuiper, G. A. Sawatzky, F. M. F. DeGroot, and T. S. Turner. Electronic-Structure of CoO, Li-Doped CoO, and $LiCoO_2$. *Phys. Rev. B*, 44:6090–6103, 1991.

[57] L. A. Montoro, M. Abbate, and J. M. Rosolen. Changes in the Electronic Structure of Chemically Deintercalated $LiCoO_2$. *Electrochem. Solid State Lett.*, 3:410–412, 2000.

[58] T. Ohzuku and A. Ueda. Solid-State Redgox Reactions of $LiCoO_2$ (R(3)Over- Bar-M) for 4 Volt Secondary Lithium Cells. *J. Electrochem. Soc.*, 141:2972–2977, 1994.

[59] M. G. Kim and C. H. Yo. X-ray absorption spectroscopic study of chemically and electrochemically Li ion extracted $Li_0yCo_{0.85}Al_{0.15}O_2$ compounds. *J. Phys. Chem. B*, 103:6457–6465, 1999.

[60] J. N. Reimers and J. R. Dahn. Electrochemical and In Situ X-Ray-Diffraction Studies of Lithium Intercalation in Li_xCoO_2. *J. Electrochem. Soc.*, 139:2091–2097, 1992.

[61] G. Kresse and J. Hafner. Ab Initio Molecular-Dynamics for Liquid-Metals. *Phys. Rev. B*, 47:558–561, 1993.

[62] G. Kresse and J. Furthmuller. Efficient Iterative Schemes for Ab Initio Total- Energy Calculations Using a Plane-Wave Basis Set. *Phys. Rev. B*, 54:11169–11186, 1996.

[63] G. Kresse and J. Furthmuller. Efficiency of Ab Initio Total Energy Calculations for Metals and Semiconductors Using a Plane-Wave Basis Set. *J. Comput. Mater. Sci.*, 6:15–50, 1996.

[64] A. Van der Ven, M. K. Aydinol, G. Ceder, G. Kresse, and J. Hafner. First-Principles Investigation of Phase Stability in Li_xCoO_2. *Phys. Rev. B*, 58:2975–2987, 1998.

[65] M. Methfessel and A. T. Paxton. High-Precision Sampling for Billouin-Zone Integration in Metals. *Phys. Rev. B*, 40:3616–3621, 1989.

[66] R. D. Leapman, P. Rez, and D. F. Mayers. K-Shell, L-Shell AND M-Shell Generalized Oscillator-Strengths and Ionization Cross Sections for Fast Electron Collisions. *J. Chem. Phys.*, 72:1232–1243, 1980.

[67] P. Rez. Electron Ionization Cross Sections for K-Shell, L-Shell, and M-Shell. *X-Ray Spectrom.*, 13:55–59, 1984.

[68] F. M. F. DeGroot, M. Abbate, J. VanElp, G. A. Sawatzky, Y. J. Ma, C. T. Chen, and F. Sette. Oxygen-1s and Cobalt-2p X-Ray Absorption of Cobalt Oxides. *J. Phys. Condens. Matter*, 5:2277–2288, 1993.

[69] C. Wolverton and A. Zunger. First-Principles Prediction of Vacancy Order-Disorder and Intercalation Battery Voltages in Li_xCoO_2. *Phys. Rev. Lett.*, 81:606–609, 1998.

[70] I. Saadoune and C. J. Delmas. On the $Li_xNi_{0.8}Co_{0.2}O_2$ System. *Solid State Chem.*, 136:8–15, 1998.

[71] M. Balasubramanian, X. Sun, X. Q. Yang, and J. McBreen. In Situ X-ray Absorption studies of a High-Rate $LiNi_{0.85}Co_{0.15}O_2$ Cathode Material. *J. Electrochem. Soc.*, 147:2903–2909, 2000.

[72] A. N. Mansour, J. McBreen, and C. A. Melendres. An In Situ X-ray absorption Spectroscopic Study of Charged $Li_{(1-z)}Ni_{(1+z)}O_2$ Cathode Material. *J. Electrochem. Soc.*, 146:2799–2809, 1999.

[73] A. N. Mansour, L. Croguennec, G. Prado, and C. J. Delmas. In Situ XAS Study of $Li_xNi_{0.7}Fe_{0.15}Co_{0.15}O_2$ Cathode Material. *Synchrotron Rad.*, 8:866–868, 2001.

[74] A. N. Mansour, X. Q. Yang, X. Sun, J. McBreen, L. Croguennec, and C. Delmas. In Situ X-ray Absorption Spectroscopic Study of $Li_{(1-z)}Ni_{(1+z)}O_2$ ($z \leq 0.02$) Cathode Material. *J. Electrochem. Soc.*, 147:2104–2109, 2000.

[75] I. Nakai, K. Takahashi, Y. Shiraishi, and T. Nakagome. XAFS Characteristics of Li Deintercalation in Rechargeable Lithium Battery Materials, $LiCoO_2$-$LiNiO_2$. *J. Phys. IV France*, 7:C2–1243–1244, 1997.

[76] I. Nakai, K. Takahashi, Y. Shiraishi, T. J. Nakagome, F. Izumi, Y. Ishii, F. Nishikawa, and T. J. Konishi. X-Ray Absorption Fine Structure and Neutron Diffraction Analyses of De-Intercalation Behavior in the $LiCoO_2$ and $LiNiO_2$ Systems. *Power Sources*, 68:536–539, 1997.

[77] I. Nakai and T. J. Nakagome. In Situ Transmission X-Ray Absorption Fine Structure Analysis of the Li Deintercalation Process in $Li(Ni_{0.5}Co_{0.5})O_2$. *Electrochem. Solid-State Lett.*, 1:259–261, 1998.

[78] T. Nonaka, C. Okuda, Y. Ukyo, and T. J. Okamoto. In Situ XAFS Study on Cathode Materials for Lithium-Ion Batteries. *Synchrotron. Rad.*, 8:869–871, 2001.

[79] Y. Uchimoto, H. Sawada, and T. J. Yao. Changes in Electronic Structure by Li Ion Deintercalation in $LiNiO_2$ From Nickel L-Edge and O K-Edge XANES. *Power Sources*, 97/98:326–327, 2001.

[80] J. Graetz, A. Hightower, C. C. Ahn, R. Yazami, P. Rez, and B. Fultz. Electronic Structure of Chemically Delithiated $LiCoO_2$ Studied by Electron Energy-Loss Spectrometry. *J. Phys. Chem. B*, 106:1286–1289, 2002.

[81] W. S. Yoon, K. B. Kim, M. G. Kim, M. K. Lee, H. J. Shin, J. M. Lee, J. S. Lee, and C. H. Yo. Oxygen Contribution on Li-Ion Intercalation-Deintercalation in $LiCoO_2$ Investigated by O K-Edge and Co L-Edge X-Ray Absorption Spectroscopy. *J. Phys. Chem. B*, 106:2526–2532, 2002.

[82] G. Ceder, M. K. Aydinol, and A. F. Kohan. Application of First-Principles Calculations to the Design of Rechargeable Li-Batteries. *Comput. Mater. Sci.*, 8:161–169, 1997.

[83] F. Ronci, B. Scrosati, V. R. Albertini, and P. Perfetti. In Situ Energy Dispersive X-ray Diffraction Study of $LiNi_{0.8}Co_{0.2}O_2$ Cathode Material for Lithium Batteries. *J. Phys. Chem. B*, 105:754–759, 2001.

[84] R. A. Sharma and R. N. Seefurth. Themodynamic Properties of the Lithium-Silicon System. *J. Eectrochem. Soc.*, 123:1763–1768, 1976.

[85] C. J. Wen and R. A. Huggins. Chemical Diffusion in Intermediate Phases in the Lithium-Silicon System. *J. Solid State Chem.*, 37:271–278, 1981.

[86] C. van der Marel, G. J. B. Vinke, and W. van der Lugt. The Phase Diagram of The System Lithium-Silicon. *Solid State Comm.*, 54:917–919, 1985.

[87] R. Nesper and H. G. von Schnering. $Li_{21}Si_5$, A Zintl Phase As Well As a Hume-Rothery Phase. *J. Solid State Chem.*, 70:48–57, 1987.

[88] W. J. Weydanz, M. Wohlfahrt-Mehrens, and R. A. Huggins. A Room Temperature Study of the Binary Lithium-Silicon and the Ternary Lithium-Chromium-Silicon System for Use in Rechargeable Lithium Batteries. *J. Power Sources*, 81:237–242, 1999.

[89] J. O. Besenhard and H. P. Fritz. Cathodic Reduction of Graphite in Organic Solutions of Alkali and NR_4^+ Salts. *J. Electroanal. Chem.*, 53:329–333, 1974.

[90] J. O. Besenhard. The Electrochemical Preparation and Properties of Ionic Alkali Metal and NR_4 Graphite Intercalation Compounds in Organic Electrolytes. *Carbon*, 14:111–115, 1976.

[91] R. Yazami and S. Genies. Chemical Stability of Lithiated-HOPG with Some Organic Electrolytes. *Denki Kagaku*, 66:1293–1298, 1998.

[92] J. O. Besenhard, J. Yang, and M. Winter. Will Advanced Lithium-Alloy Anodes Have a Chance in Lithium-Ion Batteries? *J. Power Sources*, 68:87–90, 1997.

[93] M. Winter, J. O. Besenhard, M. E. Spahr, and P. Novak. Insertion Electrode Materials for Rechargeable Lithium Batteries. *Ad. Mater.*, 10:725–763, 1998.

[94] J. Yang, M. Winter, and J. O. Besenhard. Small Particle Size Multiphase Li-Alloy Anodes for Lithium-Ion Batteries. *Solid State Ionics*, 90:281–287, 1996.

[95] M. Winter and J. O. Besenhard. Electrochemical Lithiation of Tin and Tin-Based Intermetallics and Composites. *Electrochimica Acta*, 45:31–50, 1999.

[96] S. Bourderau, T. Brousse, and D. M. Schleich. Amorphous Silicon As a Possible Anode Material for Li-Ion Batteries. *J. Power Sources*, 81:233–236, 1999.

[97] H. Li, X. Huang, L. Chen, Z. Wu, and Y. Liang. A High Capacity Nano-Si Composite Anode Material for Lithium Rechargeable Batteries. *Electrochem. Solid State Lett.*, 2:547–549, 1999.

[98] G. Che, B. B. Lakshmi, E. R. Fisher, and C. R. Martin. Carbon Nanotube Membranes for Electrochemical Energy Storage and Production. *Nature*, 393:346–349, 1998.

[99] N. Li, C. R. Martin, and B. Scrosati. A High-Rate, High-Capacity, Nanostructured Tin Oxide Electrode. *Electrochem. Solid-State Lett.*, 3:316–318, 2000.

[100] N. Li and C. R. Martin. A High-Rate, High-Capacity, Nanostructured Sn-Based Anode Prepared Using Sol-Gel Template Synthesis. *J. Electrochem. Soc.*, 148:A164–A170, 2001.

[101] N. Li, J. Patrissi, G. Che, and C. R. Martin. Rate Capabilities of Nanostructured $LiMn_2O_4$ Electrodes in Aqueous Electrolyte. *J. Electrochem. Soc.*, 147:2044–2049, 2001.

[102] J. Patrissi and C. R. Martin. Improving the Volumetric Energy Densities of Nanostructured V_2O_5 Electrodes Prepared Using the Template Method. *J. Electrochem Soc.*, 148:A1247–A1253, 2001.

[103] L. Y. Beaulieu, D. Larcher, R. A. Dunlap, and J.R. Dahn. Reaction of Li with Grain-Boundary Atoms in Nanostructured Compounds. *J. Electrochem. Soc.*, 147:3206–3212, 2000.

[104] A. Ulus, Y. Rosenberg, L. Burstein, and E. Peled. Tin Alloy-Graphite Composite Anode for Lithium-Ion Batteries. *J. Electrochem. Soc.*, 149:A635–A643, 2002.

[105] G. W. Zhou, H. Li, H. P. Sun, D. P. Yu, Y. Q. Wang, X. J. Huang, L. Q. Chen, and Z. Zhang. Controlled Li Doping of Si Nanowires by Electrochemical Insertion Method. *Appl. Phys. Lett.*, 75:2447–2449, 1999.

[106] G. X. Wang, L. Sun, D. H. Bradhurst, S. Zhong, S. X. Dou, and H. K. Liu. Innovative Nanosize Lithium Storage Alloys with Silica As Active Centre. *J. Power Sources*, 88:278–281, 2000.

[107] L. B. Hong, C. C. Ahn, and B. Fultz. The Debye Temperature on Nanocrystalline β-Sn Measured by X-Ray Diffraction. *J. Mater. Res.*, 10:2408–2410, 1995.

[108] H. Li, X. Huang, L. Chen, G. Zhou, Z. Zhang, D. Yu, Y. J. Mo, and N. Pei. The Crystal Evolution of Nano-Si Anode Caused by Lithium Insertion and Extraction at Room Temperature. *Solid State Ionics*, 135:181–191, 2000.

[109] P. Limthongkul, Y. I. Jang, N. Dudney, and Y. M. Chiang. Electrochemically Driven Solid-State Amorphization in Lithium-Silicon Alloys and Implications for Lithium Storage. *Acta Materialia*, 51:1103–1113, 2003.

[110] *Handbook of Chemistry and Physics, 66th ed.* CRC Press, Boca Raton, 1985.

[111] R. A. Huggins. Lithium Alloy Negative Electrodes Formed from Convertible Oxides. *Solid State Ionics*, 113:57–67, 1998.

[112] C. P. Chen and H. Leipold. Fracture Toughness of Silicon. *Am. Ceram. Soc. Bull.*, 59:469–472, 1980.

[113] J. Bagdahn and Sharpe Jr. W. N. Fatigue of Polycrystalline Silicon Under Long-Term Cyclic Loading. *Sens. Actuators A*, 103:9–15, 2003.

[114] M. R. StJohn, A. J. Furgala, and A.F. Sammells. Lithium-Germanium Alloys As Negative Electrodes for Molten-Salt Batteries. *J. Electrochem. Soc.*, 127:C136–C137, 1980.

[115] J. Graetz, C. C. Ahn, R. Yazami, and B. Fultz. Highly Reversible Lithium Storage in Nanostructured Silicon. *Electrochem. and Solid State Lett.*, submitted, 2003.

[116] C. S. Fuller and J. C. Severiens. Mobility of Impurity Ions in Germanium and Silicon. *Phys. Rev.*, 96:21–24, 1954.

[117] J. Reed and G. Ceder. Charge, Potential, and Phase Stability of Layered $Li(Ni_{0.5}Mn_{0.5})O_2$. *Electrochem. Solid State Lett.*, 5:A145–A148, 2002.

[118] A. S. Andersson, B. Kalska, L. Haggstrom, and J. O. Thomas. Lithium Extraction/Insertion in $LiFePO_4$: an X-Ray Diffraction and Mossbauer Spectroscopy Study. *Solid State Ionics*, 130:41–52, 2000.

[119] A. Yamada and S. C. Chung. Crystal Chemistry of the Olivine-Type $Li(Mn_yFe_{1-y})PO_4$ and $(Mn_yFe_{1-y})PO_4$ As Possible 4 V Cathode materials for lithium batteries. *J. Electrochem. Soc.*, 148:A960–A967, 2001.

[120] Karen Elizabeth Thomas. Lithium-Ion Batteries: Thermal and Interfactial Phenomena. Ph.D. thesis in Chemical Engineering, Univ. of Calif., Berkeley, 2002.

[121] K. Dokko, M. Mohamedi, Y. Fujita, T. Itoh, M. Nishizawa, M. Umeda, and I. Uchida. Kinetic Characterization of Single Particles of $LiCoO_2$ by AC Impedance and Potential Step Methods. *J. Electrochem. Soc.*, 148:A422–A426, 2001.

[122] J. P. Cho, H. S. Jung, Y. C. Park, G. B. Kim, and H. S. Lim. Electrochemical Properties and Thermal Stability of $Li_aNi_{1-x}Co_xO_2$ Cathode Materials. *J. Electrochem. Soc.*, 147:15–20, 2000.

[123] N. J. Dudney, J. B. Bates, R. A. Zuhr, S. Young, J. D. Robertson, H. P. Jun, and S. A. Hackney. Nanocrystalline $Li_xMn_{2-y}O_4$ Cathodes for Solid-State Thin-Film Rechargeable Lithium Batteries. *J. Electrochem. Soc.*, 146:2455–2464, 1999.

[124] J. F. Whitacre, W. C. West, E. Brandon, and B. V. Ratnakumar. Crystallographically Oriented /Thin-Film Nanocrystalline Cathode Layers Prepared without Exceeding 300 Degrees C. *J. Electrochem. Soc.*, 148:A1078–A1084, 2001.

[125] J. R. Dahn, E. W. Fuller, M. Obrovac, and U. von Sacken. Thermal Stability of Li_xCoO_2, $LiNiO_2$ and λ-MnO_2 and Consequences for the Safety of Li-Ion Cells. *Solid State Ionics*, 69:265–270, 1994.

[126] A. R. WIZANSKY, P. E. RAUCH, and F. J. DISALVO. Powerful Oxidizing-Agents for the Oxidative Deintercalation of Lithium from Transition-Metal Oxides. *J. Solid State Chem.*, 81:203–207, 1989.

[127] R. V. Chebiam, F. Prado, and A. Manthiram. Comparison of the Chemical Stability of $Li_{1-x}CoO_2$ and $Li_{1-x}Ni_{0.85}Co_{0.15}O_2$ Cathodes. *J. Solid State Chem.*, 163:5–9, 2002.

[128] L. Seguin, G. Amatucci, M. Anne, Y. Chabre, P. Strobel, J. M. Tarascon, and G. Vaughan. Structural Study of NiO_2 and CoO_2 As End Members of the Lithiated Compounds by In Situ High Resolution X-Ray Powder Diffraction. *J. Power Sources*, 81:604–606, 1999.

[129] V. Rossi Albertini, P. Perfetti, F. Ronci, and B. Scrosati. Structural Changes of Electrodic Materials in Electrochemical Cells Observed by In Situ Energy Dispersive X-Ray Diffraction (EDXD). *Chem. Mater.*, 13:450–455, 2001.